

ANISOTROPIC ANALYSIS OF UNCONVENTIONAL RESERVOIRS
USING ROCK PHYSICS MODEL: EAGLE FORD SHALE
CASE STUDY

by
Ufuk Durmus

© Copyright by Ufuk Durmus, 2019

All Rights Reserved

A thesis submitted to the Faculty and the Board of Trustees of the Colorado School of Mines in partial fulfillment of the requirements for the degree of Master of Science (Geophysics).

Golden, Colorado

Date _____

Signed: _____

Ufuk Durmus

Signed: _____

Dr. James L. Simmons
Thesis Advisor

Golden, Colorado

Date _____

Signed: _____

Dr. Paul Constantin Sava
Professor and Head
Department of Geophysics

ABSTRACT

Eagle Ford shale has been of importance in the oil and gas industry with the new advent of unconventional technology in recent years. Previous studies have shown that Eagle Ford shale is a world-class source rock. Rock physics models help characterize the elastic properties of conventional and unconventional reservoirs.

In this thesis, I present a novel rock physics model for organic-rich shales. The extended Maxwell homogenization scheme is utilized as a rock physics model for transversely isotropic media. Since shales have complex structures, different components of the rock are modeled as multiple inclusions. First, I estimate the anisotropic clay matrix. This is then used as the host matrix, and quartz, calcite, kerogen, and fluid-filled pores are modeled as inclusions with different aspect ratios. Representation of multiple inhomogeneities with different aspect ratios is non-trivial. Yet, I suggest a solution to the representation difficulty using this new model. The Maxwell homogenization scheme honors the aspect ratio of each inclusion embedded in an effective inclusion domain.

Combined rock physics models have been used to obtain elastic properties of clays and shales. Notwithstanding, there is no consistent method for modeling both. The developed rock physics model and workflow thoroughly handle the estimation of elastic stiffness coefficients of both clays and shales in anisotropic media. This study shows that this rock physics model can be readily applied to other unconventional reservoirs.

Dipole sonic log and core measurements of the Eagle Ford shale field are utilized to constrain the modeling results. I process and interpret dipole sonic logs to obtain elastic stiffness coefficients C_{33} , C_{55} and C_{66} . Subsequently, I use these coefficients to validate the outcomes of the Maxwell homogenization scheme. To my knowledge, this is one of the first studies that verify the robustness of this rock physics template with field data.

After obtaining the elastic stiffness tensor of the Eagle Ford shale in VTI media, I estimate the Thomsen parameters (i.e. anisotropy parameters). Anisotropy parameters ϵ , γ and δ , on average, are 0.19, 0.29 and 0.04, respectively based on my modeling results in Eagle Ford shale. Anisotropic modeling results exhibit a good correlation with dipole sonic logs. Both dipole sonic log analysis and rock physics results demonstrate that clay content is the main driver of anisotropy in the field, and there is a direct relationship between clay volume and anisotropy parameters of ϵ and γ . In addition, kerogen and fluid-filled pores have second-order influence on anisotropy in shales. Anisotropic analysis is of importance in this study because neglecting anisotropy can lead to erroneous seismic interpretation, processing, and imaging in the area of interest. This new model allows one to estimate geomechanical properties as well as seismic properties. The directional dependence of geomechanical properties should be taken into account in order for operators to optimize hydraulic fracture design and to develop the field more efficiently.

In addition, I investigate implications of the modeling results on multicomponent seismic data. Amplitude variation with angle (AVA) analysis shows increasing anisotropy in the reservoir could result in significant variation in P-wave, C-wave and S-wave datasets. I show that the isotropic assumption results in deviation at the mid and far angles.

TABLE OF CONTENTS

ABSTRACT	iii
LIST OF FIGURES	viii
LIST OF TABLES	xii
LIST OF SYMBOLS	xiv
LIST OF ABBREVIATIONS	xvi
ACKNOWLEDGMENTS	xviii
DEDICATION	xix
CHAPTER 1 INTRODUCTION	1
1.1 Project Overview	1
1.2 Geology	2
1.3 Available Datasets	4
1.4 Research Objectives	6
1.5 Thesis Outline	8
CHAPTER 2 DIPOLE SONIC LOG PROCESSING AND INTERPRETATION	9
2.1 Introduction to Dipole Sonic Log Analysis	9
2.2 Stoneley Wave	10
2.3 Dipole Sonic Log Processing	11
2.4 Interpretation	13
2.5 Discussion	15
2.6 Summary	16

CHAPTER 3 ROCK PHYSICS MODEL	17
3.1 Introduction to the Rock Physics Model	17
3.2 Mineralogy	17
3.3 Reservoir and Fluid Properties	19
3.4 Maxwell Homogenization Scheme	22
3.5 Estimation of Elastic Properties of the Rock	25
3.5.1 Clay Matrix	26
3.5.2 Shale Matrix	36
3.6 On the Shape of Effective Inclusion	39
3.7 Anisotropy of Clay and Eagle Ford Shale	40
3.8 Velocity Analysis	44
3.9 Geomechanical Properties	46
3.10 Effect of Pore Fluids on Seismic Properties	48
3.11 Effect of Thermal Maturity on Seismic Properties	50
3.12 Discussion	52
3.13 Summary	53
CHAPTER 4 IMPLICATIONS FOR MULTICOMPONENT SEISMIC DATA	54
4.1 Introduction to AVA Analysis	54
4.2 AVA Analysis in VTI Media	54
4.3 Effect of Thermal Maturity on AVA	59
4.4 Effect of Pore Fluids on AVA	62
4.5 Discussion	64
4.6 Summary	64

CHAPTER 5 CONCLUSIONS	65
5.1 Observations and Discussion	65
5.2 Suggestions for Future Work	66
REFERENCES CITED	68
APPENDIX A TENSORIAL BASIS OF SEVOSTIANOV AND KACHANOV, 2002 . .	74
APPENDIX B MAXWELL HOMOGENIZATION SCHEME OF SEVOSTIANOV, 2014	77
APPENDIX C P TENSOR DERIVATION IN ANISOTROPIC MEDIA BY SEVOSTIANOV ET AL, 2005	79

LIST OF FIGURES

Figure 1.1	Project area in Eagle Ford play (modified from U.S. Energy Information Administration, 2014).	1
Figure 1.2	Stratigraphic column of Eagle Ford formation and a typical log in the area of interest (modified from Ratcliffe <i>et al.</i>).	2
Figure 1.3	San Marcos Arch and southwest-northeast (AA') cross section of Eagle Ford (modified from Hentz <i>et al.</i> , 2014).	3
Figure 1.4	The RCP project area is located between oil and gas window (courtesy of Devon).	3
Figure 1.5	Eagle Ford project data acquisition timeline.	4
Figure 1.6	Well locations in the project relative to seismic survey area (the wells used for this thesis circled in red).	5
Figure 2.1	Representation of shear wave and Stoneley wave propagations in a vertical borehole	11
Figure 2.2	Sketch of different waveforms recorded in a borehole (after Close <i>et al.</i> , 2009).	12
Figure 2.3	Well log data from Well C a) bulk density log covering both Austin chalk and Eagle Ford layers. b) slowness curves. (Blue curve is compressional wave slowness. Red and yellow curves denote shear wave slownesses in two different directions. Green curve is calculated horizontal shear slowness. Purple curve represents Stoneley wave slowness. Light blue curve is the assumed mud slowness).	13
Figure 2.4	a) Stiffness coefficients of C_{33} , C_{44} , C_{55} , C_{66} covering both Austin chalk and Eagle Ford layers (a median filter is applied to C_{66} estimation to highlight its features). b) Stiffness coefficients of C_{44} , C_{55} , C_{66} zoomed-in Eagle Ford section.	14
Figure 2.5	a) Anisotropy parameter γ and clay content changing with depth within Eagle Ford interval. b) Cross plot of γ and clay content, correlation coefficient is 0.81.	16

Figure 3.1	Mineralogical composition, kerogen content and effective porosity of the Eagle Ford Shale with depth obtained from Well C	18
Figure 3.2	Ternary diagram of the mineralogical composition of the Eagle Ford Shale in volume fraction obtained from Well C	19
Figure 3.3	Liquid gravity map of Eagle Ford play (after Gherabati <i>et al.</i> , 2016). . . .	20
Figure 3.4	Pressure map of Eagle Ford play (after Gherabati <i>et al.</i> , 2016).	21
Figure 3.5	Illustration of "volume V" of the rock matrix and "volume V*" of the cut domain with different inhomogeneties and aspect ratios on the left and, illustration of equivalent medium with unknown properties within the volume of V* on the right.	23
Figure 3.6	a) The shape of effective inclusion domain in Maxwell's original work and other previous studies b) The shape of effective inclusion domain suggested by Sevostianov and this study.	24
Figure 3.7	Aspect ratio of each inclusion defined by the ratio of a_3 over a_1 with x_3 and x_1 axes, respectively.	25
Figure 3.8	Clay matrix composition in the survey area from the core measurements provided by the vendor.	26
Figure 3.9	Structure of clay minerals, 2:1 structure on the left, 1:1 structure on the right and each layer consists of either structure in a deck of cards (after Castberg, 2014).	27
Figure 3.10	Schematic representation of clay platelets and how their diagenesis occur (modified from Castberg, 2014).	28
Figure 3.11	Volume fraction of total porosity and effective porosity in addition to calculated bound water volume and the ratio of bound water to clay content in Well C.	29
Figure 3.12	Illustration of how to obtain clay matrix using the rock physics model . .	30
Figure 3.13	Five independent stiffness coefficients of clay matrix found within the Eagle Ford section.	32
Figure 3.14	Bulk and shear moduli of clay matrix estimated using Voigt bound, Reuss bound and Hill's average	34

Figure 3.15	a) Upper (HS+) and lower (HS-) Hashin-Shtrikman bounds of bulk modulus of water-clay composite with overlain Maxwell homogenization scheme results. b) Upper and lower HS bounds of shear modulus of water-clay composite with overlain Maxwell homogenization scheme results	36
Figure 3.16	Modeling of Eagle Ford shale, clay matrix used as a background medium and quartz, calcite, kerogen and fluid-filled pores modeled as inclusions	37
Figure 3.17	Core photos of Well L provided by the vendor. a) highly laminated Eagle Ford shale structure. b) organic matter with low aspect ratio (kerogen) and spherical calcite particles.	37
Figure 3.18	Five independent stiffness coefficients of shale matrix within the Eagle Ford section constrained by C_{33} , C_{55} and C_{66} obtained by dipole sonic logs (note that $C_{44} = C_{55}$ in VTI media)	38
Figure 3.19	Five independent stiffness coefficients of shale matrix within the Eagle Ford section comparison of suggested aspect ratio calculation with spherical assumption	39
Figure 3.20	Anisotropy of clay matrix obtained using Maxwell homogenization scheme within the Eagle Ford section	41
Figure 3.21	Cross-plots of different anisotropy parameters calculated for clay matrix .	42
Figure 3.22	Anisotropy of Eagle Ford shale obtained using Maxwell homogenization scheme	42
Figure 3.23	Cross-plots of different anisotropy parameters calculated for Eagle Ford shale	43
Figure 3.24	Relationships between anisotropy parameters and clay content within Eagle Ford section	43
Figure 3.25	a) Vertical P-wave velocity b) Vertical S-wave velocity estimation using rock physics model compared to well logs	45
Figure 3.26	a) Horizontal P-wave velocity b) Horizontal S-wave velocity estimation of Eagle Ford shale in VTI media using Maxwell homogenization scheme. .	46
Figure 3.27	Poisson's ratio estimation in vertical and horizontal directions within Eagle Ford section.	47

Figure 3.28	Young's modulus estimation in vertical and horizontal directions within Eagle Ford section.	48
Figure 3.29	Effect of pore fluids on seismic impedances in comparison with the well data	49
Figure 3.30	Effect of maturity on seismic impedances in comparison with the well data	51
Figure 4.1	computed P-wave AVA curves using the models given in Table 4.1 and Table 4.2	57
Figure 4.2	computed PS-wave AVA curves using the models given in Table 4.1 and Table 4.2	58
Figure 4.3	computed SV-wave AVA curves using the models given in Table 4.1 and Table 4.2	58
Figure 4.4	computed SH-wave AVA curves using the models given in Table 4.1 and Table 4.2	59
Figure 4.5	Computed P- and PS-wave AVA curves using the models given in Table 4.3	61
Figure 4.6	Computed SV- and SH-wave AVA curves using the models given in Table 4.3	61
Figure 4.7	Computed P- and PS-wave AVA curves using the models given in Table 4.4.	63
Figure 4.8	Computed SV- and SH-wave AVA curves using the models given in Table 4.4.	63

LIST OF TABLES

Table 1.1	Core and petrophysical data used in this study	5
Table 2.1	Anisotropy classification using stiffness coefficients	14
Table 3.1	Fluid properties of Eagle Ford using Batzle & Wang (1992) equations . . .	20
Table 3.2	Isotropic elastic moduli of clay minerals (a = Katahara (1996), b = Wang <i>et al.</i> (2001))	31
Table 3.3	Stiffness coefficients of clay matrix compared to analyses from literature (A = Ortega <i>et al.</i> (2007), B = Bayuk <i>et al.</i> (2007), C= Sayers (2005)) . .	32
Table 3.4	Comparison of isotropic elastic moduli of clay matrix (the results from the rock physics model shown at the bottom)	34
Table 3.5	Elastic moduli and densities of various minerals and fluids (a = Mavko <i>et al.</i> (2009), b = Bandyopadhyay (2009), c = Craddock <i>et al.</i> (2019)) . .	38
Table 3.6	Acoustic core measurements from two different wells provided by the vendor	45
Table 3.7	Elastic moduli and densities of oil and gas provided by Sang & Sun (2016) .	49
Table 3.8	The effect of pore fluids on P and S impedance based on the rock physics modeling results	50
Table 3.9	Elastic moduli and densities of kerogen used in this analysis at different maturity stages a = Yan & Han (2013), b = Qin* <i>et al.</i> (2014) and, c = Lucier <i>et al.</i> (2011)	50
Table 3.10	The effect of maturity level of kerogen on P and S impedance based on the rock physics modeling results	52
Table 4.1	Vertical velocities and densities obtained from the rock physics model used for AVA analysis.	56
Table 4.2	Thomsen parameters obtained using the rock physics model for AVA analysis.	56

Table 4.3	The effect of maturity level of kerogen on P and S velocities and anisotropy based on the rock physics modeling results	60
Table 4.4	The effect of pore fluids on P and S velocities and anisotropy based on the rock physics modeling results	62

LIST OF SYMBOLS

aspect ratio	α
aspect ratio of effective inclusion domain	$\alpha_{(\Omega)}$
Thomsen's anisotropy parameter	ϵ
Thomsen's anisotropy parameter	γ
Thomsen's anisotropy parameter	δ
Alkhalifah and Tsvankin's anisotropy parameter	η
fourth rank stiffness tensor	C_{ijkl}
stiffness tensor in Voigt notation	C_{ij}
vitritinite reflectance of kerogen	$\%R_0$
density	ρ
bulk density	ρ_b
vertical P-wave velocity	V_{P0}
horizontal P-wave velocity	V_{P90}
vertical S-wave velocity	V_{S0}
horizontal S-wave velocity	V_{S90}
total porosity	ϕ_{total}
effective porosity	ϕ_{eff}
bound water volume	ϕ_{bw}
parts per million	ppm
pound-force per square inch	psi

gigapascal	GPa
compliance contribution tensor	H
stiffness contribution tensor	N
compliance contribution tensor of the effective inclusion domain in Maxwell's scheme	H_{eff}
stiffness contribution tensor of the effective inclusion domain in Maxwell's scheme	N_{eff}
stiffness tensor of the host medium	C_0
stiffness tensor of the effective medium	C_{eff}
compliance tensor of the host medium	S_0
compliance tensor of two Hill's tensors	Q
stiffness tensor of two Hill's tensors	P
the Hill's compliance tensor calculated for the shape of Ω	Q_Ω
the Hill's stiffness tensor calculated for the shape of Ω	P_Ω
effective inclusion domain in Maxwell's scheme	Ω
P-impedance	I_P
S-impedance	I_S
bulk modulus	K
shear modulus	μ
bulk modulus of the host medium	K_0
shear modulus of the host medium	μ_0
poisson's ratio of the host medium	ν_0
Young's modulus	E

LIST OF ABBREVIATIONS

Reservoir Characterization Project	RCP
Colorado School of Mines	CSM
X-Ray Diffraction	XRD
Scanning Electron Microscope	SEM
Eagle Ford	EF
Austin Chalk	AC
Distributed Acoustic Sensing	DAS
Distributed Temperature Sensing	DTS
Vertical Seismic Profile	VSP
Pressure Volume Temperature	PVT
Time Lapse	4D
Three Dimensional	3D
Nine Component	9C
Three Component	3C
Amplitude Variation with Angle	AVA
Amplitude Variation with Offset	AVO
Vertical Transverse Isotropy	VTI
Horizontal Transverse Isotropy	HTI
Differential Effective Medium	DEM
Self Consistent Approximation	SCA

Standard Cubic Foot	SCF
Stock Tank Barrel	STB

ACKNOWLEDGMENTS

First of all, I would like to thank my advisor, Dr. Jim Simmons for his guidance. It's been fun to work with him. I would like to extend my gratitude to Dr. Gary Binder. I really enjoyed fruitful discussions with him, and he always had stimulating ideas for the model we developed. I am grateful to Dr. Ali Tura for making me a member of RCP and being on my committee. I also would like to thank Dr. Jeffrey Shragge and Dr. Jennifer Miskimins for being my committee members and their feedback.

I acknowledge Devon and Penn Virginia for providing the dataset and permission to publish this study. I am thankful for Turkish Petroleum Corporation for providing financial support for my study at Mines. It has been great to work with the Eagle Ford team in RCP, thank you all for the collaboration and amazing teamwork.

I also would like to thank my friends for making my time more enjoyable at CSM. It's been a great pleasure for me to have Can Oren, Odette Aragao, Jihyun Yang, Deniz Donmez, Mert Kiraz, Tugrul Konuk, Youfang Liu, Aleksei Titov, Anna Titova, Mihriban Genc, Oscar Jarillo Michel and Ivan Lim. I'll never forget the fun moments we had at GCB and other activities. I am thankful to my friends, Nurhan Tabakyan, Yaşar Metin and Hakan Yılmaz for their sincere friendship and support.

During the time I spent in Golden, I had a privilege to meet and live with my German family, Andreas Rüger & Christa Rüger and their daughters Sydney and Jessica. I will surely miss our hiking, biking and skiing adventures with Gary Wong in beautiful Colorado. I am also thankful to Jean and Sam Guyton for sharing the fun at the cabin.

Last but not least, I am most indebted to my family. I am very grateful to my mom, Nursen Demirel Durmuş, my dad, Hüseyin Durmuş, and my lovely sister, Birsen Durmuş for their endless support and invaluable encouragement for all the decisions I have made in my entire life.

I dedicate this thesis to my mom, who is the best teacher I have ever had
and to my dad, who is the most honest and hard-working man I have ever known.

CHAPTER 1

INTRODUCTION

1.1 Project Overview

The Eagle Ford project is the main research project of Phase XVII in the Reservoir Characterization Project (RCP). Devon Energy Corporation and Penn Virginia Corporation are the providers of the robust dataset in the Eagle Ford project. Since the unconventional reservoirs are complex, an integrated approach plays a vital role to better understand the reservoir and to develop the field efficiently. The major issues are completion design, well spacing, cluster spacing, and fluid properties. These can be solved by integrating geophysical analysis, geological understanding, and engineering applications. This pilot project aims to address these issues and develop practical solutions for the lifespan of the field. Figure 1.1 shows the RCP project area in the Eagle Ford play located central south Texas, in and around Lavaca and DeWitt counties.

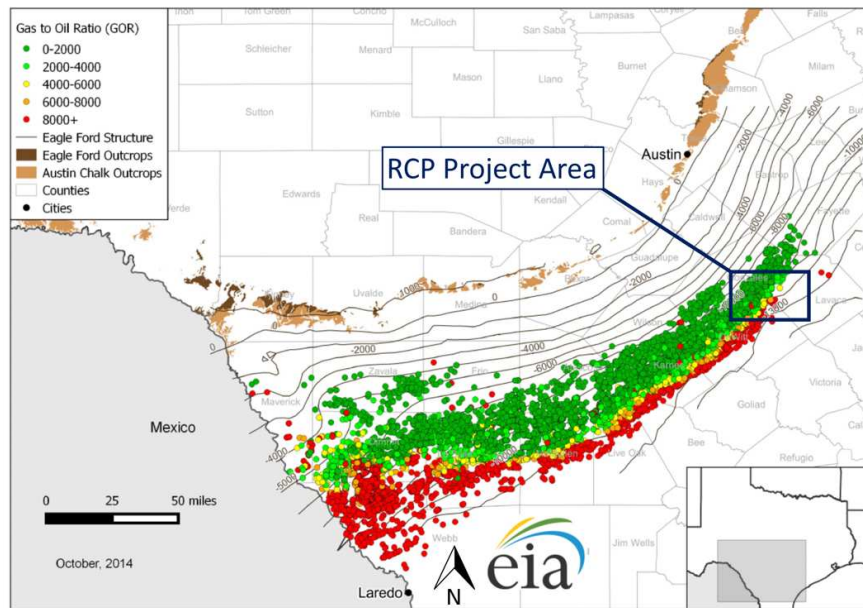


Figure 1.1: Project area in Eagle Ford play (modified from U.S. Energy Information Administration, 2014).

1.2 Geology

Eagle Ford shale is an organic-rich calcareous-mudrock. This formation was deposited in marine continental shelf environment. The late Cretaceous Eagle Ford formation is sandwiched between Austin chalk and Buda limestone (Figure 1.2). Eagle Ford shale play stretches from Mexico border to northeast Texas. The thickness of the Eagle Ford shale unit increases from northwest to southeast. In addition, reservoir properties such as temperature, pressure and hydrocarbon maturity level increases in the same direction.

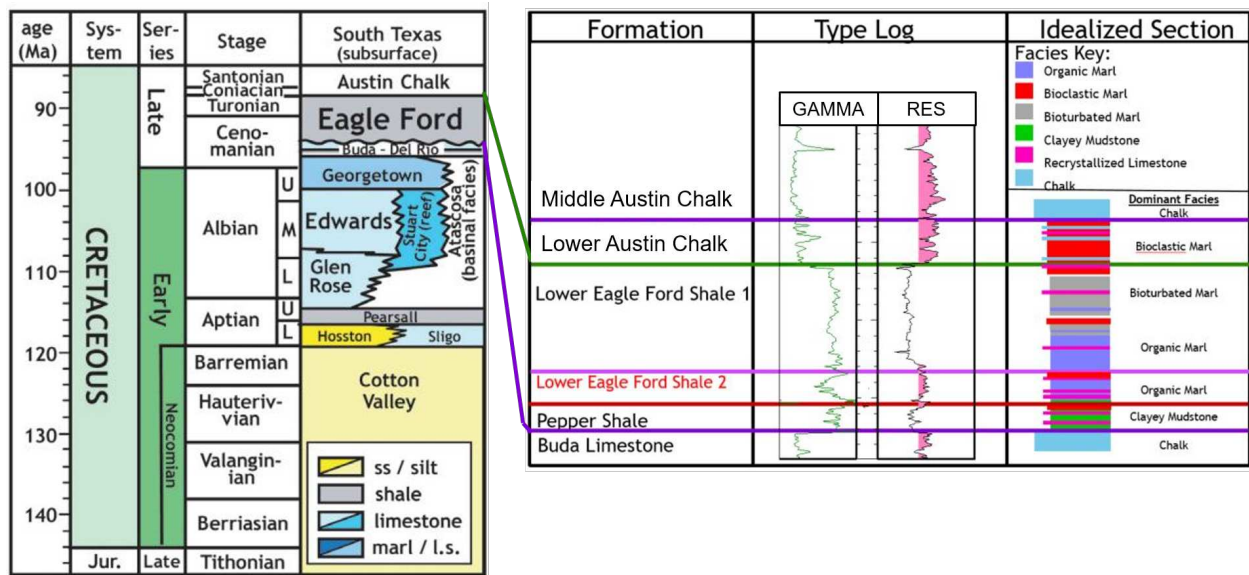


Figure 1.2: Stratigraphic column of Eagle Ford formation and a typical log in the area of interest (modified from Ratcliffe *et al.* (2012)).

Although, Eagle Ford formation is named as a "shale", it is mostly carbonate-rich mudrock. The Eagle Ford shale is divided into two units, which are Upper and Lower Eagle Ford (Hentz & Ruppel, 2010). The Lower Eagle Ford unit has high organic content and highly laminated structure. Since our study area is in the proximity of the San Marcos arch, we do not observe Upper Eagle Ford facies (Figure 1.3). For this reason, Lower Eagle Ford shale is the main focus of this research.

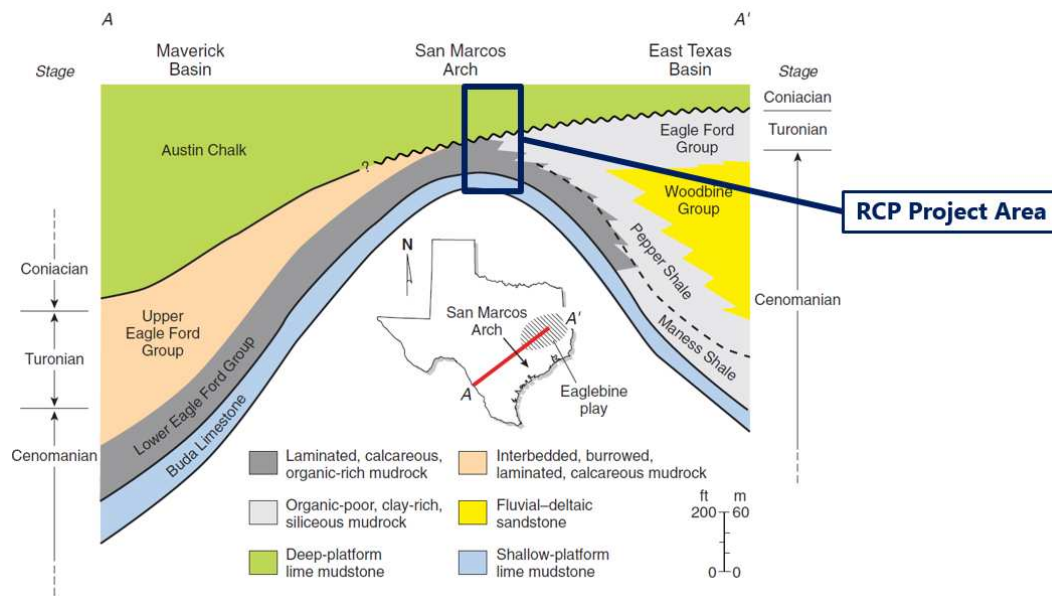


Figure 1.3: San Marcos Arch and southwest-northeast (AA') cross section of Eagle Ford (modified from Hentz *et al.*, 2014).

Because of the changing reservoir properties of the Eagle Ford shale, our field is located between the oil and gas window, which is directly related to the maturity of kerogen (Figure 1.4).

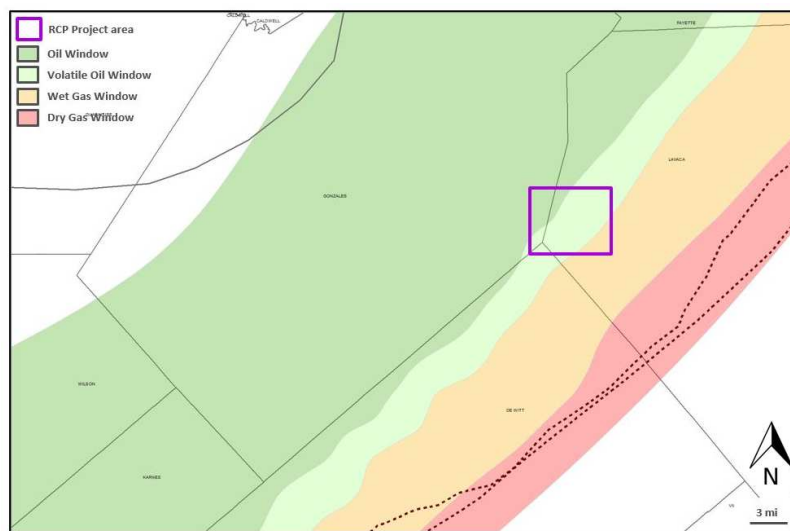


Figure 1.4: The RCP project area is located between oil and gas window (courtesy of Devon).

1.3 Available Datasets

For this pilot project, various datasets were acquired to analyze the unconventional reservoir for future development and production. This dataset includes vertical seismic profiles (VSP) (Schultz, 2019), 9-C 3D surface seismic data (Tuppen, 2019), 3-C 4D surface seismic data, microseismic data, distributed acoustic sensing (DAS) and distributed temperature sensing (DTS) data (Figure 1.5). While these datasets were provided by Devon Corporation, Penn Virginia Corporation also provided well logs, core analysis, production and completion reports.

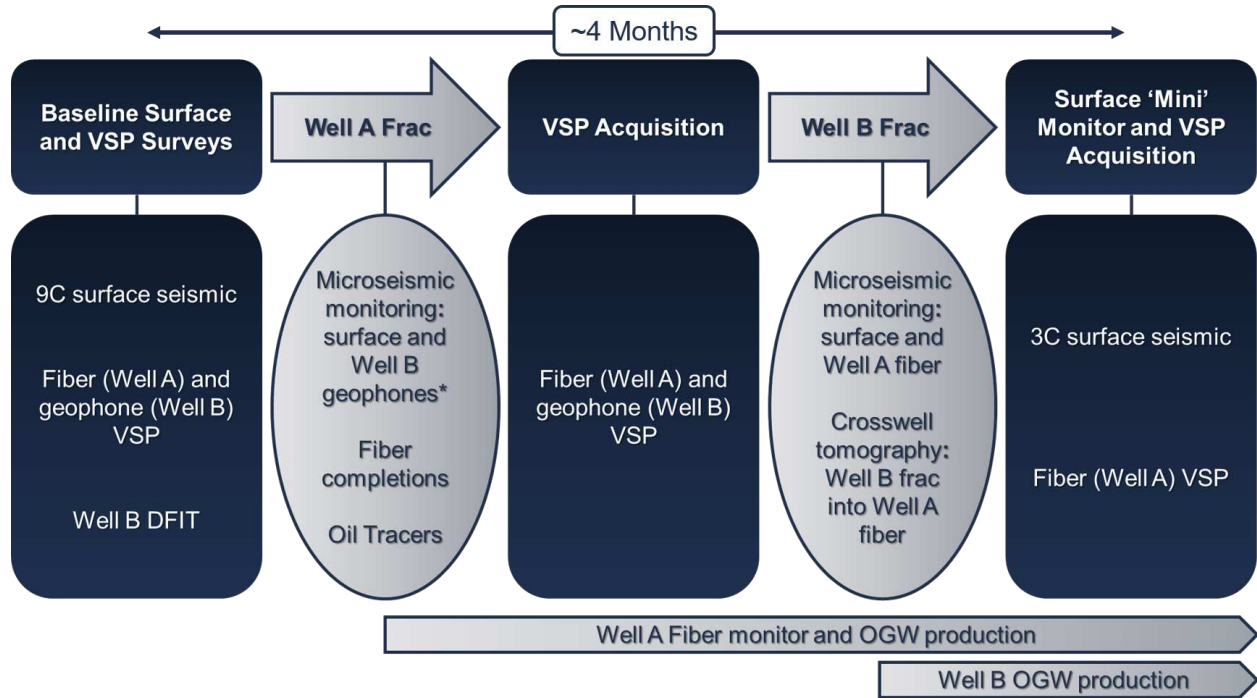


Figure 1.5: Eagle Ford project data acquisition timeline.

The data set I have used in this thesis has both advantages and disadvantages (Table 1.1). The well log measurements and the petrophysical model were provided by the vendors. Since, they are not our own measurements and analysis, the methods used and the associated error are unknown. Because Well C has both mineralogy information and a dipole sonic log, it is mainly used to constrain the rock physics model in terms of stiffness coefficients.

Table 1.1: Core and petrophysical data used in this study

Data / Well Name	Well C	Well G	Well D	Well N
Petrophysical Mineralogy	✓	✓	X	X
XRD Mineralogy	X	X	✓	✓
Sonic Logs	✓	X	X	X
Acoustic Core Measurements	X	X	only vertical	only horizontal

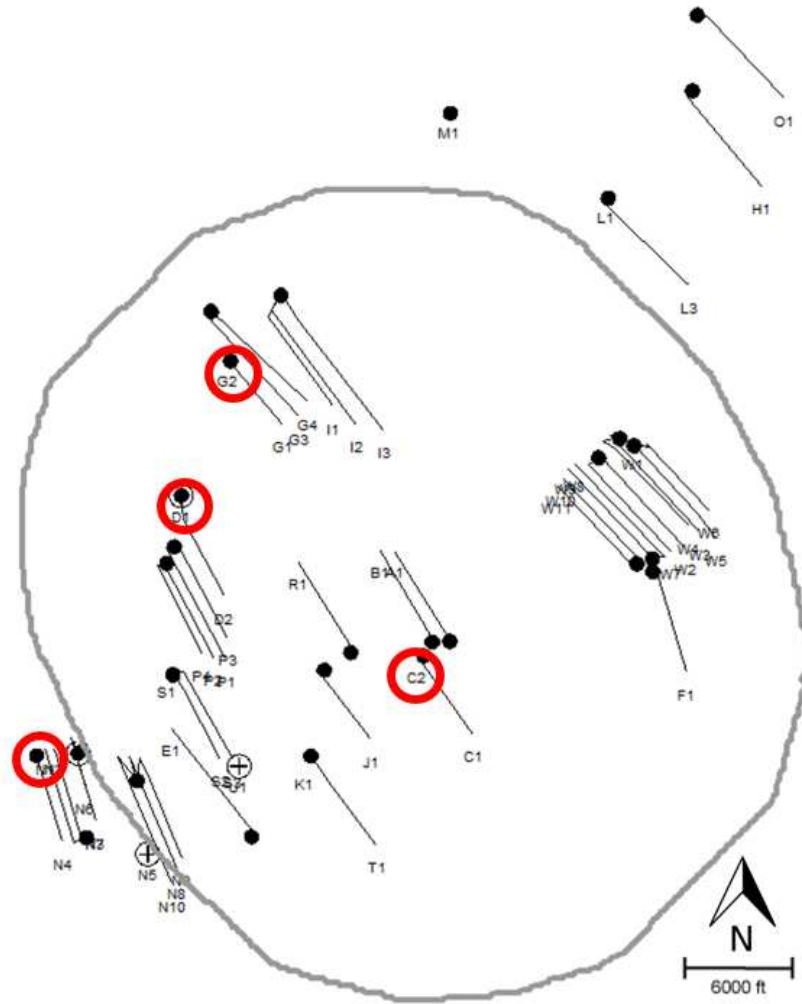


Figure 1.6: Well locations in the project relative to seismic survey area (the wells used for this thesis circled in red).

As far as core measurements are concerned, limited information can be attained. It is mainly because they did not measure velocities at different directions to gain insights into velocity anisotropy. On the other hand, we are able to constrain mineralogical composition in the reservoir with the multiple wells using petrophysical models and XRD analysis. Since Well C has both mineralogy and a dipole sonic log to constrain the rock physics model, it is primarily used to validate the rock physics modeling results. Well C is located in the middle of the survey area (Figure 1.6).

1.4 Research Objectives

In this thesis research, the main focus is to use the rock physics model to better understand seismic and geomechanical properties. Given that unconventional shale reservoirs have very complex structure, interpretation of reservoir properties in both seismic data and well logs is crucial for hydraulic fracturing design and well placement (Centurion *et al.*, 2012). To optimize production in horizontal wells, one needs to understand anisotropy in shales. Neglecting anisotropy can cause erroneous results in interpretation, processing and imaging of seismic data.

For instance, ongoing research in seismic inversion to obtain P and S impedance by Tuppen (2019) can be aided by the rock physics model. Lateral changes in P and S impedance estimates can be explained by the changes in rock properties such as porosity, kerogen content and mineralogy. Rock physics templates allow us to model the elastic behavior of changing rock properties so that we can better interpret the changes we observe in seismic and anisotropic analyses. Furthermore, one can obtain realistic values of Thomsen (1986) parameters δ along with ϵ and γ using anisotropic rock physics models. Estimating δ is particularly difficult in surface seismic data and core measurements. On a core sample, directional measurements (45°) are non-trivial, and prevent one from estimating anisotropy parameter δ . However, δ plays an important role in P-wave processing and imaging (Tsvankin *et al.*, 2010). Hence, rock physics models that can provide estimates of anisotropy parameters are helpful, and provide geophysicists with insights into seismic interpretation and processing,

and elastic behavior of rock. In particular, this research assists the development of the field in many aspects.

Previously, Sayers *et al.* (2015) investigated the effect of kerogen on anisotropy in shales using the effective medium theory of Sevostianov *et al.* (2005). However, this work does not take into account the effect of fluid-filled pores and more importantly clay platelets on anisotropy. Sayers & Dasgupta (2019) later use the extended Maxwell Homogenization scheme of Sevostianov & Giraud (2013); Sevostianov (2014) to model elastic properties of unconventional reservoirs with varying mineralogy. Yet, they assume that the shape of effective inclusion domain is spherical. Berryman & Berge (1996) and Sevostianov (2014) indicate that the chosen shape for the effective inclusion domain affects the estimation of elastic properties of an effective medium. Defining the aspect ratio of effective inclusion domain is non-trivial in case multiple inhomogeneties exist inside the medium. To address this issue, I use a method developed by Sevostianov (2014) in my rock physics model, which ensures that I represent the effective inclusion domain in my rock physics model correctly.

Individual clay minerals constitute a structure called the clay matrix. Obtaining the elastic stiffness tensor of the clay matrix in laboratory conditions is challenging. Hence, various combinations of rock physics models (i.e. differential effective medium (DEM), self consistent approximation (SCA), Kuster-Toksoz model (KT), Backus averaging) are utilized to invert for the stiffness tensor of the clay matrix using the core measurements on shale core samples (Sayers, 2005; Bayuk *et al.*, 2007). However, having multiple rock physics models can lead to inconsistent results because of certain assumptions about the models used. Although Sayers (2005) and Bayuk *et al.* (2007) use the same data set and the same rock physics models to invert for the clay matrix, they obtain different elastic stiffness coefficients.

The rock physics model I develop can handle estimation of clay matrix, and the same model is used to obtain effective elastic properties of organic-rich shales. So, this new model allows one to have a consistent method instead of having to use multiple rock physics models. In my workflow, I first estimate the anisotropic clay matrix, and I then utilize this matrix

as the host medium to model effective elastic properties of Eagle Ford shale.

1.5 Thesis Outline

In Chapter 2, I analyze dipole sonic logs from Well C to understand whether Eagle Ford shale and Austin Chalk are anisotropic. I also obtain three stiffness coefficients (C_{33} , C_{55} and C_{66}) from these logs to constrain the rock physics modeling results.

In Chapter 3, I introduce a new rock physics model and workflow for unconventional reservoirs. I describe the theory of the Maxwell homogenization scheme and the application of it as a rock physics model. I use the outcomes from Chapter 2 to validate the robustness of the rock physics modeling results.

In Chapter 4, I also demonstrate how this rock physics model can be used to analyze the implications for multicomponent (9C) seismic data. Using amplitude variation with angle (AVA), I test the sensitivity of different wave modes, namely P-wave, PS-wave (converted wave), SV-wave (RR or radial component), and SH-wave (TT or transverse component) with varying clay content in Eagle Ford shale.

CHAPTER 2

DIPOLE SONIC LOG PROCESSING AND INTERPRETATION

2.1 Introduction to Dipole Sonic Log Analysis

I aim to understand anisotropic characteristics of Eagle Ford shale in the area of interest. Dipole sonic logs can be used to determine whether a formation is anisotropic or not. In this chapter, I analyze both Austin chalk and Eagle Ford shale in terms of anisotropy. Using the slownesses of different wave modes (P and S), I calculate stiffness coefficients, which are later used to constrain the rock physics modeling results for Eagle Ford shale.

I analyze the dipole sonic log provided from Well C to obtain anisotropic information about both the Austin Chalk and Eagle Ford shale. Dipole sonic log data can provide direct measurements of compressional and shear-wave slownesses in different directions. In addition, the Stoneley wave measured in the borehole can be used to infer horizontal shear slowness. Using these wave modes, I compute elastic stiffnesses C_{33} , C_{44} , C_{55} and C_{66} as a function of depth. There are three cases that we can likely see in the area of interest using the information from dipole sonic logs, which are isotropic media, VTI (vertical transverse isotropy), and HTI (horizontal transverse isotropy) media. I show elastic stiffness tensors for each anisotropic symmetry system. Equation 2.1 represents isotropic elastic stiffness tensor with only two independent stiffness coefficients. Equations 2.2 and 2.3 present the elastic stiffness tensors for VTI and HTI media, respectively. VTI and HTI are the special cases of orthorhombic anisotropy with both having five independent stiffness coefficients.

$$\mathbf{C}^{(\text{ISO})} = \begin{pmatrix} \lambda + 2\mu & \lambda & \lambda & 0 & 0 & 0 \\ \lambda & \lambda + 2\mu & \lambda & 0 & 0 & 0 \\ \lambda & \lambda & \lambda + 2\mu & 0 & 0 & 0 \\ 0 & 0 & 0 & \mu & 0 & 0 \\ 0 & 0 & 0 & 0 & \mu & 0 \\ 0 & 0 & 0 & 0 & 0 & \mu \end{pmatrix}, \quad (2.1)$$

where λ and μ are Lamé's constants,

$$\mathbf{C}^{(\text{VTI})} = \begin{pmatrix} C_{11} & C_{12} & C_{13} & 0 & 0 & 0 \\ C_{12} & C_{11} & C_{13} & 0 & 0 & 0 \\ C_{13} & C_{13} & C_{33} & 0 & 0 & 0 \\ 0 & 0 & 0 & C_{55} & 0 & 0 \\ 0 & 0 & 0 & 0 & C_{55} & 0 \\ 0 & 0 & 0 & 0 & 0 & C_{66} \end{pmatrix}, \quad (2.2)$$

where $C_{12} = C_{11} - 2C_{66}$,

$$\mathbf{C}^{(\text{HTI})} = \begin{pmatrix} C_{11} & C_{13} & C_{13} & 0 & 0 & 0 \\ C_{13} & C_{33} & C_{23} & 0 & 0 & 0 \\ C_{13} & C_{23} & C_{33} & 0 & 0 & 0 \\ 0 & 0 & 0 & C_{44} & 0 & 0 \\ 0 & 0 & 0 & 0 & C_{55} & 0 \\ 0 & 0 & 0 & 0 & 0 & C_{55} \end{pmatrix}, \quad (2.3)$$

where $C_{23} = C_{33} - 2C_{44}$.

2.2 Stoneley Wave

A Stoneley wave is a guided wave that travels along a solid-solid interface (Stoneley, 1924). This wave has been of importance to petrophysicists in the oil and gas industry. First, a Stoneley wave has a unique character that carries quantitative information about reservoir fluid mobility and permeability (Saxena *et al.*, 2018). Secondly, a Stoneley wave can be used to derive horizontal shear wave velocity in the borehole indirectly (Norris & Sinha, 1993; Saxena *et al.*, 2018). There is a Pythagorean relationship among the Stoneley wave slowness, the mud and shear-wave slownesses as shown in Equation 2.4. Horizontal shear wave propagation is orthogonal to the borehole. Similarly, Stoneley wave propagates perpendicular to the borehole axis. For this reason, Stoneley wave slowness measurement carries indirect information regarding horizontal shear slowness. Shear-wave particle motion is perpendicular to the borehole wall. Fast shear-wave particle motion is orthogonal to slow shear wave (Figure 2.1).

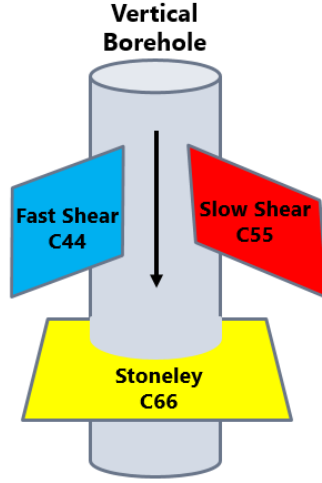


Figure 2.1: Representation of shear wave and Stoneley wave propagations in a vertical borehole

The Stoneley wave slowness is calculated as

$$\Delta t_{Stoneley}^2 = \Delta t_{Mud}^2 + \Delta t_{SH}^2 \frac{\rho_{mud}}{\rho_{bulk}}, \quad (2.4)$$

where $\Delta t_{Stoneley}$ is the Stoneley wave slowness. Δt_{Mud} is the mud slowness, Δt_{SH} is the horizontal shear wave slowness, and ρ_{mud} and ρ_{bulk} are the mud density and bulk density, respectively.

2.3 Dipole Sonic Log Processing

Using dipole sonic log measurements, we can directly obtain C_{33} , C_{44} and C_{55} by recording compressional slowness in addition to shear wave slownesses in x and y directions. We can intuitively convert slowness to velocity using Equation 2.5. In Figure 2.2, the Stoneley wave is seen as the slowest among waveforms. Rayleigh waves generally cannot be seen separately because they arrive as a part of shear waves in borehole recordings. The mud slowness is between shear waves and Stoneley wave. However, owing to its extra cost to service companies, mud properties in a wellbore are rarely measured. It is commonly known that density and velocity of the mud changes with depth, formation, pressure and temperature. We can reasonably predict mud density, which is slightly higher than water density. Mud

slowness, though, changes from field to field and should be determined between shear and Stoneley slowness depending upon reservoir properties (Bratton, 2018). Thus, one of the disadvantages of this technique is that C_{66} estimation heavily depends on mud properties and Stoneley slowness, which is not as sensitive to the formation as body waves.

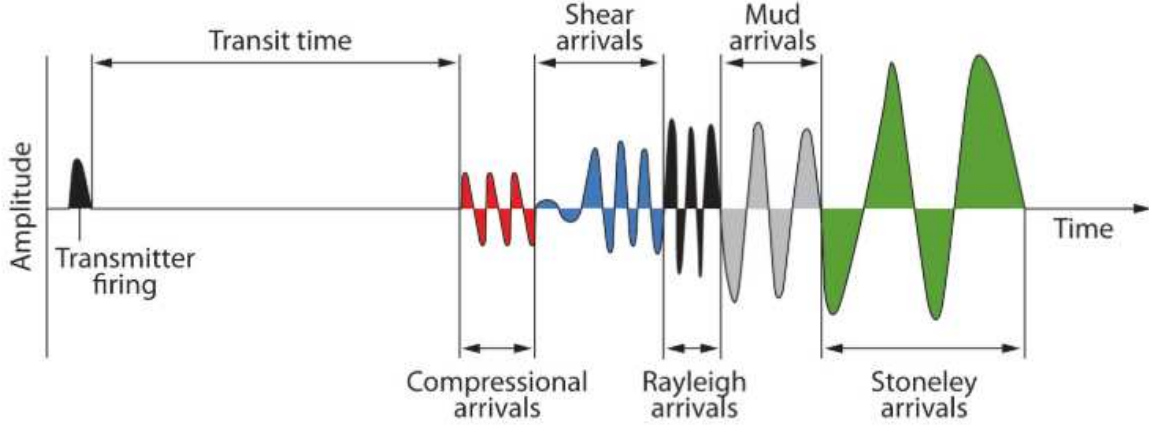


Figure 2.2: Sketch of different waveforms recorded in a borehole (after Close *et al.*, 2009).

$$V = \frac{10^6}{S}, \quad (2.5)$$

Here, V is velocity in ft/s . S is slowness in $\mu s/ft$. Using Equations 2.6 to 2.8, one can compute C_{33} , C_{44} and C_{55} stiffness coefficients. V_{P0} is vertical P-wave velocity estimated from compressional sonic log while V_{S1} and V_{S2} are fast and slow shear-wave velocities in x and y directions in the borehole, respectively. Bulk density is denoted as ρ_b .

$$C_{33} = \rho_b V_{P0}^2, \quad (2.6)$$

$$C_{44} = \rho_b V_{S1}^2, \quad (2.7)$$

$$C_{55} = \rho_b V_{S2}^2, \quad (2.8)$$

The bulk density of the Austin Chalk is much higher than Eagle Ford shale (Figure 2.3). It is also seen that the Stoneley wave does not vary with depth as much as compressional and shear waves. For my analysis, ρ_{mud} is assumed to be 1.1 g/cc , and mud slowness of 280

$\mu s/ft$ is found to be the best fit for our data.

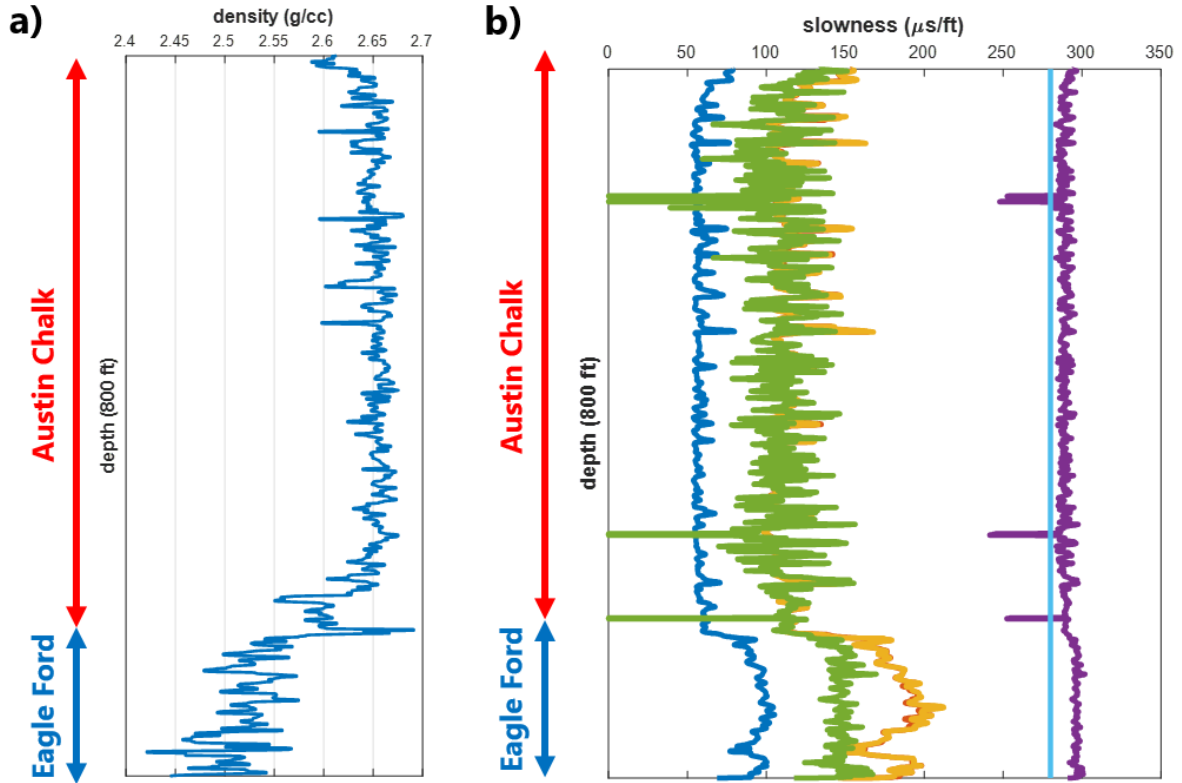


Figure 2.3: Well log data from Well C a) bulk density log covering both Austin chalk and Eagle Ford layers. b) slowness curves. (Blue curve is compressional wave slowness. Red and yellow curves denote shear wave slownesses in two different directions. Green curve is calculated horizontal shear slowness. Purple curve represents Stoneley wave slowness. Light blue curve is the assumed mud slowness).

2.4 Interpretation

After processing dipole sonic log data as described above, one can obtain four stiffness coefficients, namely C_{33} , C_{44} , C_{55} and C_{66} . This is important because the type of anisotropy and magnitude of reservoir can now be understood (Table 2.1). We can clearly interpret (Figure 2.4) that the Austin Chalk formation is mostly isotropic, since C_{44} , C_{55} , C_{66} are equal to one another. In addition, Eagle Ford shale is highly anisotropic and characterized as VTI media since there is no separation between C_{44} and C_{55} . Dipole sonic log shows important information about both the Austin chalk and Eagle Ford shale.

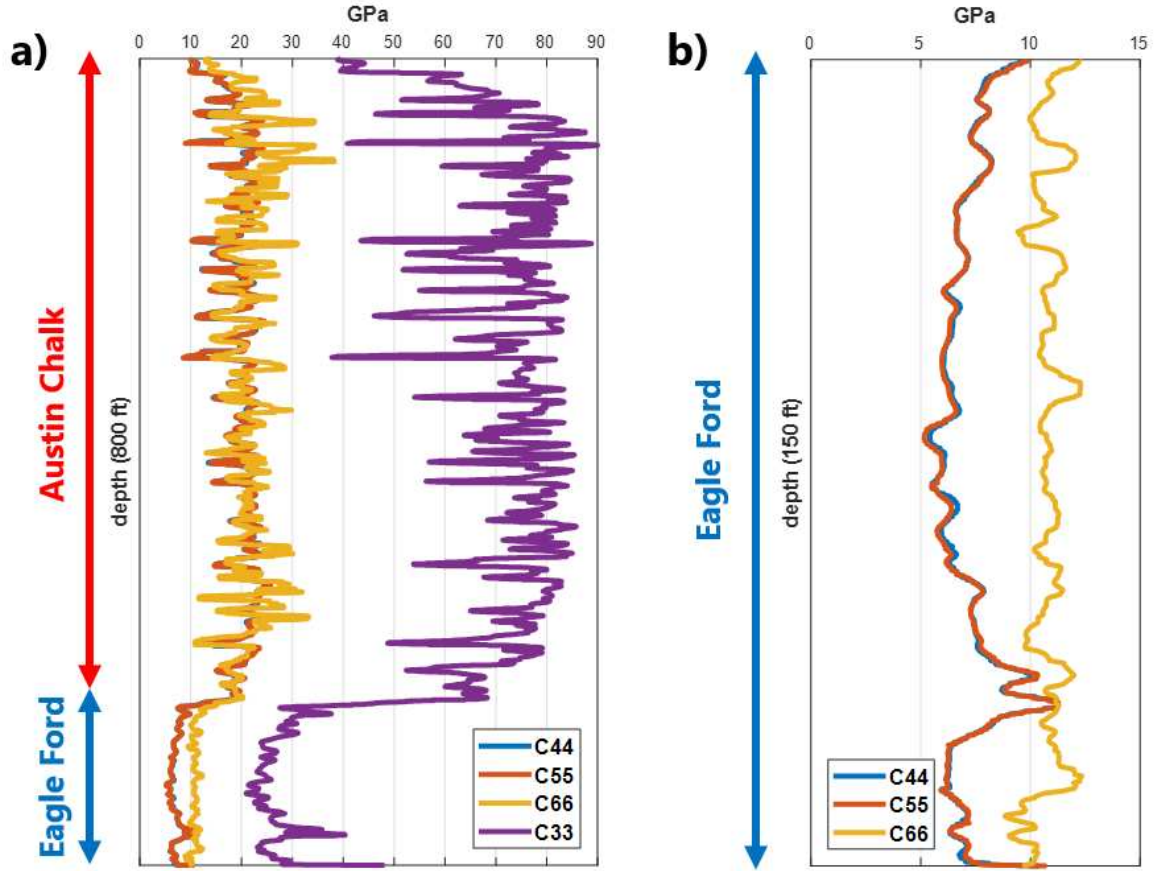


Figure 2.4: a) Stiffness coefficients of C_{33} , C_{44} , C_{55} , C_{66} covering both Austin chalk and Eagle Ford layers (a median filter is applied to C_{66} estimation to highlight its features). b) Stiffness coefficients of C_{44} , C_{55} , C_{66} zoomed-in Eagle Ford section.

Table 2.1: Anisotropy classification using stiffness coefficients

C_{ij} Relationships	Media
$C_{44} = C_{55} = C_{66}$	Isotropic
$(C_{44} = C_{55}) \neq C_{66}$	VTI
$C_{44} \neq (C_{55} = C_{66})$	HTI

2.5 Discussion

Now that we have shear stiffness coefficients (C_{44} , C_{55} , C_{66}), Thomsen's shear anisotropy parameter γ can be readily computed using Equation 2.9 (Thomsen, 1986). The γ parameter provides information about shear wave anisotropy (SH component).

$$\gamma = \frac{C_{66} - C_{55}}{2C_{55}}. \quad (2.9)$$

In Figure 2.5, a similar trend between anisotropy parameter γ and clay content within Eagle Ford section is shown. The correlation coefficient between them is 0.81. This result strongly suggests that there is a direct relationship between clay content and anisotropy, and unique structure and alignment of clay platelets are the main source of anisotropy in shales. The lack of a perfect correlation indicates that clays are not the only contributor of anisotropy. In addition to clays, kerogen content, pores and microfractures also contribute to anisotropy in shales.

Even though dipole sonic log analysis for anisotropic purposes has intrinsic issues such as certain assumptions about mud properties and Stoneley wave, one can still acquire valuable information regarding the reservoir and the type of anisotropy in the area of interest using dipole sonic log.

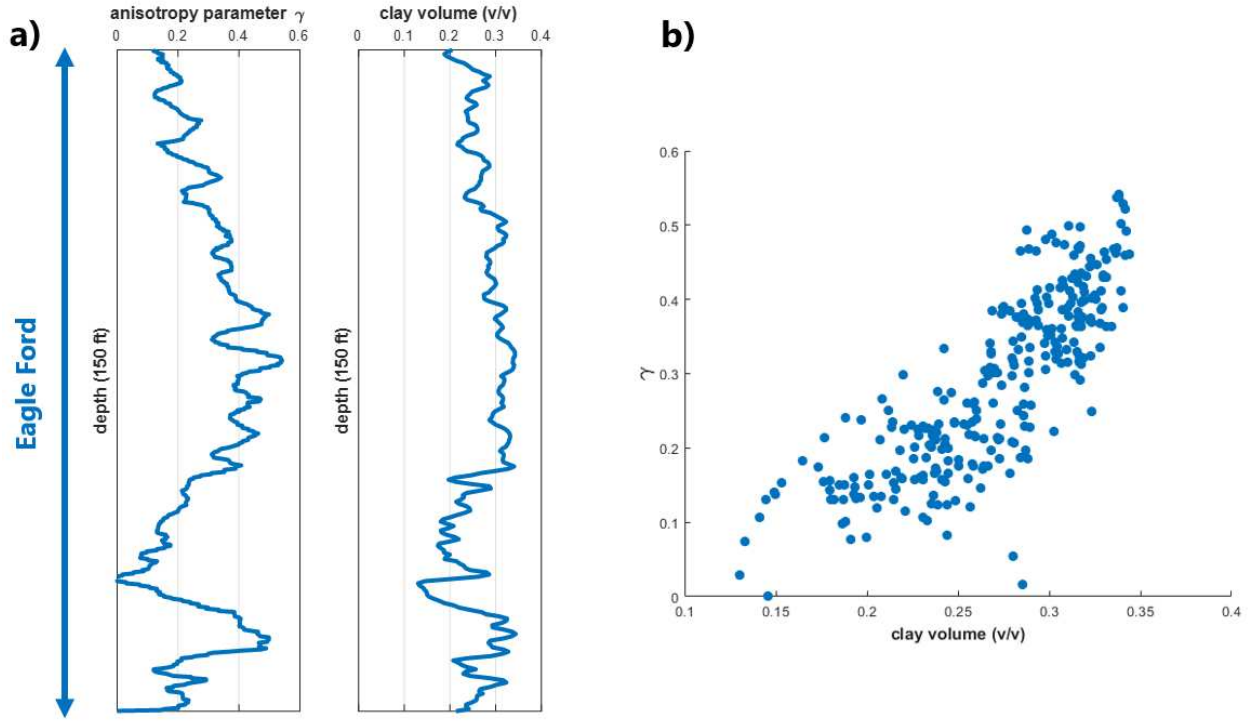


Figure 2.5: a) Anisotropy parameter γ and clay content changing with depth within Eagle Ford interval. b) Cross plot of γ and clay content, correlation coefficient is 0.81.

2.6 Summary

I performed analysis to obtain information about anisotropy for both Austin Chalk and Eagle Ford shale formations using dipole sonic log. Based on the results, Eagle Ford shale has vertical transverse isotropy (VTI), while Austin Chalk is isotropic. The interpretation of stiffness coefficients obtained from dipole sonic logs help identify the type of anisotropy in the formation. However, one should note that there are certain assumptions about mud properties that can intrinsically contain error to obtain horizontal shear wave velocity from dipole sonic logs. In addition, it is important that there is a strong correlation between clay content in Eagle Ford shale and the anisotropy parameter (γ).

CHAPTER 3

ROCK PHYSICS MODEL

3.1 Introduction to the Rock Physics Model

Understanding the complex structure of shales is challenging. Rock physics models allow us to predict valuable information about elastic and geomechanical properties of the reservoir. The Maxwell homogenization scheme is an approach that provides us with robust results (Maxwell, 1873). Sayers *et al.* (2015) examined the effect of kerogen content on anisotropy in the Eagle Ford Shale using the effective medium theory of Sevostianov *et al.* (2005). Recently, Sayers & Dasgupta (2019) used the Maxwell homogenization scheme to characterize unconventional reservoirs with varying mineralogy.

We present rock physics modeling results using the extended Maxwell homogenization scheme of Sevostianov (2014) for the Eagle Ford Shale. As an extension to previous works, we have included porosity and accounted for the shapes of multiple inclusions such as clay platelets, kerogen, fluid-filled pores, calcite and quartz to estimate the aspect ratio of embedded domain correctly. Furthermore, this novel rock physics model and workflow are used to characterize anisotropy and elastic properties of the clay matrix itself. This scheme is used to analyze geomechanical properties, seismic properties such as amplitude versus offset (AVO) and anisotropy in the reservoir. Core measurements from Wells D and N were used to constrain our modeling results along with well logs from Wells C and G. We propose using this method to better understand shales and represent the unconventional reservoirs comprehensively.

3.2 Mineralogy

The Eagle Ford is a carbonate-rich source rock. Since our survey area is located east of the San Marcos Arch, we do not observe the Upper Eagle Ford as discussed in Chapter 1. We focus on modeling the Lower Eagle Ford in this study. The Lower Eagle Ford, on

average, consists of 29% quartz, 40% calcite and 31% clay from Well C based on Figure 3.1. To better understand the distribution of the inorganic phase in Well C, one can refer to the ternary diagram in Figure 3.2. Since mineralogy is the base of our rock physics model, detailed information about mineralogical composition is necessary. Moreover, since kerogen and effective porosity have great influence on shales, they are used as inclusions to model their elastic contribution in the rock matrix.

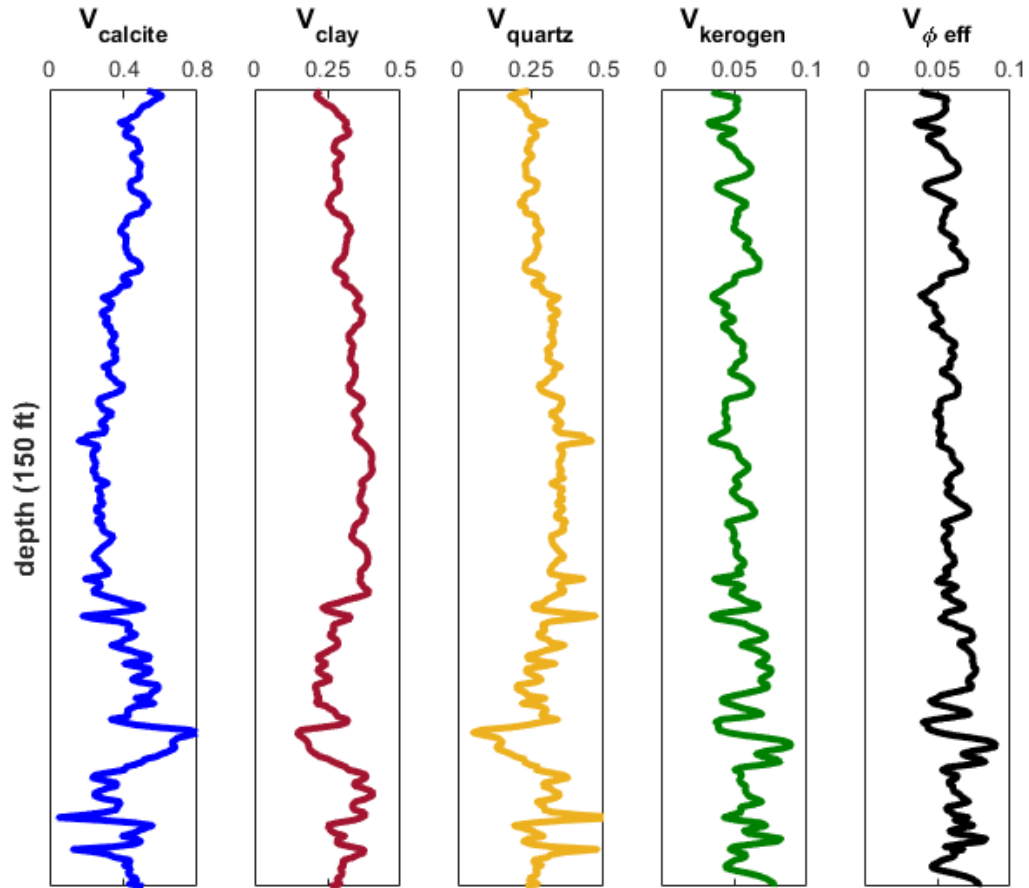


Figure 3.1: Mineralogical composition, kerogen content and effective porosity of the Eagle Ford Shale with depth obtained from Well C

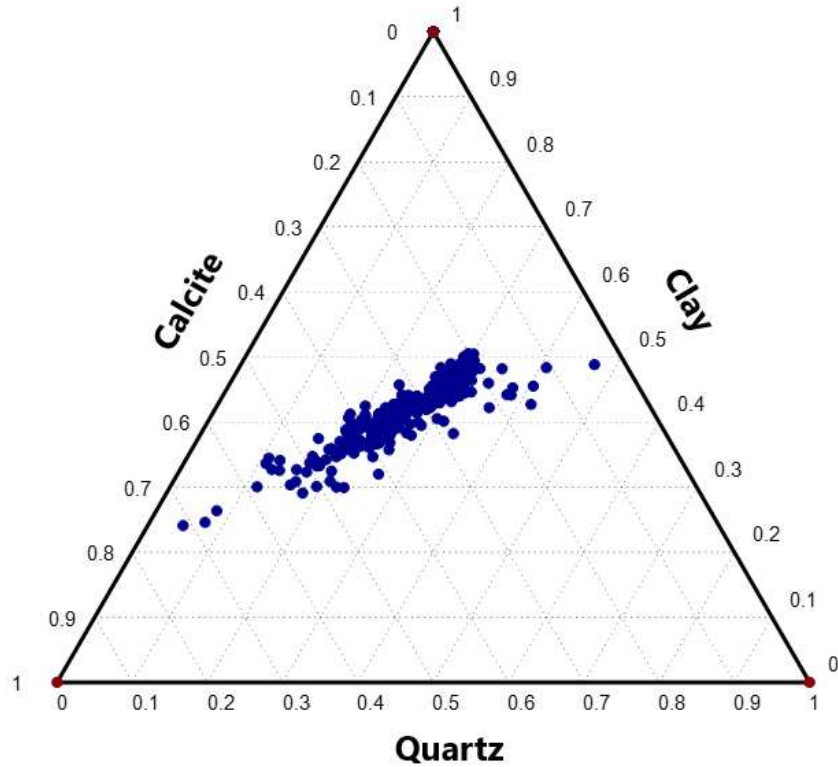


Figure 3.2: Ternary diagram of the mineralogical composition of the Eagle Ford Shale in volume fraction obtained from Well C

3.3 Reservoir and Fluid Properties

Based on the PVT (Pressure Volume Temperature) report we have from Well W, reservoir and fluid properties in the field are obtained. They are used to calculate bulk modulus and density of water and oil-gas in the reservoir so that fluid-filled pore inclusions in the model can be represented accurately. For this, the well-known and widely used empirical equations of Batzle & Wang (1992) are utilized. Table 3.1 present the results. Water salinity is 34021 ppm, and composed of 86% NaCl, 12% KCl and 2% CaCl₂. In the area of interest, oil gravity is approximately 50 API, which is consistent with Figure 3.3. Gas to oil ratio is 5996 Scf/STB. At reservoir conditions, temperature and pressure are 310 °F and 11800 psi, respectively. Pressure in the Eagle Ford varies considerably (Figure 3.4). Based on the pressure map, pressure in our area of interest may change, but I do not have enough data to

verify this variability since I only have one report from a well inside the survey area. Hence, PVT reports help us determine specific values of these properties to calculate bulk modulus and density of the fluids correctly. Since my research area is located between the oil and gas window, I estimate oil and gas mixture instead of having either as a pore fluid.

Table 3.1: Fluid properties of Eagle Ford using Batzle & Wang (1992) equations

Fluid Type	Bulk Modulus (GPa)	Density (g/cc)
Water	2.75	0.979
Combined Oil-Gas	0.355	0.445

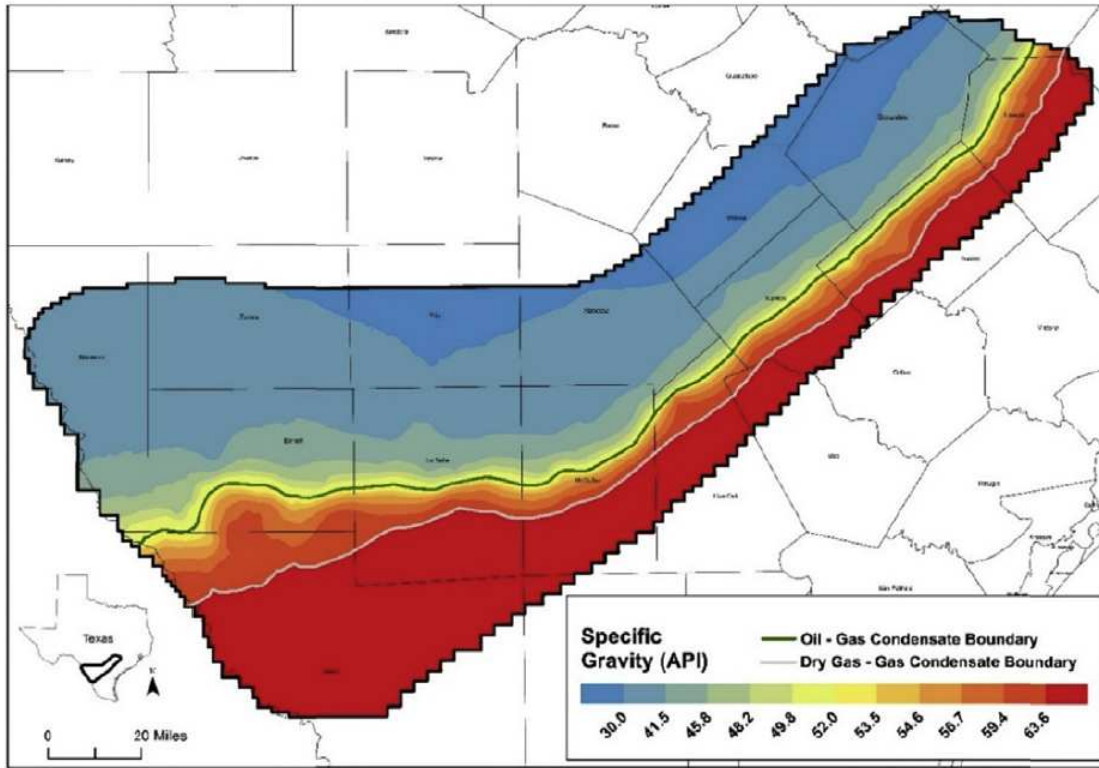


Figure 3.3: Liquid gravity map of Eagle Ford play (after Gherabati *et al.*, 2016).

In order to calculate the effective elastic properties of fluids, I use Voigt and Reuss elastic bounds for the bulk modulus of the fluid mixture. Equation 3.1 shows the stiff upper bound

3.4 Maxwell Homogenization Scheme

Maxwell (1873) original homogenization scheme has been reformulated for elastic composites by Sevostianov & Giraud (2013); Sevostianov & Kachanov (2014); Sevostianov (2014); Vilchevskaya & Sevostianov (2015); Sevostianov (2017). Sevostianov and his colleagues extended this model to transversely isotropic media, and they have utilized it to estimate elastic properties of materials such as fibers, cracks, composites, and interestingly bones in human body. With regard to rock physics, the Maxwell homogenization scheme is a novel approach.

This study investigates organic-rich shales using this scheme with novelties. To my knowledge, this is one of the first field data examples of this model used for rock physics. Figure 3.5 illustrates that multiple inhomogeneities can be represented as a fictitious domain of a certain shape (Ω). V denotes the volume of the matrix, while V^* represents the domain cut out in the shape of Ω . Elastic properties produced by multiple inhomogeneities inside the medium is equated with the fictitious domain with unknown properties in order to obtain effective properties in terms of stiffness and compliance contribution tensors as shown in 3.4 and 3.5.

$$\frac{V^*}{V} N_{eff} = \frac{1}{V} \sum_i V_i N_i \quad (3.4)$$

$$\frac{V^*}{V} H_{eff} = \frac{1}{V} \sum_i V_i H_i \quad (3.5)$$

where \mathbf{N} is the stiffness contribution tensor of inclusions, \mathbf{H} is compliance contribution tensor, V denotes volume of the rock matrix, V^* represents volume of cut out domain, and i is the number of inclusion.

Equation 3.6 is used to obtain effective stiffness coefficients, where \mathbf{N} is the stiffness contribution tensor of the inhomogeneities. Equation 3.7 is an alternative way to obtain the \mathbf{P} tensor in the shape of the representative volume (Sevostianov, 2014). Hill's tensor \mathbf{P} and \mathbf{Q} are interrelated (Sevostianov, 2014). \mathbf{C}_0 is the stiffness tensor of the rock matrix.

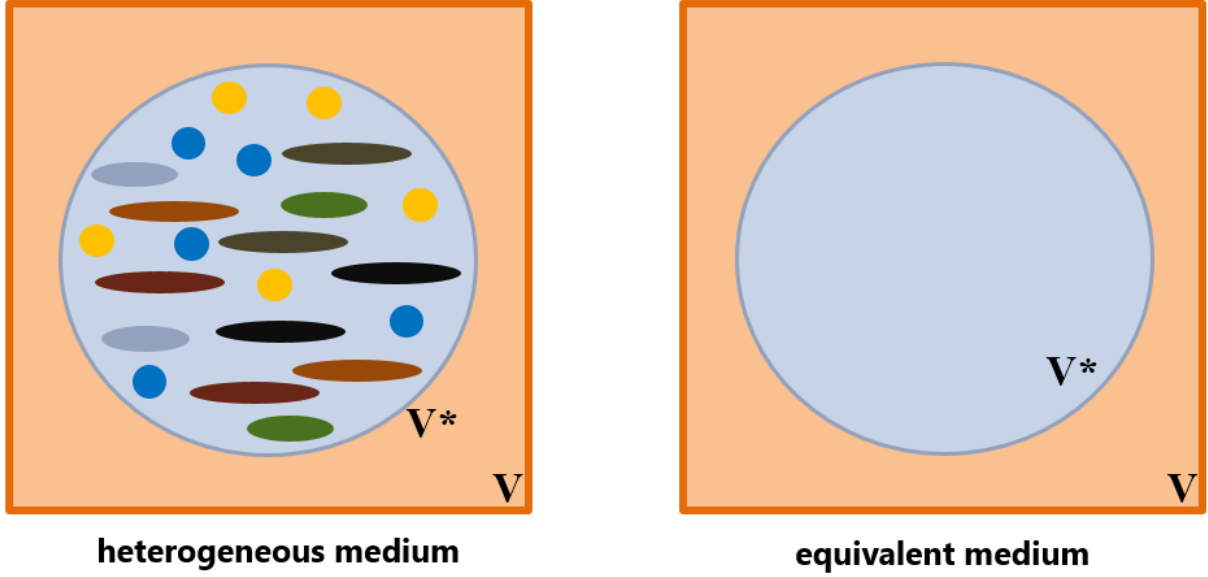


Figure 3.5: Illustration of "volume V " of the rock matrix and "volume V^* " of the cut domain with different inhomogeneties and aspect ratios on the left and, illustration of equivalent medium with unknown properties within the volume of V^* on the right.

$$\mathbf{C}_{\text{eff}} = \mathbf{C}_0 + \left\{ \left[\frac{1}{V^*} \sum_i V_i \mathbf{N}_i \right]^{-1} - \mathbf{P}_\Omega \right\}^{-1} \quad (3.6)$$

where C_0 is stiffness tensor of the background medium and

$$P_\Omega = S_0 : (J - Q_\Omega : S_0), \quad (3.7)$$

where $J_{ijkl} = (\delta_{ik}\delta_{ij} + \delta_{il}\delta_{kj})/2$ is the fourth-rank symmetric unit tensor, \mathbf{S}_0 is the compliance tensor of the rock matrix, and Q_Ω is Hill's compliance tensor calculated in the shape of effective inclusion domain (Ω).

$$P_{ijkl} = \int_{V^*} G_{ik,lj}(\mathbf{x} - \mathbf{x}') d\mathbf{x}'|_{(ij)(kl)} \quad (3.8)$$

where $G(\mathbf{x})$ is the Green's function for the anisotropic unbounded medium and the symbol parenthesis () stands for the symmetrization over corresponding indices. The integral is taken over the volume V^* meaning effective inclusion domain.

Maxwell's original work and Sayers & Dasgupta (2019)'s analysis assume the shape of the inclusion domain to be spherical. Because we use multiple inhomogeneities with different aspect ratios, Equation 3.9 should be taken into consideration to obtain the appropriate aspect ratio of Ω (Sevostianov, 2014). Otherwise, the choice of the aspect ratio can produce erroneous results (Berryman & Berge, 1996; Sevostianov, 2014). Here, Ω is assumed to be ellipsoidal (Figure 3.6).

$$\alpha_{(\Omega)} = \begin{cases} \sum_i V_i Q_{3333}^{(i)} / \sum_i V_i Q_{1111}^{(i)} & \text{if } \textit{oblate}, \\ \sum_i V_i P_{3333}^{(i)} / \sum_i V_i P_{1111}^{(i)} & \textit{otherwise}. \end{cases} \quad (3.9)$$

Here P and Q are components of Hill (1965)'s fourth-rank tensors. i represents the number of each inclusion, and V_i is the volume fraction of individual inhomogeneities.

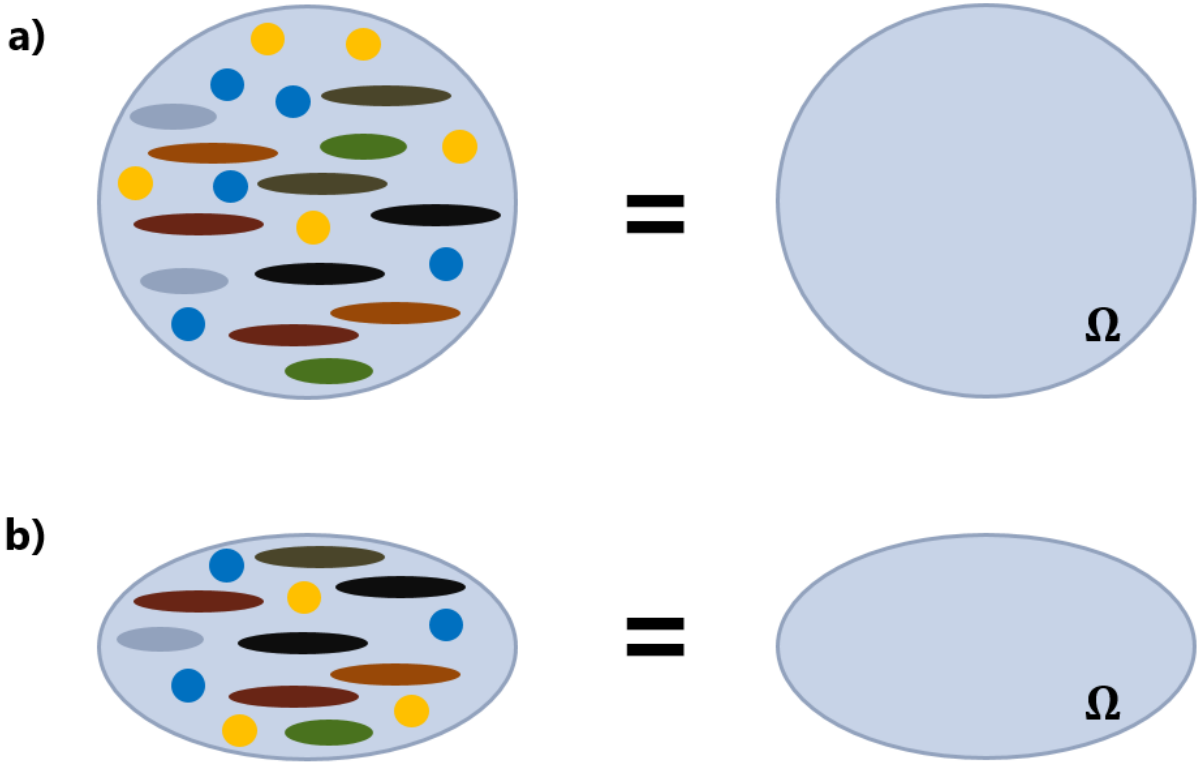


Figure 3.6: a) The shape of effective inclusion domain in Maxwell's original work and other previous studies b) The shape of effective inclusion domain suggested by Sevostianov and this study.

Sevostianov (2014) also claims that the extended Maxwell homogenization scheme would coincide with Kuster & Toksöz (1974)’s model if we were to choose spherical inclusion domain. In the extended Maxwell Homogenization scheme, the matrix itself and each individual inhomogeneity are isotropic; however, we introduce different inhomogeneities with certain aspect ratios into the medium, and this makes the structure anisotropic. Another important factor of this scheme is that it provides one with versatility regarding the structure of the matrix and inclusions. It allows one to insert not only isotropic but also anisotropic background and/or inclusions into the model. Derivations done by Sevostianov & Kachanov (2002); Sevostianov *et al.* (2005); Sevostianov (2014) are provided in the Appendices (A, B, and C). For this study, the aspect ratio of each inclusion is determined by $\alpha = c/a$, where c is the a_3 and a is $a_1 = a_2$ axis (Figure 3.7).

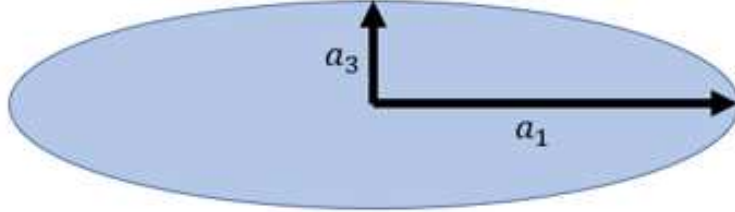


Figure 3.7: Aspect ratio of each inclusion defined by the ratio of a_3 over a_1 with x_3 and x_1 axes, respectively.

3.5 Estimation of Elastic Properties of the Rock

To use the rock physics model, one needs to know elastic properties of every individual mineral. However, elastic moduli of clay minerals vary significantly in contrast with well-established quartz and calcite. To estimate effective properties of clays as well as shales, mixture of different rock physics models and workflows have been used. Differential effective medium (DEM), self consistent approximation (SCA), and Backus averaging are the main

combined models for these purposes (Zhang *et al.*, 2019). However, the model presented in this thesis can handle all at once. One can estimate elastic properties of clay aggregates. Subsequently, clay aggregates and other components of the shale matrix can be used to model effective medium consistently with the model we develop. The detailed information is provided in the following two sections.

3.5.1 Clay Matrix

An XRD analysis of two wells (Well N and D) is provided by the vendor. The clay matrix consists of 41.75% illite-smectite mixture, 42.5% illite, 9.25% kaolinite and 6.5% chlorite minerals in Well N. Similarly, the clay matrix in Well D is composed of 43.5% illite-smectite mixture, 37.76% illite, 10.22% kaolinite and 8.52% chlorite minerals. For the rock physics model, I used the average of these two wells (Figure 3.8).

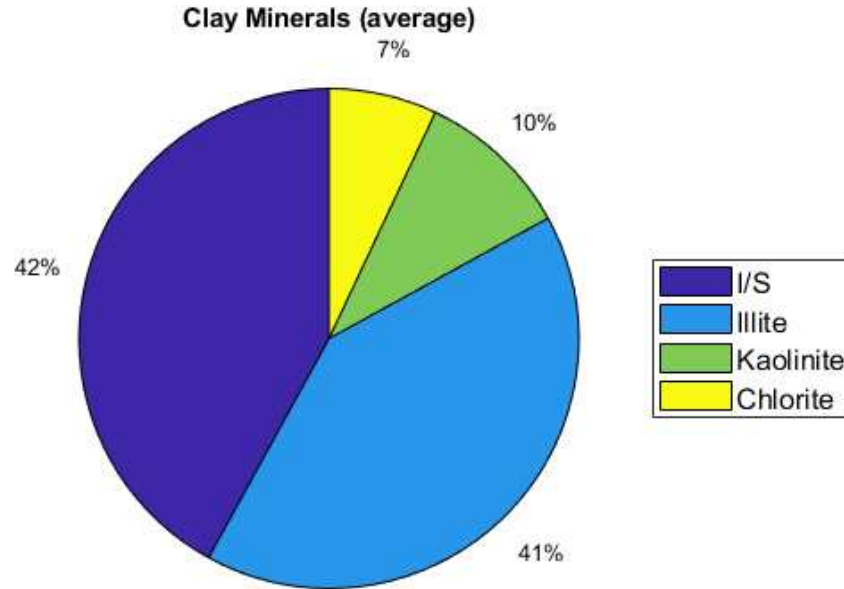


Figure 3.8: Clay matrix composition in the survey area from the core measurements provided by the vendor.

Clay minerals are mainly classified as 2:1 and 1:1 structure (Figure 3.9). Clays are a type of phyllosilicates. 2:1 structure can be described as the octahedral sheet sandwiched between two tetrahedral sheet, whereas 1:1 structure contains one tetrahedral and one octahedral sheet (Barton & Karathanasis, 2002). For instance, illite has 2:1 structure, while kaolinite has 1:1 structure. For this reason, assuming a homogeneous clay matrix is unrealistic since only one clay mineral does not exist in the basic structure of a clay matrix in the nature.

As for the properties of smectite and chlorite, one can observe different aspects related to their structure and water adsorption. Chlorite has a different structure of layering 2:1:1 compared to kaolinite and illite. Smectite shares the same structure with illite (2:1). However, since smectite has larger surface area, it is prone to retention of water. This is actually a problem called "clay swelling", and plays an important role in formation damage of hydrocarbon reservoirs (Wilson *et al.*, 2014). It is important to note that smectite can cause a decrease in permeability and issues with wellbore stability. The space between clay platelets holds water, weakly bound cations, salt and polar molecules, which lowers elastic stiffness coefficients of clay matrix. Illite is structurally very similar to muscovite. Yet, illite contains slightly more water than muscovite. Illite is very common in sedimentary basins as in the project area (41 % on average).

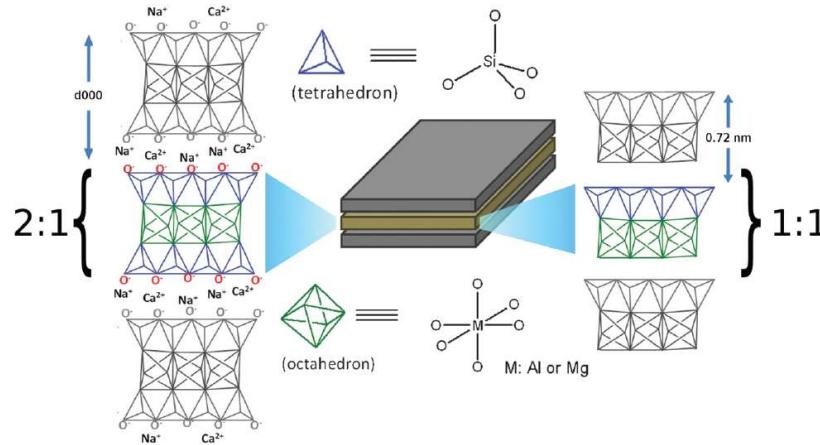


Figure 3.9: Structure of clay minerals, 2:1 structure on the left, 1:1 structure on the right and each layer consists of either structure in a deck of cards (after Castberg, 2014).

Another important aspect of clay minerals is that they are sometimes present in mixed layers. One of the most common mixed silicate layer is illite-smectite. This is of importance because the provided XRD analysis shows this mixture as one of the clay mineral components in our field. Illite-smectite mixture can be formed in different order systems such as R0, R1, R2 and R3. R stands for the German term "Reichweite", range or reach in English. If it is R0, it means illite-smectite mixture is not ordered, meaning randomly mixed. R1 mixture has the order of ISISISIS, and the name of this specific illite-smectite composition is called rectorite. That structure and ordering is what we observe in our area of interest. To exemplify, R3 would be ordered as IIS in this system. Figure 3.10 demonstrates how clay platelets are formed in different scales.

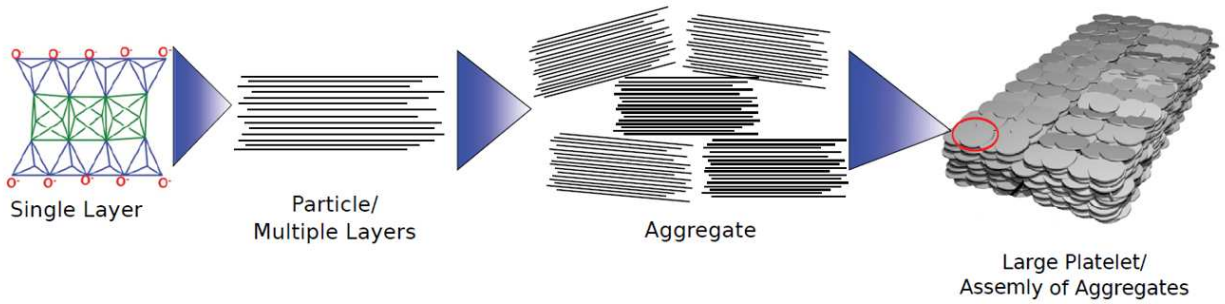


Figure 3.10: Schematic representation of clay platelets and how their diagenesis occur (modified from Castberg, 2014).

So as to model a clay matrix using Maxwell homogenization scheme, we need to know properties of inter-clay medium as well as composition of clay minerals. Bound water between clay platelets is used as background in the rock physics model. Volume fraction of bound water (ϕ_{bw}) can be found using Equation 3.10.

$$\phi_{bw} = \phi_{total} - \phi_{eff}. \quad (3.10)$$

Since total (ϕ_{total}) and effective porosity (ϕ_{eff}) of Well C are already provided by the vendor, volume of bound water can be readily estimated (Figure 3.11). I have also calculated

the ratio of clay-bound water to clay content, which shows around 8% bound water inside the clay matrix. This information is used to model inter-clay medium in this work.

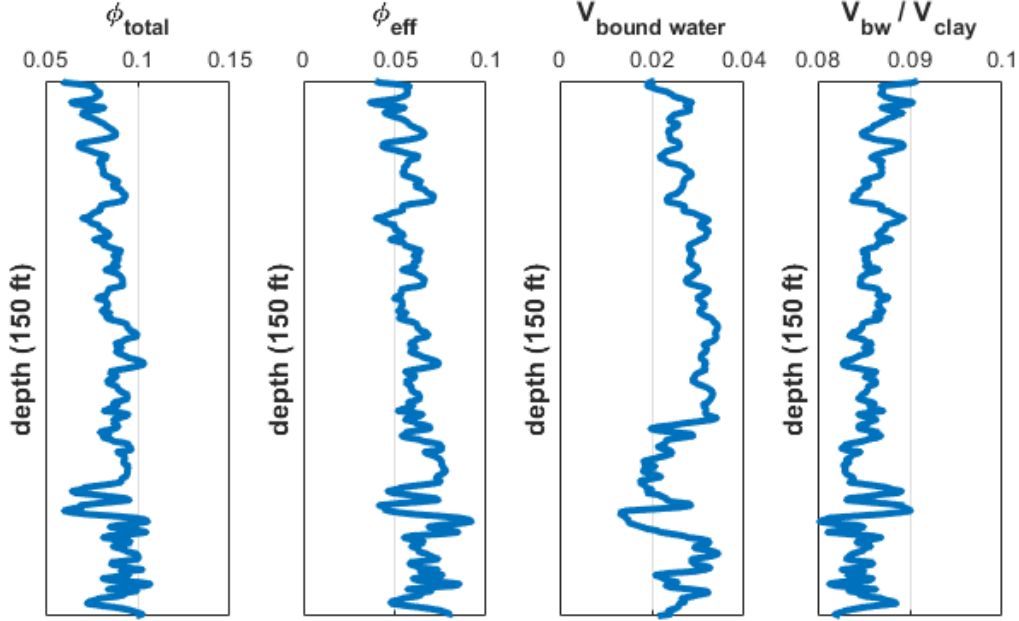


Figure 3.11: Volume fraction of total porosity and effective porosity in addition to calculated bound water volume and the ratio of bound water to clay content in Well C.

Now that we have inter-clay medium information, clay platelets can be modeled as ellipsoidal inclusions in the rock physics model using bulk and shear moduli in Table 3.2. Figure 3.12 illustrates the background matrix and clay platelets as inclusions. Each clay platelet is assumed to be isotropic in this study. This is actually a realistic assumption, because anisotropy at this scale is difficult to obtain. There are some studies examined elastic stiffness coefficients of clay minerals, but they generally make a core sample out of clay powder (Alexandrov & Ryzhova, 1961; Katahara, 1996; Vanorio *et al.*, 2003). Such estimation results in higher stiffness coefficients and higher anisotropy than what is observed in clay matrix (Militzer *et al.*, 2011). This is reasonable because inter-clay medium lowers elastic properties of clay aggregates substantially.

I already constrain the volume fraction of minerals, kerogen and porosity information from Well C. However, I do not have a direct information regarding the aspect ratio of each constituent in Eagle Ford shale to apply to my rock physics model. So, a grid-search is performed to obtain the best fit with aspect ratios of clay platelets and bulk and shear moduli of background water-like medium using the objective function shown in equation 3.11. I minimize RMS error using three independent stiffness coefficients obtained from dipole sonic logs of Well C and the predicted coefficients from the rock physics model. This allows me to obtain best-fit aspect ratios of different inclusions in the research area.

$$\mathbf{J} = \sqrt{\langle C_{33}^{well} - C_{33}^{model} \rangle^2 + \langle C_{55}^{well} - C_{55}^{model} \rangle^2 + \langle C_{66}^{well} - C_{66}^{model} \rangle^2} \quad (3.11)$$

where the brackets " $\langle \rangle$ " are mean average. Superscripts (well) and (model) represent the corresponding stiffness coefficients obtained from dipole sonic logs of Well C and the extended Maxwell Homogenization scheme, respectively.

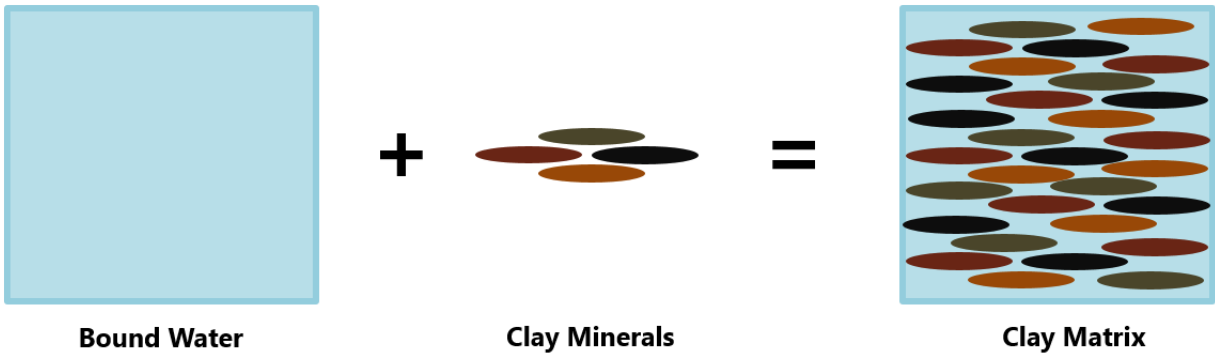


Figure 3.12: Illustration of how to obtain clay matrix using the rock physics model

Table 3.2: Isotropic elastic moduli of clay minerals (a = Katahara (1996), b = Wang *et al.* (2001))

Materials	K (GPa)	μ (GPa)
Kaolinite ^a	55.5	31.8
Chlorite ^a	54.3	30.2
Illite ^a	52.3	31.7
Illite – Smectite ^b	37	18.2

The aspect ratio is searched between 0 and 0.99. Since the background medium is expected to be water-like medium, I test values for the bulk modulus between the values of 1 and 5, and shear modulus between 0 and 0.5. The best fit aspect ratio of clay platelets is found to be 0.69. This value is much higher than what is expected. Aspect ratio of clay minerals are known to be very low (between 0.05 to 0.1) (Hornby *et al.*, 1994). I assert that our model tries to compensate for overpredicted anisotropy by raising aspect ratio, since clay platelets are assumed to align perfectly in this model. Additionally, there may be some intrinsic error in well log measurements or processing that can lead to this discrepancy. It is known that clay platelets are not perfectly aligned due to regional diagenesis. However, since we do not have SEM images of clay minerals from our field, we would need to make an unnecessary assumption of clay alignment in the shale using an orientation distribution function. The bulk modulus and shear moduli of water-like inter-clay medium are found to be 1.71 GPa and 0.3 GPa, respectively. These are in agreement with the work of Sayers & den Boer (2018). The results following this workflow can be found in Figure 3.13. Compared to some other studies from the literature, the results obtained using Maxwell homogenization scheme are reasonable (Table 3.3).

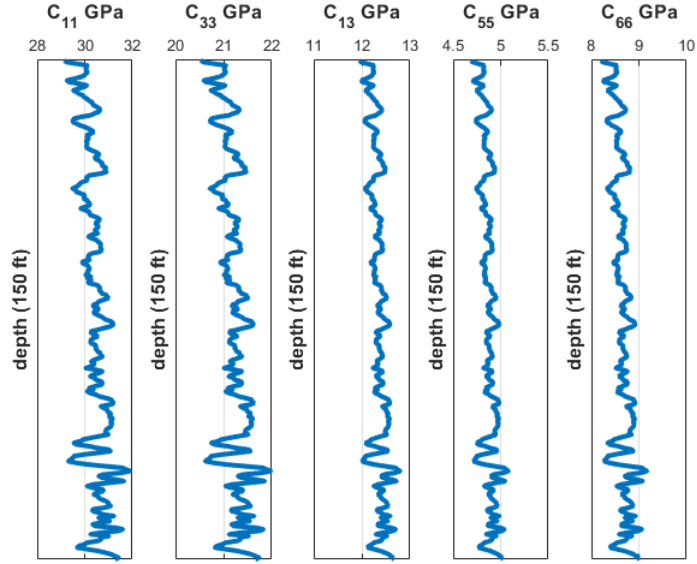


Figure 3.13: Five independent stiffness coefficients of clay matrix found within the Eagle Ford section.

Table 3.3: Stiffness coefficients of clay matrix compared to analyses from literature (A = Ortega *et al.* (2007), B = Bayuk *et al.* (2007), C= Sayers (2005))

Coefficients	A	B	C	Results from this study
C_{11} (GPa)	44.9	23.7	40	29.13 - 31.91
C_{33} (GPa)	24.2	8.5	16.8	20.52 - 21.99
C_{13} (GPa)	18.1	3.1	9	11.95 - 12.79
C_{55} (GPa)	3.7	0.8	2.7	4.69 - 5.08
C_{66} (GPa)	11.6	5.7	13.1	8.2 - 9.17

Estimating elastic properties of clay matrix has always been an issue in the literature. Since lab measurements are very limited on clay matrix, different methods have been used to obtain this information. For instance, Sayers (2005) and Bayuk *et al.* (2007) used the same data set from the study of Greenhorn shale of Jones & Wang (1981). Yet, even though

both studies used the same dataset and rock physics models (DEM and SCA) to invert for the properties of clay matrix, they came up with different results. Measuring the elastic properties of clay matrix in the lab or inverting for them using different rock physics models are non-trivial issues. Elastic properties of clay aggregates vary significantly depending on the composition and particle alignment. Therefore, I suggest estimating a tailored clay matrix for any unconventional reservoir that is of interest, and this clay matrix can be thoroughly estimated using Maxwell homogenization scheme.

Having calculated stiffness tensor of the clay matrix in VTI media, isotropic bulk (K) and shear (μ) moduli can be also obtained using the equations 3.12 to 3.17. This allows us to compare our modeling results with equivalent literature analyses (Table 3.4). Bulk and shear moduli of clay matrix estimated using Hill (1963); Reuss (1929); Voigt (1910) are shown in Figure 3.14. It is noted that upper bound (Voigt) and lower bound (Reuss) have very close values. Hill's average of bulk modulus ranges from 18.97 to 30.48, and that of shear modulus varies from 7.86 to 12.83.

$$K_v = \frac{1}{9}(2C_{11} + C_{33}) + \frac{2}{9}(C_{12} + 2C_{13}) \quad (3.12)$$

$$\mu_v = \frac{1}{15}(2C_{11} + C_{33}) - \frac{1}{15}(C_{12} + 2C_{13}) + \frac{1}{5}(2C_{55} + C_{66}) \quad (3.13)$$

$$K_r = \frac{1}{A(C_{11} + C_{12} + 2C_{33} - 4C_{13})} \quad (3.14)$$

$$\mu_r = \frac{15}{2A(2(C_{11} + C_{12}) + 4C_{13} + C_{33}) + 6(1/C_{55} + 1/C_{66})} \quad (3.15)$$

where $A = 1/(C_{33}(C_{11} + C_{12}) - 2C_{13}^2)$

$$K_{vrh} = \frac{1}{2}(K_v + K_r) \quad (3.16)$$

$$\mu_{vrh} = \frac{1}{2}(\mu_v + \mu_r) \quad (3.17)$$

where K_v , K_r , K_{vrh} are bulk modulus calculated using Voigt bound, Reuss bound and Hill's average, respectively, and μ_v , μ_r , μ_{vrh} are shear modulus estimated using Voigt bound, Reuss bound and Hill's average, respectively.

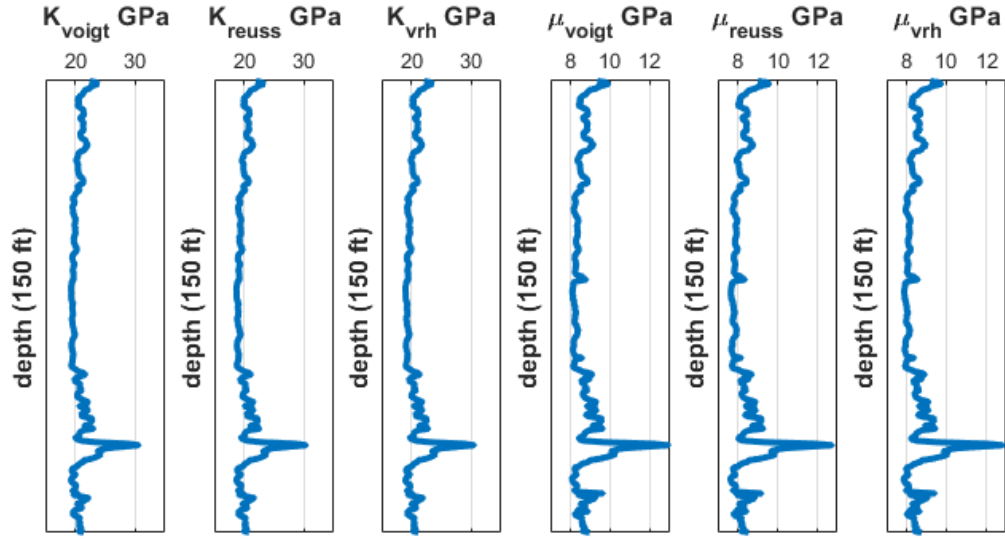


Figure 3.14: Bulk and shear moduli of clay matrix estimated using Voigt bound, Reuss bound and Hill's average

Table 3.4: Comparison of isotropic elastic moduli of clay matrix (the results from the rock physics model shown at the bottom)

References	K (GPa)	μ (GPa)
Mavko <i>et al.</i> (2009)	25	9
Vanorio <i>et al.</i> (2003)	12	6
Hornby <i>et al.</i> (1994)	22.9	10.6
Berge & Berryman (1995)	21.4	6.7
Ortega <i>et al.</i> (2007)	23.9	6.7
<i>VRH average of this study</i>	<i>20.32</i>	<i>8.42</i>

Modeling results of Maxwell homogenization scheme in transversely isotropic media can be approximated to isotropic bulk and shear moduli using VRH average. In comparison with the results from literature, our modeling results provide promising and consistent bulk and shear moduli as demonstrated in Table 3.4. In contrast to other effective elastic models, the

Maxwell homogenization scheme is in compliance with Hashin-Shtrikman bounds (Sevostianov & Giraud, 2013). As long as one does not violate the Hashin Shtrikman bounds, the volume fraction of inclusion or background matrix is unimportant. To demonstrate this, Hashin & Shtrikman (1963) bounds are utilized to obtain upper and lower bounds of bulk and shear moduli using water-like medium and four different clay minerals. Equations 3.18 to 3.22 are provided for this purpose.

$$K_{HS}^- \equiv \Lambda(\mu_{min}) \leq K_{eff} \leq \Lambda(\mu_{max}) \equiv K_{HS}^+, \quad (3.18)$$

$$\mu_{HS}^- \equiv \Gamma(\zeta(K_{min}, \mu_{min})) \leq \mu_{eff} \leq \Gamma(\zeta(K_{max}, \mu_{max})) \equiv \mu_{HS}^+, \quad (3.19)$$

where the functions Λ , Γ and ζ are calculated as follows

$$\Lambda(\mu) \equiv \left(\sum_{i=1}^N \frac{v_i}{K_i + \mu} \right)^{-1} - \mu, \quad (3.20)$$

$$\Gamma(\zeta) \equiv \left(\sum_{i=1}^N \frac{v_i}{\mu_i + \zeta} \right)^{-1} - \zeta, \quad (3.21)$$

$$\zeta(K, \mu) = \frac{\mu}{6} \left(\frac{9K + 8\mu}{K + 2\mu} \right). \quad (3.22)$$

Here, K_{eff} , K_{HS}^- and K_{HS}^+ are the effective bulk modulus, lower bound of HS and upper bound of HS, respectively. μ_{eff} , μ_{HS}^- and μ_{HS}^+ represent the same notation for shear modulus. N is the number of elements. v_i is volume fraction of each element. Hashin & Shtrikman (1963) provides the narrowest possible bounds for a multi-phase composite.

Figure 3.15 demonstrates and proves that modeling results of clay-water composite using Maxwell homogenization scheme in this study do not violate Hashin-Shtrikman bounds. So, the quality control of this analysis is done readily. It is also evident that one can use this scheme and workflow to model clay matrix in any sedimentary rocks.

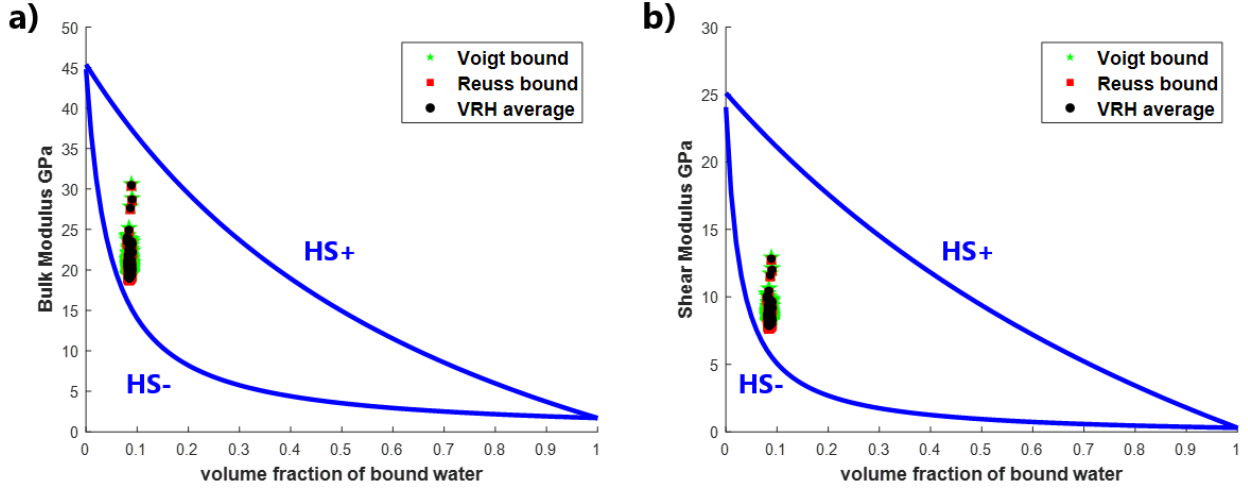


Figure 3.15: a) Upper (HS+) and lower (HS-) Hashin-Shtrikman bounds of bulk modulus of water-clay composite with overlain Maxwell homogenization scheme results. b) Upper and lower HS bounds of shear modulus of water-clay composite with overlain Maxwell homogenization scheme results

3.5.2 Shale Matrix

Since clay platelets are connected to each other, clay minerals fabricate load-bearing skeleton of shales (Hornby *et al.*, 1994). Hence, estimated clay stiffness coefficients are used as background matrix to model Eagle Ford shale. The rest are modeled as inclusions with different aspect ratios (Figure 3.16). For instance, quartz and calcite are known to be isotropic minerals, and represented as spherical inclusions in this model. The other two inclusions are kerogen and fluid-filled pores. Section 3.1 shows how to obtain effective moduli of fluid phases. For kerogen, the values from Table 3.5 are used. I did a grid search in order to find best fit of aspect ratios of kerogen and pores using Equation 3.11. Using this objective function, I minimize the RMS error of C_{33} , C_{55} , and C_{66} between the actual dipole sonic log values and my modeling results so that I obtain aspect ratio estimates of each inclusion for the Eagle Ford layer. The best fit aspect ratios for kerogen and fluid-filled pores are 0.48 and 0.35, respectively. This result is reasonable because Sone & Zoback (2013) showed that Eagle Ford inclusions have the lowest aspect ratio among all shale samples examined from various

reservoirs. Additionally, core photos from Well L is compatible with these assumptions and analyses (Figure 3.17).

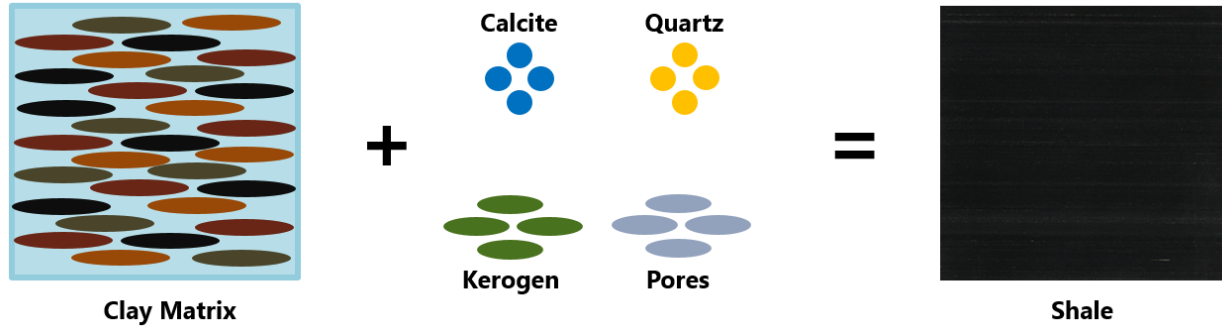


Figure 3.16: Modeling of Eagle Ford shale, clay matrix used as a background medium and quartz, calcite, kerogen and fluid-filled pores modeled as inclusions

Vitrinite reflectance ($\% R_0$) of kerogen is around 1.4 in the area of interest based on the core analysis provided by the vendor. This information allows us to estimate density of kerogen depending on thermal maturity (Craddock *et al.*, 2019). Using the values from Table 3.5, one can model shale matrix using Maxwell homogenization scheme comprehensively.

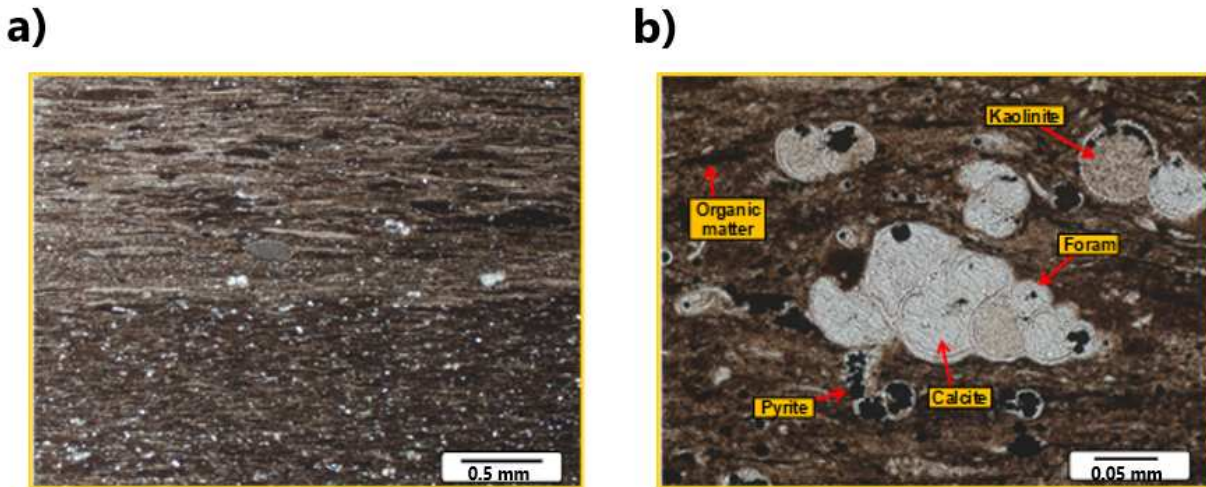


Figure 3.17: Core photos of Well L provided by the vendor. a) highly laminated Eagle Ford shale structure. b) organic matter with low aspect ratio (kerogen) and spherical calcite particles.

Table 3.5: Elastic moduli and densities of various minerals and fluids (a = Mavko *et al.* (2009), b = Bandyopadhyay (2009), c = Craddock *et al.* (2019))

Materials	K (GPa)	μ (GPa)	Density (g/cm ³)
Quartz ^a	37	44	2.65
Calcite ^a	70.2	29	2.71
Kerogen	5 ^b	3 ^b	1.45 ^c

Figure 3.18 shows the agreement between the rock physics model results and well log data. Root mean square (RMS) error using the objective function in Equation 3.11 is 3.21 GPa. This is a reasonable error compared to core measurements, well log analysis or seismic properties.

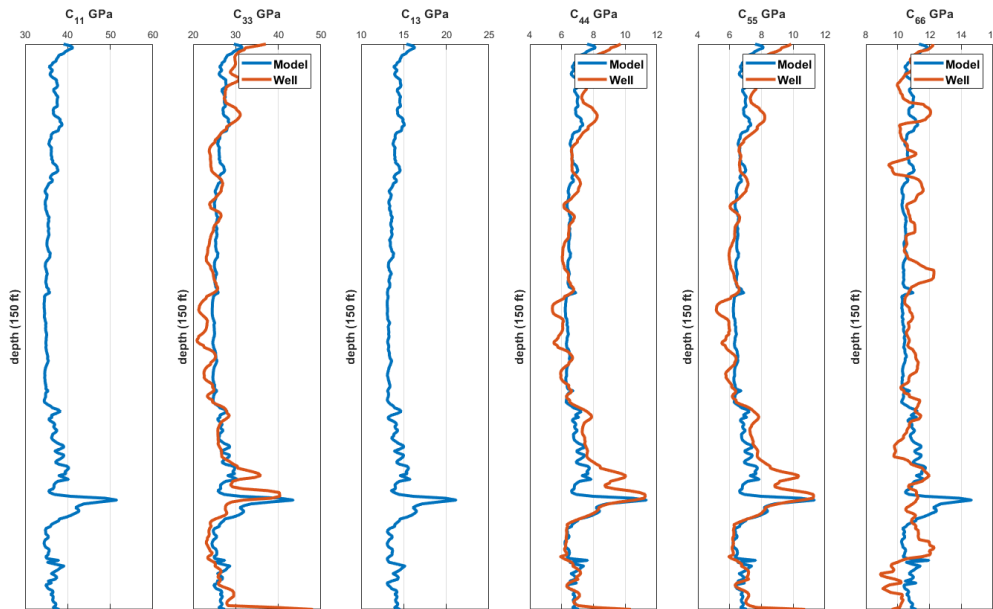


Figure 3.18: Five independent stiffness coefficients of shale matrix within the Eagle Ford section constrained by C_{33} , C_{55} and C_{66} obtained by dipole sonic logs (note that $C_{44} = C_{55}$ in VTI media)

My rock physics modeling results are constrained by dipole sonic logs. I show the match between modeling results and directly calculated C_{33} , C_{44} , C_{55} and indirectly calculated C_{66} . Additionally, I calculate C_{11} and C_{13} using my model. This is important because these two stiffness coefficients help calculate anisotropy parameters.

3.6 On the Shape of Effective Inclusion

I emphasize the importance of the shape of effective inclusion domain throughout this thesis. Berryman & Berge (1996); Sevostianov (2014) also pointed out that the choice of aspect ratio may have significant effect on the results. In order to illustrate this issue, I have used the same model with same parameters, and calculated five independent stiffness coefficients of the rock matrix using the formula given by Sevostianov (2014) and calculated spherical assumption in both clay matrix and shale matrix. As expected, the spherical aspect ratio assumption of the effective inclusion domain significantly changes the results (Figure 3.19).

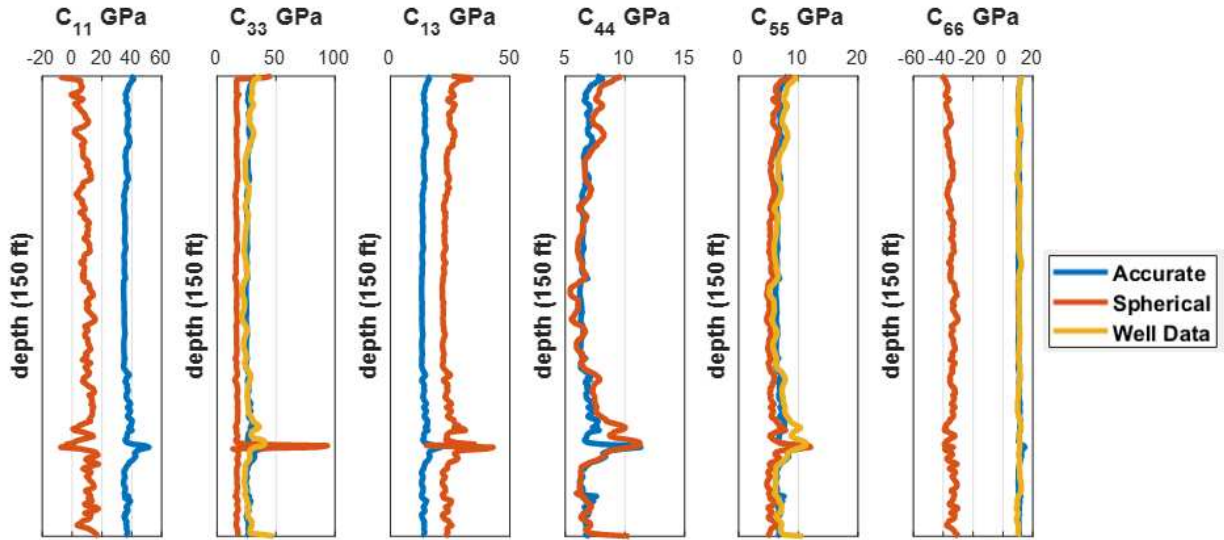


Figure 3.19: Five independent stiffness coefficients of shale matrix within the Eagle Ford section comparison of suggested aspect ratio calculation with spherical assumption

If one were to use this model with certain assumption, I assume that matching field data would not be possible based on this results. This issue should be addressed, and the shape

of effective inclusion should be taken into account so as to obtain robust results. This is one of the main points and contributions of this study.

3.7 Anisotropy of Clay and Eagle Ford Shale

We obtain effective stiffness coefficients of the rock in a transversely isotropic medium using the Maxwell homogenization scheme. Equation 3.23 represents the stiffness tensor in a VTI medium. Thomsen (1986) introduced very intuitive notations for the anisotropy parameters shown in Equations 3.24, 3.25 and 3.26 . Using Thomsen parameters, we can observe the variation of anisotropy within the reservoir. In addition to Thomsen's ϵ , γ and δ anisotropy parameters, Alkhalifah & Tsvankin (1995) anisotropy parameter η is also calculated using Equation 3.27. In the common two indices notation (Voigt, 1910; Nye, 1985), C_{ijkl} 4th rank tensor can be represented as C_{ij} using $()_{11} \rightarrow ()_1$, $()_{22} \rightarrow ()_2$, $()_{33} \rightarrow ()_3$, $()_{23} \rightarrow ()_4$, $()_{13} \rightarrow ()_5$, $()_{12} \rightarrow ()_6$.

$$\mathbf{C}^{(\mathbf{VTI})} = \begin{pmatrix} C_{11} & C_{12} & C_{13} & 0 & 0 & 0 \\ C_{12} & C_{11} & C_{13} & 0 & 0 & 0 \\ C_{13} & C_{13} & C_{33} & 0 & 0 & 0 \\ 0 & 0 & 0 & C_{55} & 0 & 0 \\ 0 & 0 & 0 & 0 & C_{55} & 0 \\ 0 & 0 & 0 & 0 & 0 & C_{66} \end{pmatrix} \quad (3.23)$$

where $C_{12} = C_{11} - 2C_{66}$. In VTI media, there are five independent stiffness coefficients. Since we already obtain those in previous sections, now anisotropy parameters for clay matrix and shale can be calculated.

$$\epsilon = \frac{C_{11} - C_{33}}{2C_{33}}, \quad (3.24)$$

$$\gamma = \frac{C_{66} - C_{55}}{2C_{55}}, \quad (3.25)$$

$$\delta = \frac{(C_{13} + C_{55})^2 - (C_{33} - C_{55})^2}{2C_{33}(C_{33} - C_{55})}. \quad (3.26)$$

$$\eta = \frac{\epsilon - \delta}{1 + 2\delta} \quad (3.27)$$

Figure 3.20 shows high anisotropy values for the clay matrix. It is also noteworthy that there is a very good linear relationship among anisotropy parameters calculated for clay matrix itself (Figure 3.21). This could possibly help us determine any of the anisotropy parameters in this area if we have information regarding one of them. Compared to anisotropy of clay matrix itself, Eagle Ford shale has lower anisotropy (Figure 3.22). Good correlation between ϵ and γ is witnessed within Eagle Ford section; however, the same linear trend is not observed between other anisotropy parameters for Eagle Ford shale using rock physics model (Figure 3.23). With respect to clay content and anisotropy relationship, one can see a clear trend between increasing anisotropy parameters of ϵ , γ , and δ and increasing clay content in Eagle Ford shale (Figure 3.24). Yet, there is no linear relationship between δ and increasing clay content. This could suggest that using empirical relationship or coefficients to obtain δ parameter using others is not viable even though unconventional industry tend to do so due to directional measurement difficulties. In this case, rock physics model is quite helpful to obtain this information with ease.

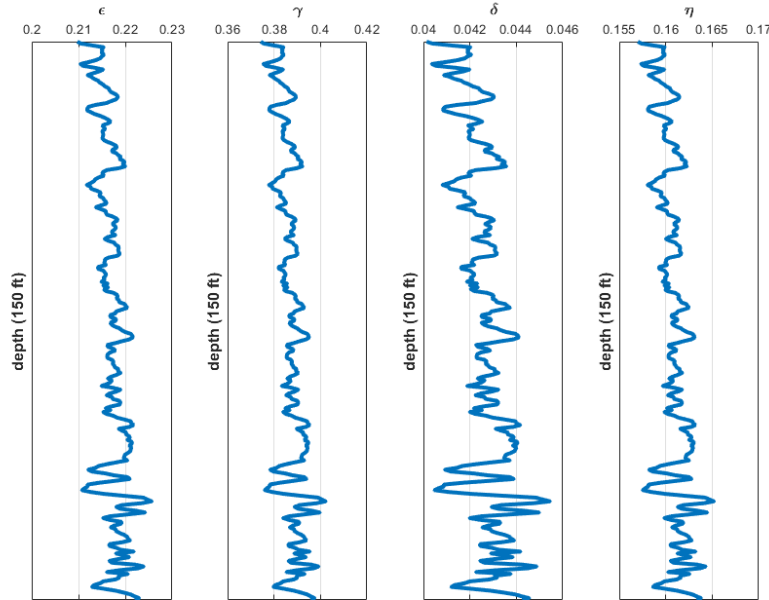


Figure 3.20: Anisotropy of clay matrix obtained using Maxwell homogenization scheme within the Eagle Ford section

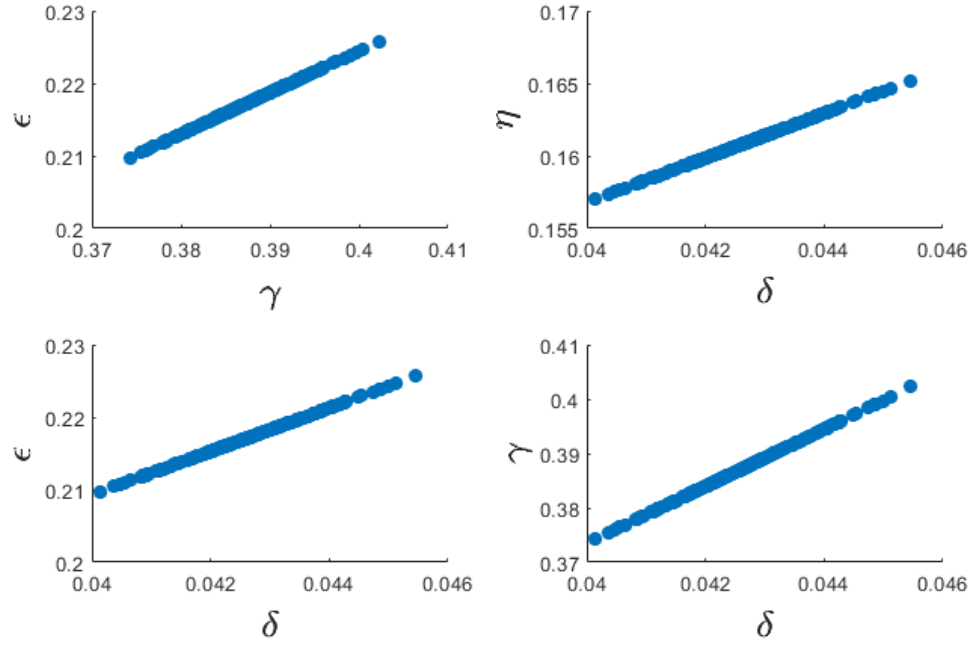


Figure 3.21: Cross-plots of different anisotropy parameters calculated for clay matrix

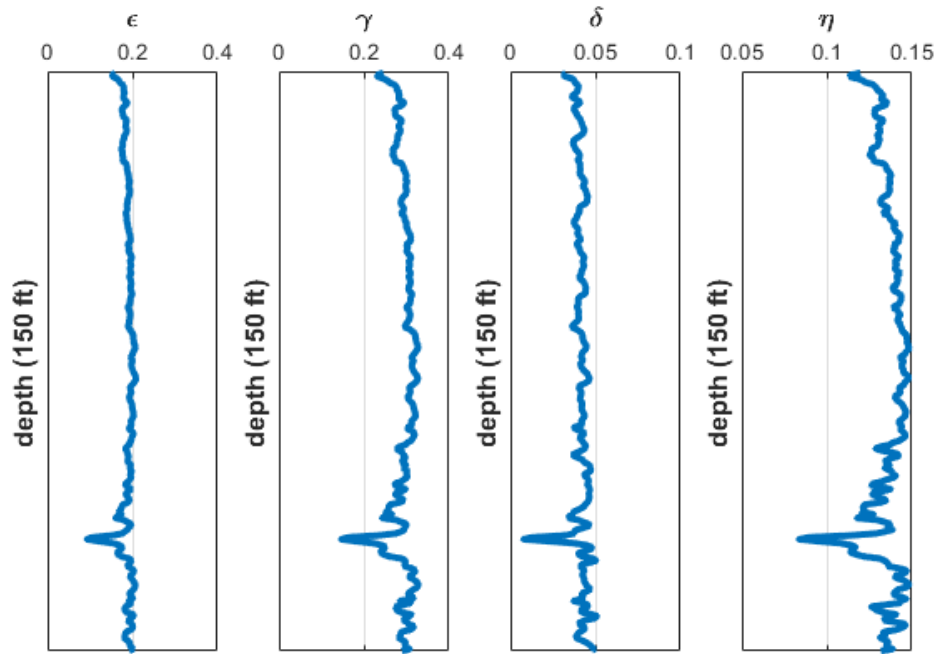


Figure 3.22: Anisotropy of Eagle Ford shale obtained using Maxwell homogenization scheme

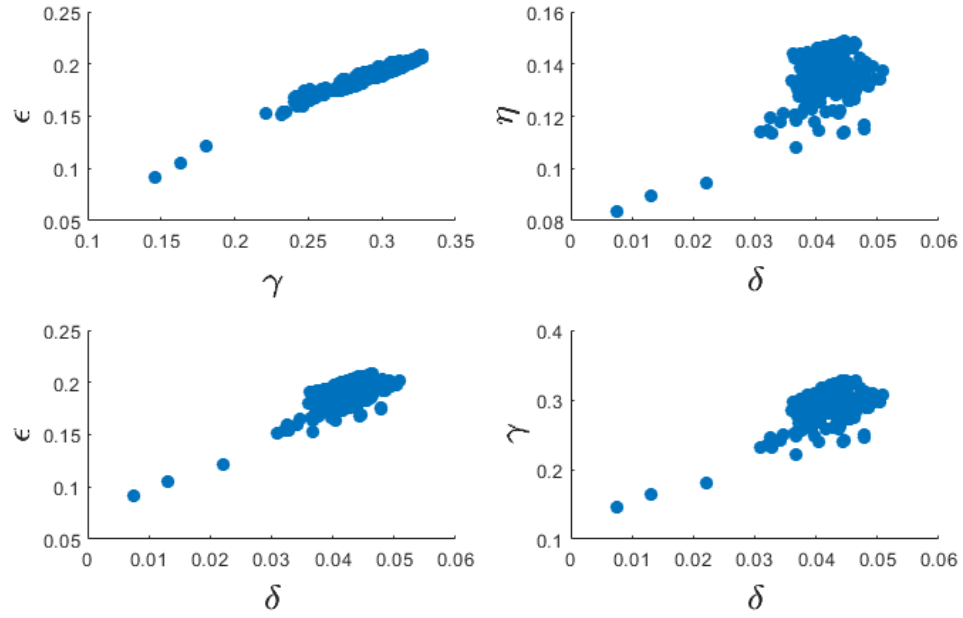


Figure 3.23: Cross-plots of different anisotropy parameters calculated for Eagle Ford shale

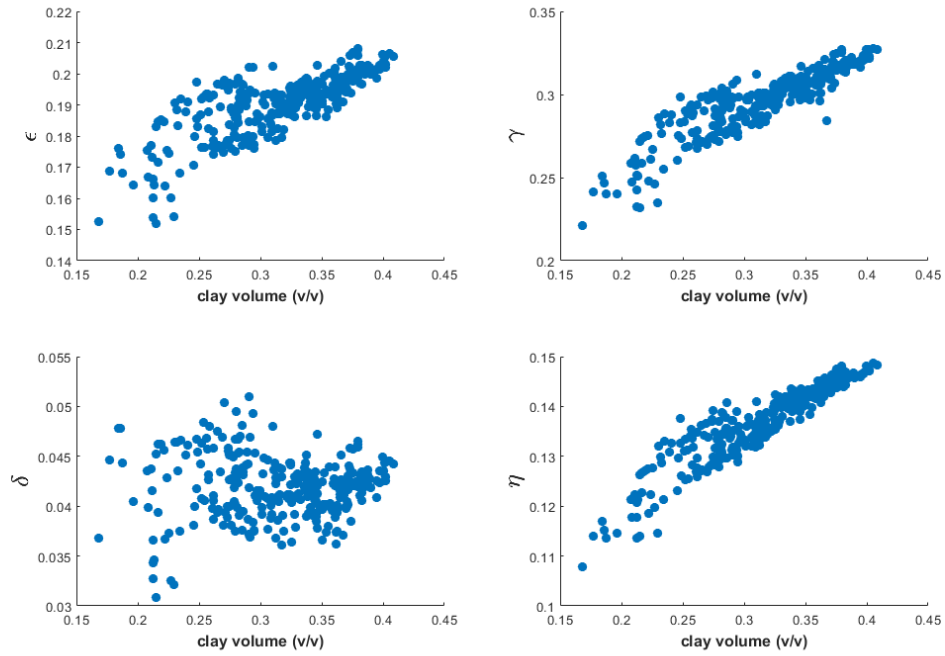


Figure 3.24: Relationships between anisotropy parameters and clay content within Eagle Ford section

3.8 Velocity Analysis

With the ease of Equations 3.28 and 3.31, we can easily compute the P- and S- wave velocities in both vertical and horizontal directions in VTI media. Vertical velocities are slower than horizontal ones because of anisotropy within Eagle Ford shale. Figure 3.25 shows a reasonable match of modeling results with the well logs. Root mean square error of vertical P-wave velocity is 554.17 ft/s while that of vertical S-wave velocity is 313.48 ft/s. Reasonable error range is seen within 150-foot Eagle Ford section between modeling results and actual well log data. Vertical and horizontal velocities are

$$V_{P0} = \sqrt{\frac{C_{33}}{\rho}}, \quad (3.28)$$

$$V_{P90} = \sqrt{\frac{C_{11}}{\rho}}, \quad (3.29)$$

$$V_{S0} = \sqrt{\frac{C_{55}}{\rho}}, \quad (3.30)$$

$$V_{S90} = \sqrt{\frac{C_{66}}{\rho}}, \quad (3.31)$$

where V_{P0} and V_{P90} are vertical and horizontal P-wave velocities, respectively. V_{S0} denotes Sv wave mode, whereas V_{S90} represents Sh wave mode. Here ρ is bulk density of the rock. Limited acoustic core measurements from the area of interest provided by the vendor are shown in Table 3.6. Well D has only one acoustic core measurement in vertical direction under 2070 psi of confining pressure and 2070 psi of axial pressure. Well N has three acoustic core measurements under 750 psi of confining pressure and 100 psi of axial pressure. Since these measurements are from different wells and taken under different pressure conditions by the vendor, they are not helpful for validating the modeling results.

Average vertical P-wave velocity is 10634 ft/s, whereas horizontal P-wave velocity is 12482 ft/s based on the rock physics modeling results. Horizontal and vertical shear wave velocities are 6778 ft/s and 5380 ft/s on average, respectively. Figure 3.26 shows estimated horizontal

P and S wave velocities within Eagle Ford section.

Table 3.6: Acoustic core measurements from two different wells provided by the vendor

Core number	V_{P0} (ft/s)	V_{S0} (ft/s)	V_{P90} (ft/s)	V_{S90} (ft/s)	ρ_b (g/cc)
Well D-1V	11905	6820	-	-	2.38
Well N-44H	-	-	14927	8834	2.496
Well N-54H	-	-	14848	8765	2.484
Well N-86H	-	-	14985	9033	2.564

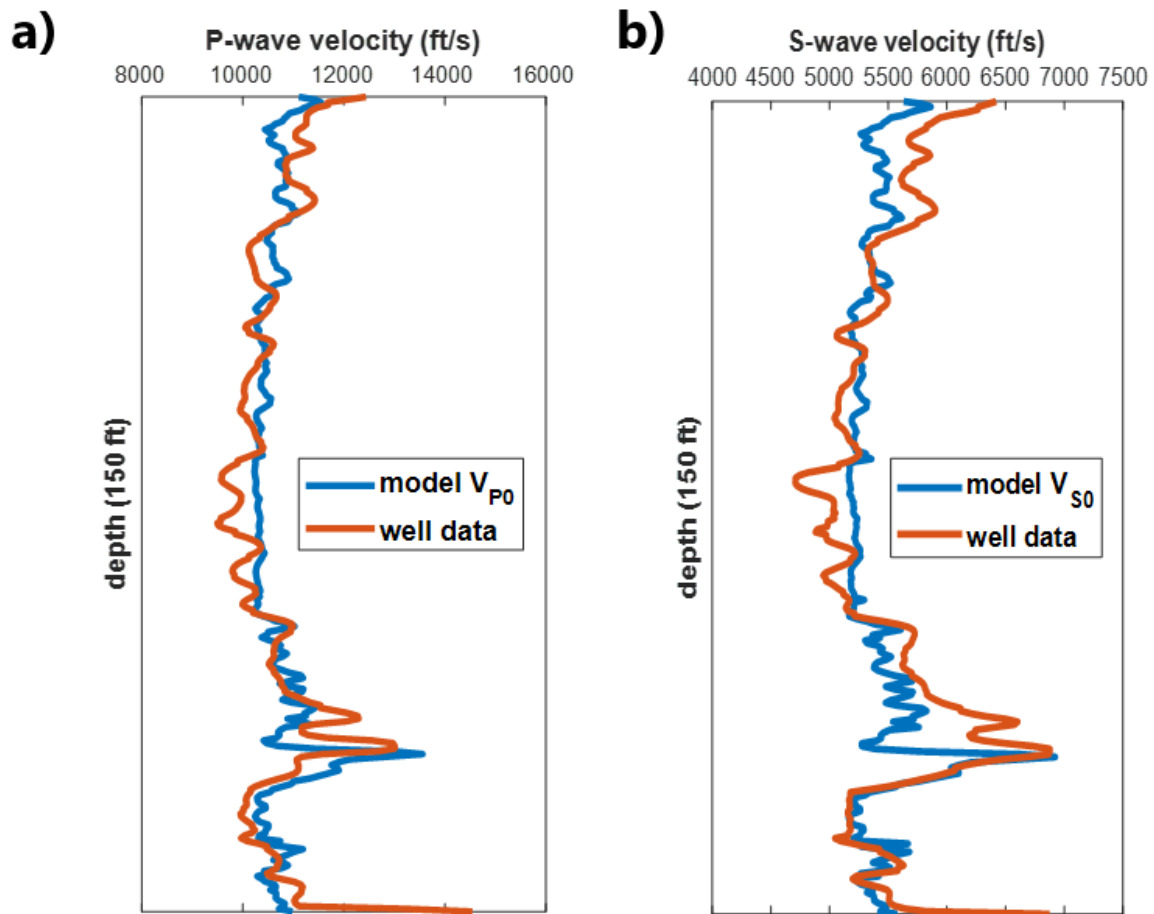


Figure 3.25: a) Vertical P-wave velocity b) Vertical S-wave velocity estimation using rock physics model compared to well logs

Directional dependence of P- and S-wave velocities are important, because anisotropic information that one can obtain can improve accuracy in surface and borehole microseismic event location applications.

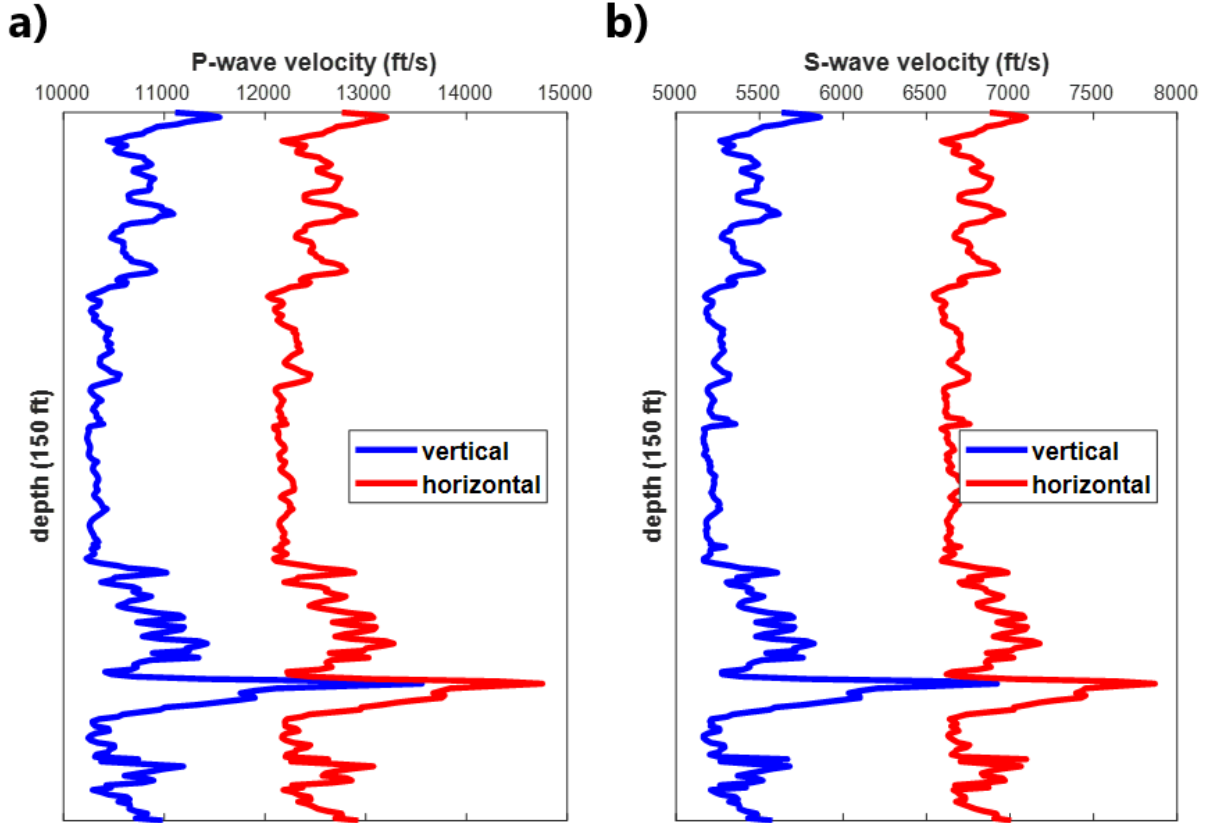


Figure 3.26: a) Horizontal P-wave velocity b) Horizontal S-wave velocity estimation of Eagle Ford shale in VTI media using Maxwell homogenization scheme.

3.9 Geomechanical Properties

Estimating geomechanical properties is crucial for hydraulic fracture design. Isotropic assumption in the properties used for completion can result in poor performance in the production (Reischman *et al.*, 2015). Peña (1998) provided Young's modulus and Poisson's ratio equations in terms of stiffness coefficients in different directions for anisotropic media.

Equation 3.32 is Young's modulus in the horizontal direction. Equation 3.33 is Young's modulus in the vertical direction. Equation 3.34 is Poisson's ratio in the vertical direction,

and Equations 3.35 & 3.36 are Poisson's ratio in the two horizontal directions.

$$E_1 = \frac{[C_{33}(C_{11} + C_{12}) - 2C_{13}^2](C_{11} - C_{12})}{C_{11}C_{33} - C_{13}^2} \quad (3.32)$$

$$E_3 = \frac{C_{33}(C_{11} + C_{12}) - 2C_{13}^2}{C_{11} + C_{12}} \quad (3.33)$$

$$\nu_{31} = \frac{C_{13}}{C_{11} + C_{12}}, \quad (3.34)$$

$$\nu_{12} = \frac{C_{33}C_{12} - C_{13}^2}{C_{11}C_{33} - C_{13}^2}, \quad (3.35)$$

$$\nu_{13} = \frac{C_{13}(C_{11} - C_{12})}{C_{11}C_{33} - C_{13}^2} \quad (3.36)$$

The stiffness coefficients of Eagle Ford shale obtained using Maxwell homogenization scheme are used to find both Young's modulus and Poisson's ratio in vertical and horizontal directions. Figure 3.27 illustrates variation of Poisson's ratio in two different directions. Similarly, estimated Young's modulus is shown in Figure 3.28.

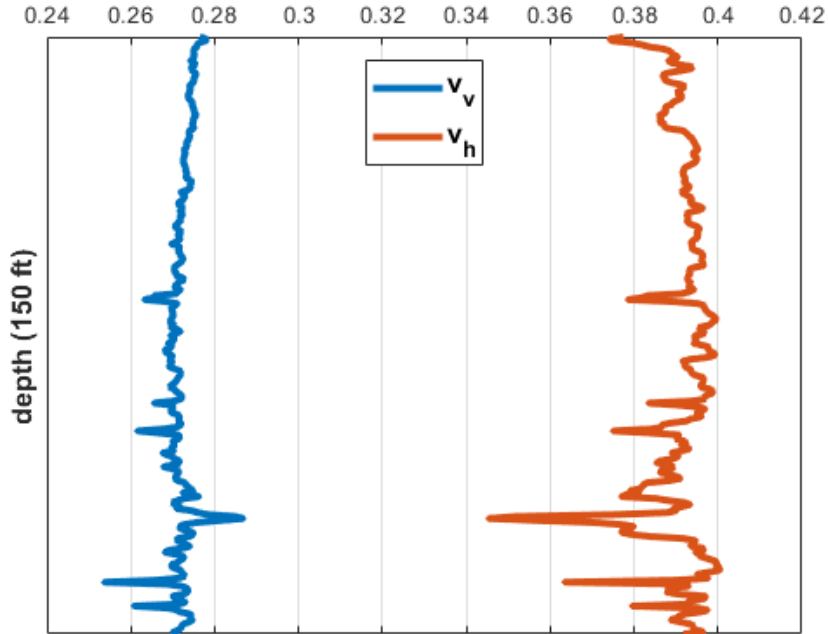


Figure 3.27: Poisson's ratio estimation in vertical and horizontal directions within Eagle Ford section.

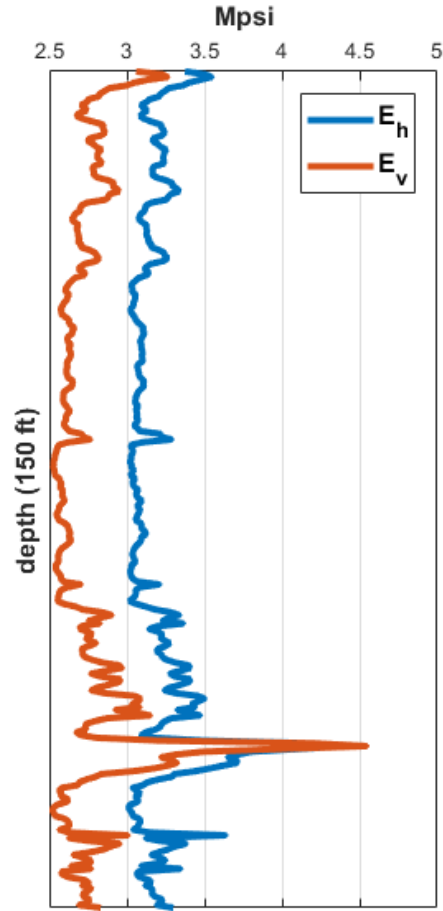


Figure 3.28: Young's modulus estimation in vertical and horizontal directions within Eagle Ford section.

3.10 Effect of Pore Fluids on Seismic Properties

Since this new rock physics model is able to model fluid-filled pores in the shale matrix, I can take advantage of this to demonstrate the effects of pore fluids and pore volume on seismic properties. To do this, I use oil and gas properties shown in Table 3.1. For the inorganic phase of the rock matrix, average values of minerals in this field are used. So, 29% quartz, 40% calcite and 31% clay are utilized in addition to 5% kerogen. I vary the porosity from 4% to 9% based on the well log information as shown in Table 3.8. The previously

constrained aspect ratios of each inclusion are kept the same. These specific values are discussed in Sections 3.5.1 and 3.5.2. Figure 3.29 illustrates that increasing porosity clearly lowers both P and S impedance. Even though the effect of oil-filled pores and gas-filled pores on impedances are very similar, Maxwell homogenization scheme can detect slight differences between various fluids.

Table 3.7: Elastic moduli and densities of oil and gas provided by Sang & Sun (2016)

Materials	K (GPa)	μ (GPa)	Density (g/cm ³)
Oil	1.31	0	0.80
Gas	0.10	0	0.50

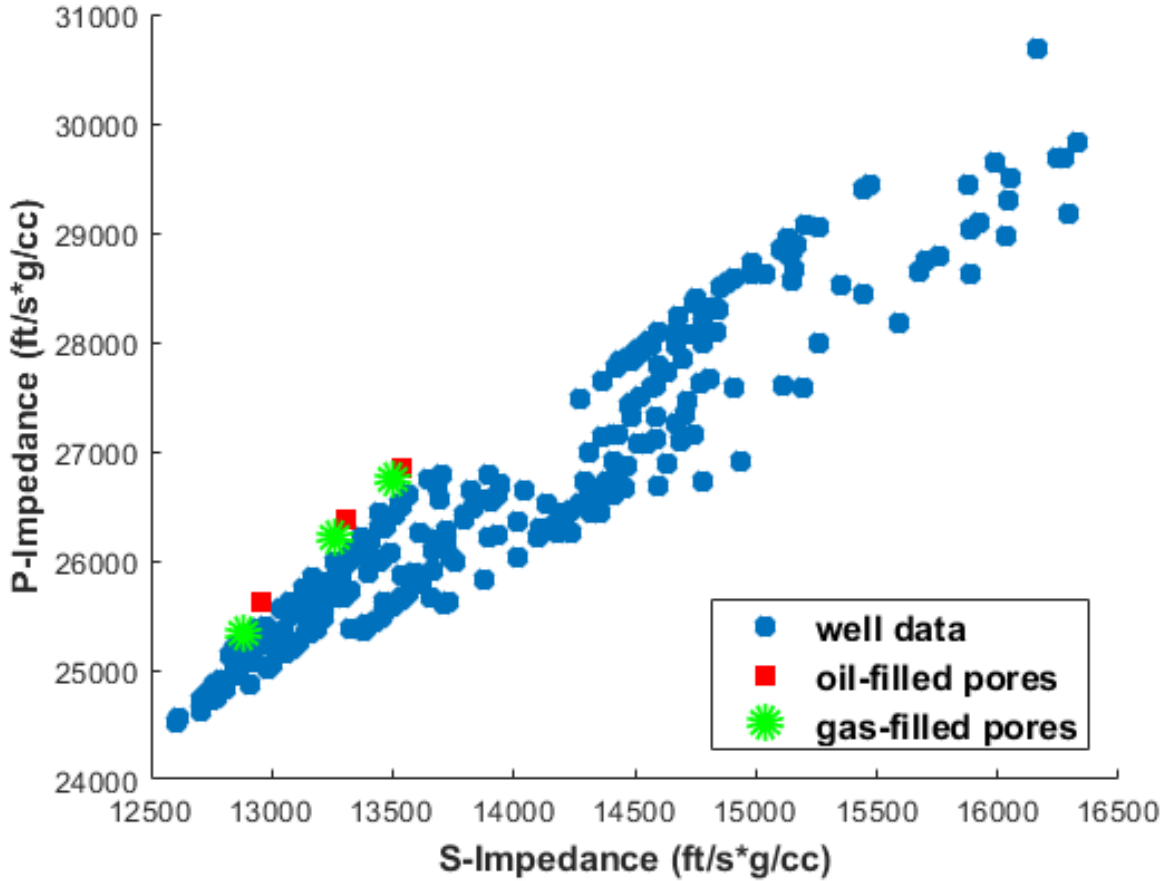


Figure 3.29: Effect of pore fluids on seismic impedances in comparison with the well data

Table 3.8: The effect of pore fluids on P and S impedance based on the rock physics modeling results

Fluid type	Porosity %	I_P (ft/s*g/cc)	I_S (ft/s*g/cc)	Density (g/cm^3)
Oil	4	26841	13536	2.5096
Oil	6	26382	13309	2.4728
Oil	9	25628	12954	2.4175
Gas	4	26747	13504	2.4976
Gas	6	26221	13260	2.4548
Gas	9	25346	12882	2.3905

This analysis has a value in a potential enhanced oil recovery (EOR) project. One can apply this model to see whether fluid change in pore space can be detected.

3.11 Effect of Thermal Maturity on Seismic Properties

Zhao *et al.* (2016) analyze the effect of thermal maturity on elastic properties using a rock physics model. In my model, I use kerogen as an inclusion as well. This can potentially help estimate P and S impedances at different maturity stages. Bulk and shear moduli of kerogen change with maturity level (Table 3.9).

Table 3.9: Elastic moduli and densities of kerogen used in this analysis at different maturity stages a = Yan & Han (2013), b = Qin* *et al.* (2014) and, c = Lucier *et al.* (2011)

Maturity Level	Hydrocarbon type	K (GPa)	μ (GPa)	ρ (g/cm^3)
Immature ^a	-	3.5	1.75	1.10
Mature ^b	Oil	5	3.5	1.26
Overmature ^c	Gas	7.98	4.18	1.34

Compared to fluid properties, modeling maturity is more complex, because increasing maturity changes not only elastic moduli of kerogen but also pore space and fluid type. Recently, Tutuncu & Bui (2019) state that when the source rock gets more mature, the liquid transforms to gas and expels out of the pore space. This eventually increases the porosity. In my model, I vary the pore space along with kerogen volume to account for the maturity level thoroughly (Table 3.10). Figure 3.30 shows maturity has an impact on impedances. In addition to increasing kerogen volume and porosity, maturity level causes a decrease in both P and S impedances.

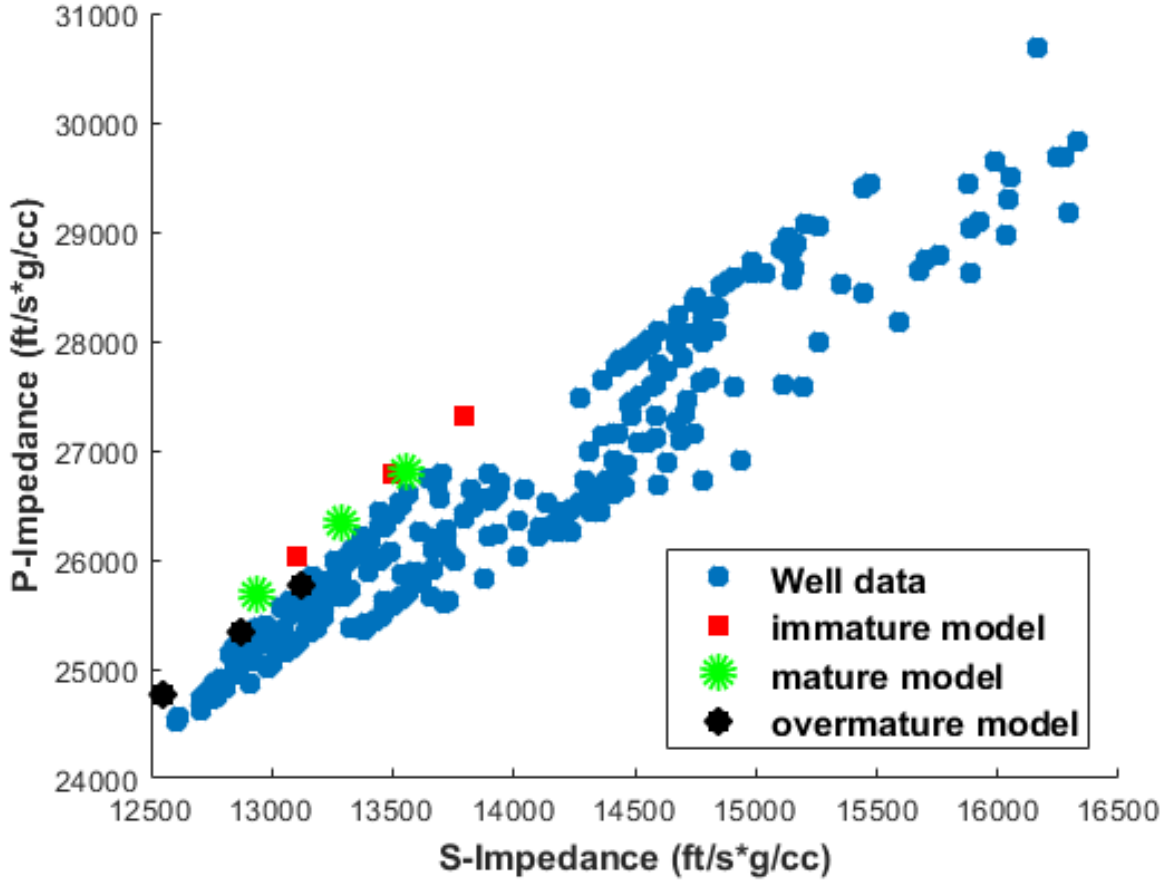


Figure 3.30: Effect of maturity on seismic impedances in comparison with the well data

Table 3.10: The effect of maturity level of kerogen on P and S impedance based on the rock physics modeling results

maturity	kerogen %	pores %	I_P (ft/s*g/cc)	I_S (ft/s*g/cc)	ρ (g/cm ³)
Immature	2	4	27320	13796	2.5464
Immature	5	4	26789	13502	2.5001
Immature	9	4	26038	13108	2.4384
Mature	2	6	26807	13551	2.5048
Mature	5	6	26334	13285	2.4633
Mature	9	6	25685	12938	2.4080
Overmature	2	9	25761	13120	2.4241
Overmature	5	9	25335	12872	2.3850
Overmature	9	9	24766	12551	2.3329

3.12 Discussion

With this new technique, the Maxwell homogenization scheme, we can attain plausible results and a realistic representation of the rock matrix in unconventional reservoirs. This new model allows one to model both clay and shale matrix at the same time. This process for unconventional shale would require the use of multiple rock physics model. Having a consistent model is crucial to have robust results. Furthermore, I apply this novel scheme to Eagle Ford shale and validate the fidelity of the rock physics modeling results.

In this chapter, I focus on the analysis of multiple inhomogeneties and their effects on seismic and reservoir properties. I include fluid-filled pores along with kerogen in our model. The uniqueness of this study is that we account for the shape of the inclusions to estimate the aspect ratio of cut domain thoroughly instead of assuming spherical effective inclusion domain. So, our embedded domain is ellipsoidal as are our inclusions. For this, I utilize a

formula suggested by Sevostianov (2014).

Although well logs, core measurements, and seismic inversion could help us calculate some of the geomechanical and reservoir properties, they are limited in understanding the anisotropy in the reservoir. For this reason, rock physics models are necessary to be able to analyze the reservoir and estimate parameters essential for completion design and well placement. With the help of the rock physics model I present in this chapter, one can analyze the anisotropic effects on geomechanical and seismic properties.

Since acoustic core measurements with increasing pressure is not provided by the vendor in this project, incorporating pressure dependence into the rock physics model is not possible. However, from the literature review, one can see that pressure dependence of seismic velocities and anisotropy is negligible in Eagle Ford shale. I suspect the small effect of pressure dependence as demonstrated by Sone & Zoback (2013) and Mokhtari *et al.* (2016) is not detectable.

3.13 Summary

The presented rock physics model and workflow can be applied to unconventional fields to estimate elastic stiffness coefficients of both clay and shale matrix in anisotropic media. For this application, one needs to constrain the modeling results using dipole sonic logs and/or core measurements taken from the field. Aspect ratios and elastic moduli (bulk and shear modulus) of some of the minerals such as quartz, calcite and pyrite are well known. Yet, the elastic properties of clays and kerogen need to be constrained a priori to obtain robust results using this rock physics model, the extended Maxwell homogenization scheme. Based on the results from this new rock physics model, Thomsen parameters obtained for Eagle Ford shale are $\epsilon = 0.19$, $\gamma = 0.29$ and $\delta = 0.04$.

CHAPTER 4

IMPLICATIONS FOR MULTICOMPONENT SEISMIC DATA

4.1 Introduction to AVA Analysis

One of the advantages of the rock physics model is to change the composite of the rock understand what would be the effect of each component on seismic properties in unconventional reservoirs. To analyze seismic response in the area of interest, I test different models by varying clay content, pore fluid and kerogen maturity to observe the implications for multicomponent seismic data in Eagle Ford shale.

This study is of importance, since clay content, kerogen and porosity has influence on anisotropy parameters. Using the rock physics model, I am able to create different realistic models based on the mineralogy and petrophysical data from the field, and test the sensitivity of different wave modes such as P-wave, PS-wave (converted wave), SV-wave (RR) and SH-wave (TT) to various complexities in shales. Amplitude variation with angle (AVA) analysis can be helpful to widen the understanding of different wave modes in seismic inversion.

4.2 AVA Analysis in VTI Media

In order to estimate reflection coefficients in VTI media, approximate coefficients for P-, C-, SV- and SH-waves derived by Rueger (2002) are used in this section.

$$R_P^{VTI} = \frac{1}{2} \frac{\Delta Z}{\bar{Z}} + \frac{1}{2} \left(\frac{\Delta V_{P0}}{\bar{V}_{P0}} - \left(\frac{2\bar{V}_{S0}}{\bar{V}_{P0}} \right)^2 \frac{\Delta G}{\bar{G}} + \Delta\delta \right) \sin^2 i + \frac{1}{2} \left(\frac{\Delta V_{P0}}{\bar{V}_{P0}} + \Delta\epsilon \right) \sin^2 i \tan^2 i \quad (4.1)$$

$$R_{SV}^{VTI} = -\frac{1}{2} \frac{\Delta Z^S}{\bar{Z}^S} + \left(\frac{7}{2} \frac{\Delta V_{S0}}{\bar{V}_{S0}} + 2 \frac{\Delta\rho}{\bar{\rho}} + \frac{1}{2} \left(\frac{\bar{V}_{P0}}{\bar{V}_{S0}} \right)^2 (\Delta\epsilon - \Delta\delta) \right) \sin^2 j - \frac{1}{2} \frac{\Delta V_{S0}}{\bar{V}_{S0}} \sin^2 j \tan^2 j \quad (4.2)$$

$$R_{SH}^{VTI} = -\frac{1}{2} \frac{\Delta Z^S}{\bar{Z}^S} + \frac{1}{2} \left(\frac{\Delta V_{S0}}{\bar{V}_{S0}} + \Delta \gamma \right) \tan^2 j \quad (4.3)$$

$$\begin{aligned} R_{PS}^{VTI} = & -\frac{1}{2} \frac{\Delta \rho}{\bar{\rho}} \frac{\sin i_1}{\cos j_1} - \frac{\bar{V}_{S0}}{\bar{V}_{P0}} \left(\frac{\Delta \rho}{\bar{\rho}} + 2 \frac{\Delta V_{S0}}{\bar{V}_{S0}} \right) \sin i_1 \cos i_1 + \left(\frac{\bar{V}_{S0}}{\bar{V}_{P0}} \right)^2 \left(2 \frac{\Delta V_{S0}}{\bar{V}_{S0}} + \frac{\Delta \rho}{\bar{\rho}} \right) \frac{\sin^3 i_1}{\cos j_1} \\ & + \left[\left(\frac{\bar{V}_{P0}^2}{2 (\bar{V}_{P0}^2 - \bar{V}_{S0}^2)} \cos j_1 - \frac{\bar{V}_{S0} \bar{V}_{P0} \cos i_1}{2 (\bar{V}_{P0}^2 - \bar{V}_{S0}^2)} \right) (\delta_2 - \delta_1) \right] \sin i_1 \\ & + \left[\frac{\bar{V}_{S0} \bar{V}_{P0} \cos i_1}{(\bar{V}_{P0}^2 - \bar{V}_{S0}^2)} (\delta_2 - \delta_1 + \epsilon_1 - \epsilon_2) \right] \sin^3 i_1 \\ & - \left[\frac{\bar{V}_{P0}^2}{(\bar{V}_{P0}^2 - \bar{V}_{S0}^2) \cos j_1} (\delta_2 - \delta_1 + \epsilon_1 - \epsilon_2) \right] \sin^3 i_1 \end{aligned} \quad (4.4)$$

Equations 4.1 - 4.4 are the linearized reflection coefficients of P-, SV, SH and PS waves, respectively, in VTI media. Z is P-wave impedance. V_{P0} and V_{S0} are vertical velocities of P- and S- wave, respectively. G is the vertical shear modulus. δ , ϵ and γ are Thomsen parameters. i is P-wave incidence angle, while j is S-wave incidence angle. Z^s refers to shear impedance. Expressions in the equations are $\Delta X = X2 - X1$ and $\bar{X} = (X1 + X2)/2$. Indices 1 and 2 represent upper and lower half of the interface, respectively.

Having obtained anisotropy information for Eagle Ford shale using both dipole sonic log and the rock physics model, I would like to perform AVA analysis to observe what would be the implications for multicomponent seismic data in different scenarios. For this purpose, I vary the clay content, the main driver of anisotropy in shales, and obtain four different models given in Table 4.1 and Table 4.2. The minimum clay volume in our area of interest is 15%, while it goes up to 41% at maximum. The average value of clay content is 31%, and the results for 31% clay are modeled as both isotropic and anisotropic. The overlying Austin Chalk is assumed to be isotropic for this study, and this information is based on the dipole sonic log analysis from Chapter 2.

In Figure 4.1, it is evident that higher anisotropy lowers the P-wave reflection coefficient. Moreover, there is a clear separation between the anisotropic and isotropic models around 15 degrees. With increasing incidence angle, the reflection coefficients of isotropic assumption deviates considerably.

Table 4.1: Vertical velocities and densities obtained from the rock physics model used for AVA analysis.

Models	Clay Content %	V_{P0} (ft/s)	V_{S0} (ft/s)	ρ (g/cc)
AC	-	17367	9017	2.65
EF1	15 (min)	11285	5796	2.4766
EF2	31 (avg)	10567	5308	2.4522
EF3	31 (avg iso)	10567	5308	2.4522
EF4	41 (max)	10242	5082	2.4416

Table 4.2: Thomsen parameters obtained using the rock physics model for AVA analysis.

Models	ϵ	γ	δ
EF1	0.17	0.2562	0.0358
EF2	0.1930	0.3039	0.0427
EF3	0	0	0
EF4	0.2030	0.3289	0.0447

Reflection coefficient of converted wave increases with incidence angle in all the models (Figure 4.2). Similar to the behavior of P-wave, reflection amplitudes of converted wave decrease with increasing angle for the isotropic model. When it comes to shear wave analysis, one can observe indisputably unique characteristics of vertical and horizontal modes. SV-

wave flips the polarity around 25 degrees in all the models. It is also seen that the SV-wave amplitudes flip polarity in the isotropic model at a lower degree (Figure 4.3). For SH wave, the reflection coefficient gets the same value with SV mode at normal incidence angle as expected (Figure 4.4). What stands out is that maximum clay content, meaning higher anisotropy, increases the reflection coefficient of horizontal shear wave compared to the other models.

The analysis of different wave modes is important, because one can interpret the behavior of different components in seismic data more accurately. In addition, the effects of anisotropy in unconventional reservoirs are significant. Increasing anisotropy is observed to result in more rapid changes in amplitude-variation-with-angle in the presented models.

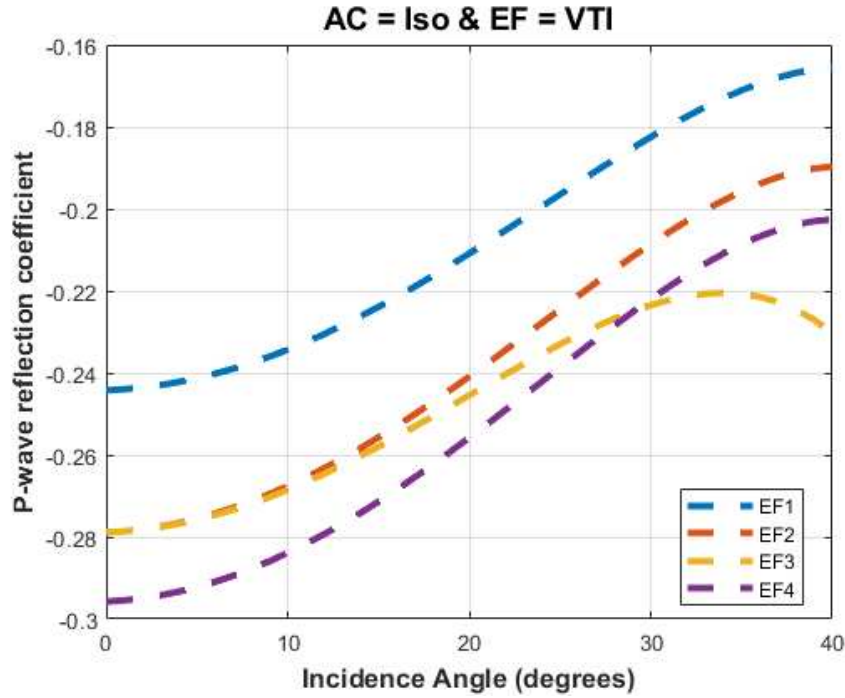


Figure 4.1: computed P-wave AVA curves using the models given in Table 4.1 and Table 4.2

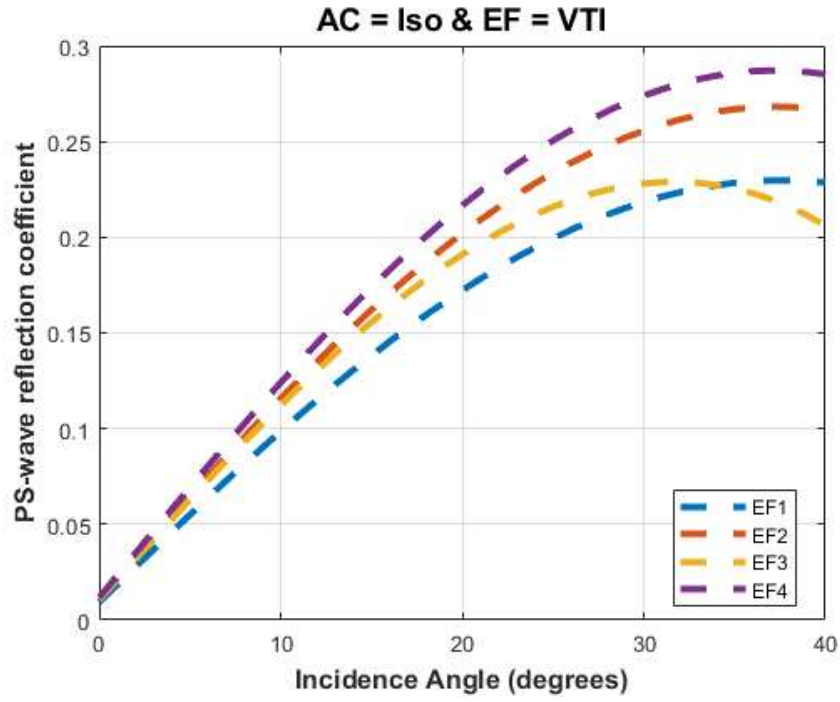


Figure 4.2: computed PS-wave AVA curves using the models given in Table 4.1 and Table 4.2

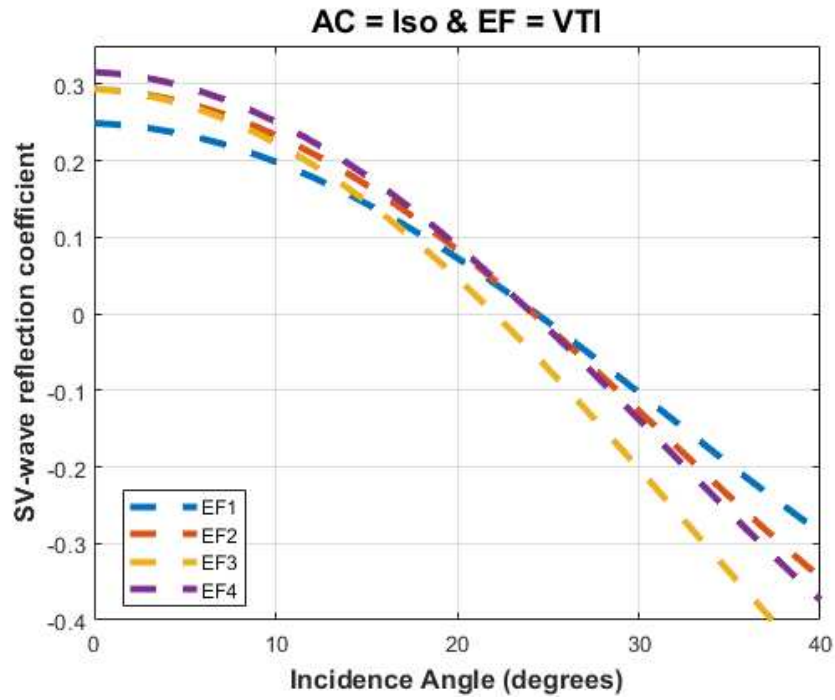


Figure 4.3: computed SV-wave AVA curves using the models given in Table 4.1 and Table 4.2

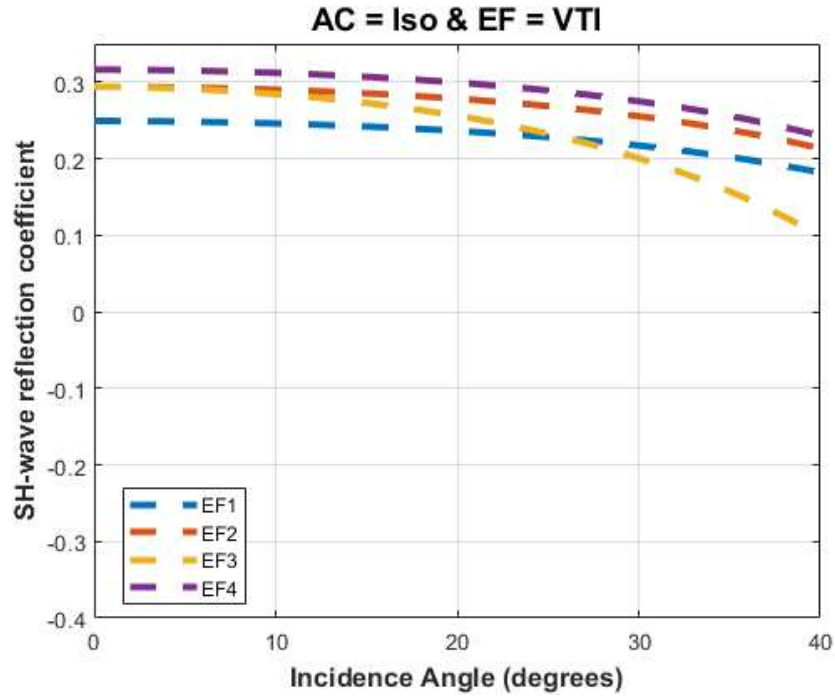


Figure 4.4: computed SH-wave AVA curves using the models given in Table 4.1 and Table 4.2

4.3 Effect of Thermal Maturity on AVA

In addition to clay content, microfractures and pores, the thermal maturity of kerogen is of significance in the elastic properties of the shales. To model the effect of kerogen, I model varying kerogen and maturity level while keeping the rest of the constituents such as minerals and aspect ratios constant (Table 4.3). Since pore space increases with maturity, I reflect this change in my model.

Table 4.3: The effect of maturity level of kerogen on P and S velocities and anisotropy based on the rock physics modeling results

maturity	ker-pore %	V_P (ft/s)	V_S (ft/s)	ρ (g/cm^3)	ϵ	γ	δ
Immature	2 - 4	10728	5417	2.5464	0.1809	0.2854	0.037
Immature	5 - 4	10714	5400	2.5001	0.1838	0.2906	0.038
Immature	9 - 4	10678	5375	2.4384	0.188	0.2968	0.04
Mature	2 - 6	10702	5410	2.5048	0.1862	0.29	0.0404
Mature	5 - 6	10690	5393	2.4633	0.1885	0.2948	0.041
Mature	9 - 6	10666	5372	2.4080	0.1912	0.3	0.0418
Overmature	2 - 9	10627	5412	2.4241	0.2	0.2978	0.0513
Overmature	5 - 9	10622	5397	2.3850	0.2026	0.3025	0.0513
Overmature	9 - 9	10616	5379	2.3329	0.2045	0.3074	0.0517

Figure 4.5 shows that increasing maturity decreases P-wave reflection coefficient, whereas it increases C-wave reflection coefficient with increasing angle. Changes in SV-wave with increasing angle are larger with respect to those in SH-wave (Figure 4.6). In both S-wave modes, one can observe that maturity increases reflection coefficient with increasing angle except that fact that after polarity reversal around 25° in SV-wave, the reflection coefficient of the immature model is slightly larger.

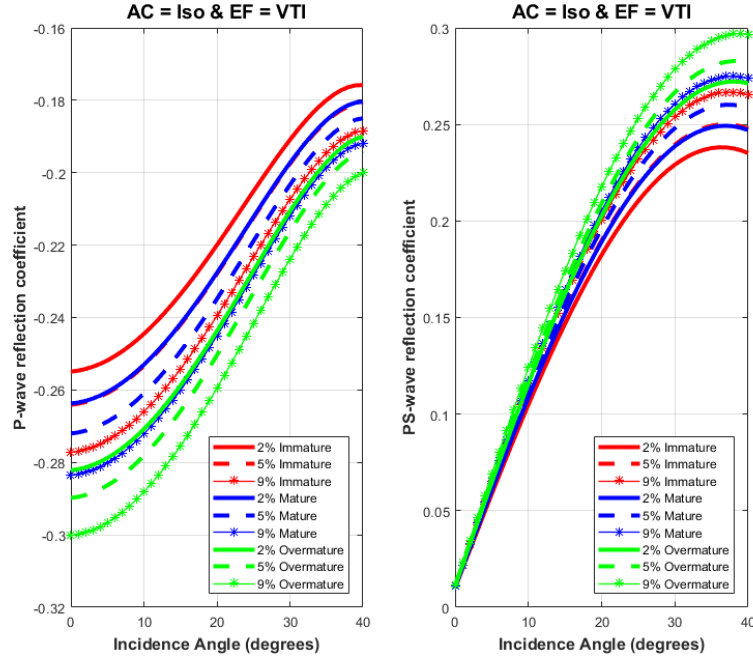


Figure 4.5: Computed P- and PS-wave AVA curves using the models given in Table 4.3

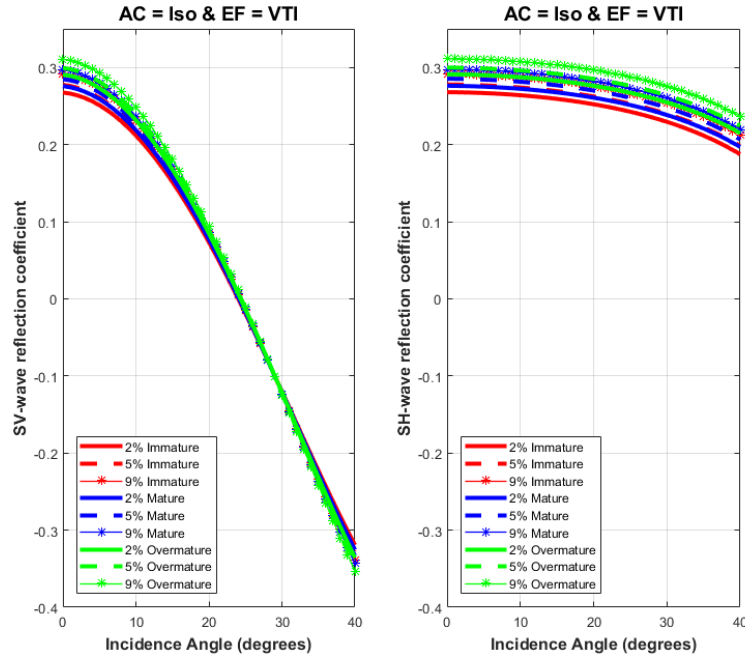


Figure 4.6: Computed SV- and SH-wave AVA curves using the models given in Table 4.3

4.4 Effect of Pore Fluids on AVA

Modeling the effect of different fluids in pore space is of importance to understand whether we can detect fluid effects in seismic data for future applications of Enhanced Oil Recovery (EOR) techniques. The properties given in Chapter 3 is also used to simulate amplitude variation with angle in different seismic wave modes. Two different fluid types, namely oil and gas, are modeled with changing porosity from 4 to 9 percent, while the other variables are held constant (Table 4.4).

Table 4.4: The effect of pore fluids on P and S velocities and anisotropy based on the rock physics modeling results

Fluid type	Porosity %	V_P (ft/s)	V_S (ft/s)	ρ (g/cm^3)	ϵ	γ	δ
Oil	4	10695	5393	2.5096	0.1839	0.2902	0.0382
Oil	6	10668	5382	2.4728	0.1885	0.2949	0.0411
Oil	9	10601	5358	2.4175	0.1978	0.3027	0.0472
Gas	4	10708	5406	2.4976	0.1849	0.2902	0.0390
Gas	6	10681	5401	2.4548	0.1908	0.2949	0.043
Gas	9	10602	5388	2.3905	0.2029	0.3027	0.051

Figure 4.7 exhibits larger variation between oil and gas in near angles (0 to 10°), while the difference between these two fluids becomes smaller in farther angles in P-wave mode. However, PS-wave reflection coefficient shows very similar values in near angles (0-10°) for all the models, but demonstrates slight differences between oil and gas with increasing angle. For both S-wave modes, it is difficult the differentiate between oil and gas on amplitude variation with angle (Figure 4.8). It should be also noted that high porosity increases reflection coefficients in all the models except for P-wave mode.

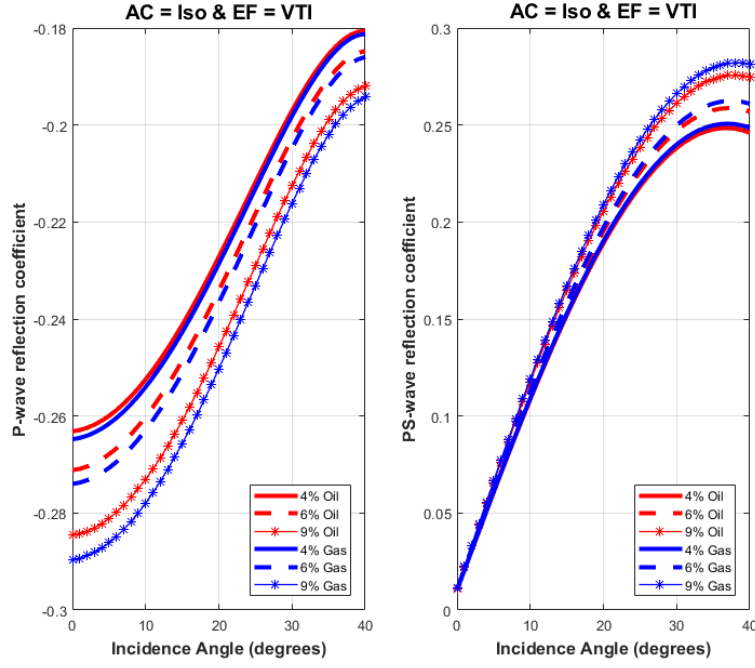


Figure 4.7: Computed P- and PS-wave AVA curves using the models given in Table 4.4.

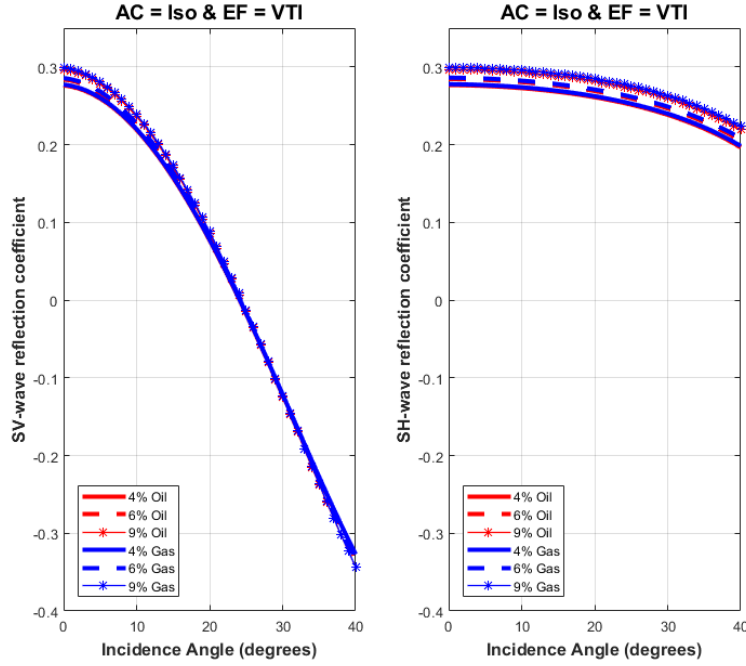


Figure 4.8: Computed SV- and SH-wave AVA curves using the models given in Table 4.4.

4.5 Discussion

In this chapter, I show that kerogen maturity and pore fluids slightly affect amplitude variation with angle compared to the clay content. It is well known that clay alignment is the main driver of anisotropy in shales. This chapter indicates that even though other heterogeneities inside the medium have impact on anisotropy and elastic properties, the influence of clay minerals is the most significant on both anisotropy and AVA analysis. This study also demonstrates that the new rock physics model is sensitive to the effect of fluid substitution inside the pore space. This allows one to estimate possible changes in seismic data in the case of enhanced oil recovery (EOR) or similar applications in the reservoir. Eagle Ford shale, specifically, is shown to be sensitive to VTI anisotropy in AVA analysis. This analysis solidifies that isotropic assumption in a highly anisotropic shale reservoir could lead to inaccurate outcomes in seismic properties. In AVA analysis, isotropic assumption deviates considerably in mid and far angles.

4.6 Summary

AVA analysis is helpful to identify the sensitivity of different seismic wave modes to intrinsic complexities in shales. It is clear that clay variation inside the reservoir could have an impact on different seismic wave modes. In contrast to clay volume variation, the models created from pore fluid and kerogen maturity do not exhibit comparable variation in seismic wave amplitudes. Increasing kerogen content decreases the amplitude of P-wave, whereas it increases the reflection coefficient of PS-wave. As for S-wave modes, the SV-wave shows the unique feature of a polarity around 25° . After 25° , increasing clay content has different impact and lowers the reflection coefficient of the SV-wave mode. Compared to SH wave, SV-wave shows more sensitivity to varying clay content.

CHAPTER 5

CONCLUSIONS

5.1 Observations and Discussion

In Chapter 1, I introduce the Eagle Ford project, available datasets, and some of the geological features in the area of interest.

In Chapter 2, I show how to process and analyze dipole sonic log data in anisotropic formations. Additionally, I review dipole sonic logging and Stoneley wave. Based on the interpretation of dipole sonic log, Eagle Ford shale clearly exhibits strong transverse isotropy with vertical axis of symmetry (VTI). However, the overlying Austin chalk is interpreted as isotropic. Most importantly, I find a strong correlation between the clay content in the Eagle Ford formation and anisotropy parameter (γ). This result implies that clay minerals and their alignments are the main cause of anisotropy in shales. I also indicate that stiffness coefficients obtained from dipole sonic logs can be used to constrain rock physics modeling results.

In Chapter 3, I present a novel rock physics model, extended Maxwell homogenization scheme, to predict elastic properties of unconventional reservoirs. This new model and the workflow I developed can handle modeling of both a clay matrix and organic-rich shales. In addition, the shape of the effective inclusion domain is taken into account for further analysis, because certain assumptions regarding this shape can cause an unrealistic estimation of elastic stiffness tensor. To obtain an accurate shape for the inclusion domain, I suggest using a method to calculate the aspect ratio of the effective inclusion domain by honoring the aspect ratio and volume fraction of each inhomogeneity. Subsequently, the fidelity of this new model is tested using field data of Eagle Ford shale. Based on the stiffness tensor in VTI media obtained using this new rock physics model, Thomsen parameters of ϵ , γ and δ are 0.19, 0.29 and 0.04, respectively. The results of the Maxwell homogenization scheme

are promising, and thus this robust rock physics model shows potential for application to other unconventional fields.

In Chapter 4, I investigate the effect of the clay content (i.e. anisotropy) on seismic properties. Using amplitude-variation-with-angle (AVA) analysis in VTI media, one can see the implications of the rock physics model in different seismic wave modes. I show that making an isotropic assumption in an anisotropic shale reservoir would result in significant error in mid and far angles in the AVA analysis. I also indicate that modeling fluid substitution in the pore space is possible using this new rock physics model. Even though different fluid components slightly change the results, it can be detected in this model. One can also simulate kerogen content in shales at different maturity stages with the help of the Maxwell homogenization scheme. Compared to horizontal shear wave (SH) mode, vertical shear wave (SV) mode is more sensitive to clay content variation in Eagle Ford shale.

5.2 Suggestions for Future Work

In order to further constrain my rock physics modeling results, I suggest taking additional core measurements in different directions so that anisotropy parameters can be obtained and the rock physics model can be further constrained. In addition, due to lack of information about alignment of clay platelets, I have assumed that clay minerals are aligned perfectly with respect to the symmetry axis. However, this assumption is not necessarily accurate in the nature. To better understand the distribution of clay platelets inside shales due to compaction and diagenesis, SEM images of cores in microscale should be acquired. One can then extract the orientation distribution function from the images and apply it to the extended Maxwell homogenization scheme. This process should enhance the accuracy and the physical explanation of the model.

Eagle Ford shale is known to have volcanic ash beds throughout the play. Since I do not have a direct information about this heterogeneity, I do not take ash beds into account in my rock physics modeling. Since volcanic ash beds can cause anisotropy, this should also be modeled in the Maxwell Homogenization scheme as inclusion. Volcanic ash beds and their

effects on elastic properties can be another area of research in the future project for this field.

Some engineering work done on this Eagle Ford project demonstrate inconsistency with geophysical analyses. This is due to poor assumptions and the failure to use the results from geophysical data sets. Isotropic assumptions regarding reservoir properties generally lead to incorrect results. For this reason, engineers should incorporate geomechanical properties estimated accurately in anisotropic media in their planning to improve well stimulation and well placement. Organic-rich shales such as Eagle Ford exhibit complex anisotropic structure. Thus, different data sets should be evaluated to obtain robust results regarding elastic properties in the area of interest. In this context, this new rock physics model can help one to update various reservoir parameters and understand their main drivers comprehensively.

REFERENCES CITED

- Alexandrov, K.S., & Ryzhova, T.V. 1961. The Elastic Properties of Rock-Forming Minerals. II: Layered Silicates. *Bulletin USSR Academy of science, Geophysics Series*, 1165–1168.
- Alkhalifah, Tariq, & Tsvankin, Ilya. 1995. Velocity analysis for transversely isotropic media. *Geophysics*, **60**(5), 1550–1566.
- Bandyopadhyay, K. 2009. *Seismic anisotropy: Geological causes and its implications to reservoir geophysics*. Ph.D. thesis, Stanford University.
- Barton, C D, & Karathanasis, A D. 2002. Clay minerals. *Encyclopedia of Soil Science*.
- Batzle, Michael, & Wang, Zhijing. 1992. Seismic properties of pore fluids. *Geophysics*, **57**(11), 1396–1408.
- Bayuk, Irina O., Ammerman, Mike, & Chesnokov, Evgeni M. 2007. Elastic moduli of anisotropic clay. *Geophysics*, **72**(5), D107–D117.
- Berge, P. A., & Berryman, J. G. 1995. Realizability of Negative Pore Compressibility in Poroelastic Composites. *Journal of Applied Mechanics*, **62**(4), 1053–1062.
- Berryman, James G., & Berge, Patricia A. 1996. Critique of two explicit schemes for estimating elastic properties of multiphase composites. *Mechanics of Materials*, **22**(2), 149–164.
- Bratton, Tom R. 2018. *Stress induced changes in elastic wave attributes in the Wattenberg Field, Colorado, USA*. Ph.D. thesis, Colorado School of Mines.
- Castberg, Rene C. 2014. *Impact of electric fields on the alignment of clay particles*. Ph.D. thesis, University of Oslo.
- Centurion, Sergio Marcelo, Cade, Randall, & Luo, Xin Lucy. 2012. Eagle Ford Shale: Hydraulic Fracturing, Completion, and Production Trends: Part II. *Pages 2925–2939 of: SPE Annual Technical Conference and Exhibition*, vol. 7. Society of Petroleum Engineers.
- Close, D, Cho, D, Horn, F, & Edmundson, H. 2009. The sound of sonic: A historical perspective and introduction to acoustic logging. *CSEG Recorder*, **34**(05), 34–43.

- Craddock, Paul, Lewis, Richard, Miles, Jeffrey, & Pomerantz, Andrew. 2019. Thermal maturity-adjusted log interpretation (TMALI) in organic shale. *Pages 1–19 of: SPWLA 60th Annual Logging Symposium Transactions*. Society of Petrophysicists and Well Log Analysts.
- Gherabati, S. Amin, Browning, John, Male, Frank, Ikonnikova, Svetlana A., & McDaid, Guinevere. 2016. The impact of pressure and fluid property variation on well performance of liquid-rich Eagle Ford shale. *Journal of Natural Gas Science and Engineering*, **33**, 1056–1068.
- Hashin, Z., & Shtrikman, S. 1963. A variational approach to the theory of the elastic behaviour of multiphase materials. *Journal of the Mechanics and Physics of Solids*, **11**(2), 127–140.
- Hentz, Tucker F., & Ruppel, Stephen C. 2010. Regional Lithostratigraphy of the Eagle Ford Shale : Maverick Basin to East Texas Basin. *GCAGS Transactions*, **60**, 325–337.
- Hentz, Tucker F., Ambrose, William A., & Smith, David C. 2014. Eaglebine play of the southwestern East Texas basin Stratigraphic and depositional framework of the Upper Cretaceous (Cenomanian-Turonian) Woodbine and Eagle Ford Groups. *AAPG Bulletin*, **98**(12), 2551–2580.
- Hill, R. 1963. Elastic properties of reinforced solids: Some theoretical principles. *Journal of the Mechanics and Physics of Solids*, **11**(5), 357–372.
- Hill, R. 1965. A self-consistent mechanics of composite materials. *Journal of the Mechanics and Physics of Solids*, **13**(4), 213–222.
- Hornby, Brian E., Schwartz, Larry M., & Hudson, John A. 1994. Anisotropic effective medium modeling of the elastic properties of shales. *Geophysics*, **59**(10), 1570–1583.
- Jones, Leonie E. A., & Wang, Herbert F. 1981. Ultrasonic velocities in Cretaceous shales from the Williston basin. *Geophysics*, **46**(3), 288–297.
- Katahara, Keith W. 1996. Clay mineral elastic properties. *Pages 1691–1694 of: SEG Technical Program Expanded Abstracts 1996*. Society of Exploration Geophysicists.
- Kuster, Guy T., & Toksöz, M. Nafi. 1974. Velocity and attenuation of seismic waves in two-phase media part I. theoretical formulations. *Geophysics*, **39**(5), 587–606.
- Lucier, Amie M., Hofmann, Ronny, & Bryndzia, L. Taras. 2011. Evaluation of variable gas saturation on acoustic log data from the Haynesville Shale gas play, NW Louisiana, USA. *The Leading Edge*, **30**(3), 300–311.

- Mavko, Gary, Mukerji, Tapan, & Dvorkin, Jack. 2009. *The Rock Physics Handbook*. Cambridge: Cambridge University Press.
- Maxwell, James Clerk. 1873. *A treatise on electricity and magnetism*. Oxford: Clarendon Press.
- Militzer, B., Wenk, H.-R., Stackhouse, S., & Stixrude, L. 2011. First-principles calculation of the elastic moduli of sheet silicates and their application to shale anisotropy. *American Mineralogist*, **96**(1), 125–137.
- Mokhtari, Mehdi, Honarpour, Mehdi Matt, Tutuncu, Azra Nur, & Boitnott, Gregory N. 2016. Characterization of Elastic Anisotropy in Eagle Ford Shale: Impact of Heterogeneity and Measurement Scale. *SPE Reservoir Evaluation & Engineering*, **19**(03), 429–439.
- Norris, Andrew N., & Sinha, Bikash K. 1993. Weak elastic anisotropy and the tube wave. *Geophysics*, **58**(8), 1091–1098.
- Nye, John Frederick. 1985. *Physical Properties of Crystals*. Oxford University Press.
- Ortega, J. Alberto, Ulm, Franz-Josef, & Abousleiman, Younane. 2007. The effect of the nanogranular nature of shale on their poroelastic behavior. *Acta Geotechnica*, **2**(3), 155–182.
- Peña, Franklin J. Ruiz. 1998. *Elastic properties of sedimentary anisotropic rocks*. Ph.D. thesis, Massachusetts Institute of Technology.
- Qin*, Xuan, Han, De-hua, & Zhao, Luanxiao. 2014. Rock physics modeling of organic-rich shales with different maturity levels. *Pages 2952–2957 of: SEG Technical Program Expanded Abstracts 2014*. Society of Exploration Geophysicists.
- Ratcliffe, K.T., Wright, A.M., & Schmidt, K. 2012. Application of inorganic whole-rock geochemistry to shale resource plays: an example from the Eagle Ford Shale Formation, Texas. *The Sedimentary Record*, **10**(2), 4–9.
- Reischman, Richard, Brooks, Scott, Willms, Trevor, Albrecht, Tony L., Walsh, John J., & Arteaga, Edgar. 2015. Acoustic Log Measurements in the Lower Eagle Ford Formation in Brazos and Robertson Counties, Texas and Their Implications on Completion Design. *In: Proceedings of the 3rd Unconventional Resources Technology Conference*. Tulsa, OK, USA: American Association of Petroleum Geologists.
- Reuss, A. 1929. Berechnung der Fließgrenze von Mischkristallen auf Grund der Plastizitätsbedingung für Einkristalle. *ZAMM - Zeitschrift für Angewandte Mathematik und Mechanik*, **9**(1), 49–58.

- Rueger, Andreas. 2002. 4. Reflectivity in VTI Media. *Pages 39–62 of: Reflection Coefficients and Azimuthal AVO Analysis in Anisotropic Media*. Society of Exploration Geophysicists.
- Sang, Liqin, & Sun, Yuefeng. 2016. Two-stage rock-physics modeling of the elastic properties of organic-rich shales. *Pages 3164–3168 of: SEG Technical Program Expanded Abstracts 2016*. Society of Exploration Geophysicists.
- Saxena, Vimal, Krief, Michel, & Adam, Ludmila. 2018. *Handbook of Borehole Acoustics and Rock Physics for Reservoir Characterization*. Elsevier.
- Sayers, C.M. 2005. Seismic anisotropy of shales. *Geophysical Prospecting*, **53**(5), 667–676.
- Sayers, Colin M., & Dasgupta, Sagnik. 2019. A predictive anisotropic rock-physics model for estimating elastic rock properties of unconventional shale reservoirs. *Leading Edge*, **38**(5), 358–365.
- Sayers, Colin M., & den Boer, Lennert D. 2018. The Elastic Properties of Clay in Shales. *Journal of Geophysical Research: Solid Earth*, **123**(7), 5965–5974.
- Sayers, Colin M., Guo, Shiguang, & Silva, Josimar. 2015. Sensitivity of the elastic anisotropy and seismic reflection amplitude of the Eagle Ford Shale to the presence of kerogen. *Geophysical Prospecting*, **63**(1), 151–165.
- Schultz, Whitney. 2019. *Time-lapse multicomponent geophone and DAS VSP processing and analysis (MSc thesis)*. Golden: Colorado School of Mines.
- Sevostianov, I., & Kachanov, M. 2002. Explicit cross-property correlations for anisotropic two-phase composite materials. *Journal of the Mechanics and Physics of Solids*, **50**(2), 253–282.
- Sevostianov, Igor. 2014. On the shape of effective inclusion in the Maxwell homogenization scheme for anisotropic elastic composites. *Mechanics of Materials*, **75**, 45–59.
- Sevostianov, Igor. 2017. Maxwell Homogenization Scheme in Micromechanics: an Overview. *MATEC Web of Conferences*, **132**(10), 03017.
- Sevostianov, Igor, & Giraud, Albert. 2013. Generalization of Maxwell homogenization scheme for elastic material containing inhomogeneities of diverse shape. *International Journal of Engineering Science*, **64**, 23–36.
- Sevostianov, Igor, & Kachanov, Mark. 2014. On some controversial issues in effective field approaches to the problem of the overall elastic properties. *Mechanics of Materials*, **69**(1), 93–105.

- Sevostianov, Igor, Yilmaz, Nadir, Kushch, Vladimir, & Levin, Valery. 2005. Effective elastic properties of matrix composites with transversely-isotropic phases. *International Journal of Solids and Structures*, **42**(2), 455–476.
- Sone, Hiroki, & Zoback, Mark D. 2013. Mechanical properties of shale-gas reservoir rocks Part 1: Static and dynamic elastic properties and anisotropy. *Geophysics*, **78**(5), D381–D392.
- Stoneley, R. 1924. Elastic Waves at the Surface of Separation of Two Solids. *Proceedings of the Royal Society A: Mathematical, Physical and Engineering Sciences*, **106**(738), 416–428.
- Thomsen, Leon. 1986. Weak elastic anisotropy. *Geophysics*, **51**(10), 1954–1966.
- Tsvankin, Ilya, Gaiser, James, Grechka, Vladimir, van der Baan, Mirko, & Thomsen, Leon. 2010. Seismic anisotropy in exploration and reservoir characterization: An overview. *Geophysics*, **75**(5), 15–75.
- Tuppen, Charles Adam. 2019. *Nine-component seismic amplitude inversion: a case study in the Eagle Ford Shale (MSc thesis)*. Golden: Colorado School of Mines.
- Tutuncu, Azra N., & Bui, Binh. 2019. A Comparative Study of Organic Richness and Maturity Impact on Anisotropic Geomechanical Properties in Shale Reservoirs. *In: Proceedings of the 7th Unconventional Resources Technology Conference*. Tulsa, OK, USA: American Association of Petroleum Geologists.
- U.S. Energy Information Administration. 2014. Updates to the EIA Eagle Ford Play Maps. *United States Energy Information Administration. Independent Statistics & Analysis, U.S. Department of Energy*, 1–10.
- Vanorio, Tiziana, Prasad, Manika, & Nur, Amos. 2003. Elastic properties of dry clay mineral aggregates, suspensions and sandstones. *Geophysical Journal International*, **155**(1), 319–326.
- Vilchevskaya, Elena, & Sevostianov, Igor. 2015. Effective elastic properties of a particulate composite with transversely-isotropic matrix. *International Journal of Engineering Science*, **94**, 139–149.
- Voigt, Woldemar. 1910. *Lehrbuch der Krystallophysik: (mit Ausschluss der Krystalloptik)*. BG Teubner-Verlag, Leipzig.
- Wang, Zhijing (Zee), Wang, Hui, & Cates, Michael E. 2001. Effective elastic properties of solid clays. *Geophysics*, **66**(2), 428–440.

- Wilson, M. J ., Wilson, L., & Patey, I . 2014. The influence of individual clay minerals on formation damage of reservoir sandstones: a critical review with some new insights. *Clay Minerals*, **49**(2), 147–164.
- Yan, Fuyong, & Han, De-hua. 2013. Measurement of elastic properties of kerogen. *Pages 2778–2782 of: SEG Technical Program Expanded Abstracts 2013*. Society of Exploration Geophysicists.
- Zhang, Feng, Zhang, Tuo, & Li, Xiang Yang. 2019. Seismic amplitude inversion for the transversely isotropic media with vertical axis of symmetry. *Geophysical Prospecting*, 1365–2478.
- Zhao, Luanxiao, Qin, Xuan, Han, De-Hua, Geng, Jianhua, Yang, Zhifang, & Cao, Hong. 2016. Rock-physics modeling for the elastic properties of organic shale at different maturity stages. *Geophysics*, **81**(5), D527–D541.

APPENDIX A

TENSORIAL BASIS OF SEVOSTIANOV AND KACHANOV, 2002

In this thesis, I use the tensorial basis of Sevostianov & Kachanov (2002) to calculate the fourth rank tensor of effective media in Maxwell homogenization scheme.

$$\begin{aligned}
T_{ijkl}^{(1)} &= \theta_{ij}\theta_{kl}, T_{ijkl}^{(2)} = (\theta_{ik}\theta_{lj} + \theta_{il}\theta_{kj} - \theta_{ij}\theta_{kl})/2, \\
T_{ijkl}^{(3)} &= \theta_{ij}m_k m_l, T_{ijkl}^{(4)} = m_i m_j \theta_{kl}, \\
T_{ijkl}^{(5)} &= (\theta_{ik}m_l m_j + \theta_{il}m_k m_j + \theta_{jk}m_l m_i + \theta_{jl}m_k m_i)/4, \\
T_{ijkl}^{(6)} &= m_i m_j m_k m_l,
\end{aligned} \tag{A.1}$$

where $\theta_{ij} = \delta_{ij} - m_i m_j$ and $\mathbf{m} = m_1 e_1 + m_2 e_2 + m_3 e_3$ is a unit vector along the axis of transverse symmetry.

These tensors form a closed algebra with respect to the operation of multiplication

$$(\mathbf{T}^{(\alpha)} : \mathbf{T}^{(\beta)})_{ijkl} \equiv T_{ijpq}^{(\alpha)} T_{pqkl}^{(\beta)} \tag{A.2}$$

Then the inverse of any fourth rank tensor \mathbf{X} , as well as the product $\mathbf{X} : \mathbf{Y}$ of two such tensors are readily found in the closed form, as soon as the representations in the basis

$$\mathbf{X} = \sum_{k=1}^6 X_k \mathbf{T}^{(k)}, \quad \mathbf{Y} = \sum_{k=1}^6 Y_k \mathbf{T}^{(k)} \tag{A.3}$$

are established.

The Inverse tensor \mathbf{X}^{-1} defined by

$$X_{ijmn}^{-1} X_{mnkl} = (X_{ijmn} X_{mnkl}^{-1}) = J_{ijkl} \text{ is given by}$$

$$\begin{aligned}
\mathbf{X}^{-1} &= \frac{X_6}{2\Delta} \mathbf{T}^{(1)} + \frac{1}{X_2} \mathbf{T}^{(2)} - \frac{X_3}{\Delta} \mathbf{T}^{(3)} - \frac{X_4}{\Delta} \mathbf{T}^{(4)} \\
&\quad + \frac{4}{X_5} \mathbf{T}^{(5)} + \frac{2X_1}{\Delta} \mathbf{T}^{(6)}
\end{aligned} \tag{A.4}$$

where $\Delta = 2(X_1 X_6 - X_3 X_4)$.

The product of two tensors $\mathbf{X} : \mathbf{Y}$ (tensor with $ijkl$ components equal to $X_{ijmn}Y_{mnkl}$) is

$$\begin{aligned}\mathbf{X} : \mathbf{Y} = & (2X_1Y_1 + X_3Y_4)\mathbf{T}^{(1)} + (X_2Y_2)\mathbf{T}^{(2)} \\ & + (2X_1Y_3 + X_3Y_6)\mathbf{T}^{(3)} + (2X_4Y_1 + X_6Y_4)\mathbf{T}^{(4)} \\ & + \left(\frac{1}{2}X_5Y_5\right)\mathbf{T}^{(5)} + (X_6Y_6 + 2X_4Y_3)\mathbf{T}^{(6)}\end{aligned}\quad (\text{A.5})$$

If x_3 is the axis of transverse symmetry, tensors $T^{(1)}, \dots, T^{(6)}$ given by A.1 have the following non-zero components:

$$\begin{aligned}\mathbf{T}_{1111}^{(1)} &= \mathbf{T}_{2222}^{(1)} = \mathbf{T}_{1122}^{(1)} = \mathbf{T}_{2211}^{(1)} = 1, \\ \mathbf{T}_{1212}^{(2)} &= \mathbf{T}_{2121}^{(2)} = \mathbf{T}_{1221}^{(2)} = \mathbf{T}_{2112}^{(2)} = \mathbf{T}_{1111}^{(2)} = \mathbf{T}_{2222}^{(2)} = \frac{1}{2}, \\ \mathbf{T}_{1122}^{(2)} &= \mathbf{T}_{2211}^{(2)} = -\frac{1}{2}, \\ \mathbf{T}_{1133}^{(3)} &= \mathbf{T}_{2233}^{(3)} = 1, \\ \mathbf{T}_{3311}^{(4)} &= \mathbf{T}_{3322}^{(4)} = 1, \\ \mathbf{T}_{1313}^{(5)} &= \mathbf{T}_{2323}^{(5)} = \mathbf{T}_{2332}^{(5)} = \mathbf{T}_{3113}^{(5)} = \mathbf{T}_{3223}^{(5)} = \mathbf{T}_{3131}^{(5)} = \mathbf{T}_{3232}^{(5)} = \frac{1}{4}, \\ \mathbf{T}_{3333}^{(6)} &= 1.\end{aligned}\quad (\text{A.6})$$

A general transversely isotropic fourth rank tensor, being represented in this basis

$$\Psi_{ijkl} = \sum_{m=1}^6 \psi_m T_{ijkl}^{(m)}$$

has the following components:

$$\begin{aligned}\psi_1 &= (\Psi_{1111} + \Psi_{1122})/2, & \psi_2 &= 2\Psi_{1212}, & \psi_3 &= \Psi_{1133}, \\ \psi_4 &= \Psi_{3311}, & \psi_5 &= 4\Psi_{1313}, & \psi_6 &= \Psi_{3333}.\end{aligned}\quad (\text{A.7})$$

Utilizing A.7 one obtains the following representations.

The components of the elastic stiffness tensor in a general transversely isotropic media can be written as

$$\begin{aligned}C_1 &= (C_{1111} + C_{1122})/2, & C_2 &= 2C_{1212}, & C_3 &= C_{1133}, \\ C_4 &= C_{3311}, & C_5 &= 4C_{1313}, & C_6 &= C_{3333}.\end{aligned}\quad (\text{A.8})$$

Tensor of elastic compliances of the isotropic material $S_{ijkl} = \sum_{m=1}^6 s_m T_{ijkl}^m$ has the following components:

$$\begin{aligned} s_1 &= \frac{1 - \nu_0}{4\mu_0(1 + \nu_0)}, & s_2 &= \frac{1}{2\mu_0}, & s_3 &= s_4 = \frac{-\nu_0}{2\mu_0(1 + \nu_0)}, \\ s_5 &= \frac{1}{\mu_0}, & s_6 &= \frac{1}{2\mu_0(1 + \nu_0)}. \end{aligned} \quad (\text{A.9})$$

Tensor of elastic stiffness of the isotropic material $C_{ijkl} = \sum_{m=1}^6 c_m T_{ijkl}^m$ has the following components:

$$\begin{aligned} c_1 &= \lambda_0 + \mu_0, & c_2 &= 2\mu_0, & c_3 &= c_4 = \lambda_0, \\ c_5 &= 4\mu_0, & c_6 &= \lambda_0 + 2\mu_0. \end{aligned} \quad (\text{A.10})$$

where λ_0 is Lamé parameter and can be found in equation B.7. ν_0 is Poisson's ratio and can be calculated using equation B.8. K_0 and μ_0 are bulk and shear modulus of the rock matrix, respectively.

Isomers of fourth rank unit tensors are represented in the form

$$\begin{aligned} \mathbf{J}_{ijkl} &= (\delta_{ik}\delta_{lj} + \delta_{il}\delta_{kj})/2 \\ &= \frac{1}{2}T_{ijkl}^1 + T_{ijkl}^2 + 2T_{ijkl}^5 + T_{ijkl}^6, \end{aligned} \quad (\text{A.11})$$

$$\mathbf{II}_{ijkl} = \delta_{ij}\delta_{kl} = T_{ijkl}^1 + T_{ijkl}^3 + T_{ijkl}^4 + T_{ijkl}^6. \quad (\text{A.12})$$

APPENDIX B

MAXWELL HOMOGENIZATION SCHEME OF SEVOSTIANOV, 2014

The derivation of the coefficients using the tensorial basis in A.1 was done by Sevostianov (2014); Sevostianov & Giraud (2013). I use the following coefficients derived by Sevostianov (2014) for the computation of the clay matrix, because I define background matrix and each inclusion as isotropic in my model. So, the coefficients below are beneficial.

The stiffness contribution tensor \mathbf{N} for a spheroidal inhomogeneity is represented in the basis A.1 by coefficients

$$\begin{aligned} n_1 &= \frac{1}{2\delta_1} \left[\frac{\Delta\lambda + \Delta\mu}{\Delta\mu(3\Delta\lambda + 2\Delta\mu)} + p_6 \right], & n_2 &= \frac{2\Delta\mu}{1 + 2p_2\Delta\mu}, \\ n_3 &= n_4 = -\frac{1}{\delta_1} \left[-\frac{\Delta\lambda}{2\Delta\mu(3\Delta\lambda + 2\Delta\mu)} + p_3 \right], \\ n_5 &= \frac{4\Delta\mu}{1 + \Delta\mu p_5}, & n_6 &= \frac{1}{\delta_1} \left[\frac{\Delta\lambda + 2\Delta\mu}{2\Delta\mu(3\Delta\lambda + 2\Delta\mu)} + 2p_1 \right]. \end{aligned} \quad (\text{B.1})$$

where

$$\begin{aligned} \Delta\mu &= \mu_i - \mu_0, & \Delta\lambda &= \lambda_i - \lambda_0 \\ \delta_1 &= \frac{1 + (\Delta\lambda + 2\Delta\mu)p_6 + 4(\Delta\lambda + \Delta\mu)2p_1 + 4\Delta\lambda p_3}{2\Delta\mu(3\Delta\lambda + 2\Delta\mu)} \\ &\quad + 2p_1 p_6 - 2p_3^2 \end{aligned} \quad (\text{B.2})$$

Here i indicates the inclusion. Since we have multiple inclusions, it is necessary to calculate the coefficients for each one of them separately. μ_0 and λ_0 are shear modulus and Lamé parameter of the rock matrix, respectively. Lamé parameter is calculated using equation B.7.

The coefficients of Hill's tensors \mathbf{P} and \mathbf{Q} are:

$$\begin{aligned} p_1 &= \frac{1}{2\mu_0}[(1 - \kappa)f_0 + \kappa f_1], & p_2 &= \frac{1}{2\mu_0}[(2 - \kappa)f_0 + \kappa f_1], \\ p_3 &= p_4 = -\frac{\kappa}{\mu_0}f_1, & p_5 &= \frac{1}{\mu_0}(1 - f_0 - 4\kappa f_1), \\ p_6 &= \frac{1}{\mu_0}[(1 - \kappa)(1 - 2f_0) + 2\kappa f_1] \end{aligned} \quad (\text{B.3})$$

and

$$\begin{aligned} q_1 &= \mu_0[4\kappa - 1 - 2(3\kappa - 1)f_0 - 2\kappa f_1], \\ q_2 &= 2\mu_0[1 - (2 - \kappa)f_0 - \kappa f_1], \\ q_3 &= q_4 = 2\mu_0[(2\kappa - 1)f_0 + 2\kappa f_1], \\ q_5 &= 4\mu_0(f_0 + 4\kappa f_1), & q_6 &= 8\mu_0(\kappa f_0 - \kappa f_1). \end{aligned} \quad (\text{B.4})$$

where $\kappa = 1/[2(1 - \nu_0)]$. ν_0 is Poisson's ratio of the rock matrix and defined as equation B.8. Functions $f_0(\alpha)$ and $f_1(\alpha)$ are dependent on aspect ratio (α) and given by

$$f_0 = \frac{\alpha^2(1 - g)}{2(\alpha^2 - 1)}, \quad f_1 = \frac{\kappa\alpha^2}{4(\alpha^2 - 1)^2}[(2\alpha^2 + 1)g - 3] \quad (\text{B.5})$$

where

$$g(\alpha) = \begin{cases} \frac{1}{\alpha\sqrt{1-\alpha^2}} \arctan \frac{\sqrt{1-\alpha^2}}{\alpha}, & \text{oblate shape } (\alpha < 1) \\ \frac{1}{2\alpha\sqrt{\alpha^2-1}} \ln \frac{\alpha+\sqrt{\alpha^2-1}}{\alpha-\sqrt{\alpha^2-1}}, & \text{prolate shape } (\alpha > 1) \end{cases} \quad (\text{B.6})$$

Here, an ellipsoidal inhomogeneity with dimensions $a_3 = c$ and $a_1 = a_2 = a$ along axes x_1 , x_2 , and x_3 in a transversely isotropic medium, the aspect ratio α is defined as $\alpha = c/a$.

Elastic parameters needed for this study can be calculated as follows.

$$\lambda_0 = K_0 - \frac{2\mu_0}{3} \quad (\text{B.7})$$

$$\nu_0 = \frac{\lambda_0}{2(\lambda_0 + \mu_0)} \quad (\text{B.8})$$

where λ_0 and ν_0 are Lamé parameter and Poisson's ratio of the rock matrix, respectively. K_0 and μ_0 are bulk and shear modulus of the rock matrix, respectively.

APPENDIX C

P TENSOR DERIVATION IN ANISOTROPIC MEDIA BY SEVOSTIANOV ET AL, 2005

After obtaining anisotropic clay matrix, I utilize the coefficients of the P tensor in anisotropic media in order to model Eagle Ford shale with anisotropic clay matrix as the host. The derivations of this tensor are done by Sevostianov *et al.* (2005) in the tensorial basis of Sevostianov & Kachanov (2002).

$$P_{ijkl} = P_1 T_{ijkl}^1 + P_2 T_{ijkl}^2 + P_3 T_{ijkl}^3 + P_4 T_{ijkl}^4 + P_5 T_{ijkl}^5 + P_6 T_{ijkl}^6 \quad (\text{C.1})$$

The coefficients of P tensor in transversely anisotropic media, $P_1, P_2, P_3, P_4, P_5, P_6$ are in the form as follows:

$$\begin{aligned} P_1 &= \frac{\pi}{2} \sum_{l=1}^3 (b_l - A_l a_l) J_1^{(l)}, \quad P_2 = \frac{\pi}{2} \sum_{l=1}^3 (2b_l - A_l a_l) J_1^{(l)}, \\ P_3 &= -\frac{\pi}{2} \sum_{l=1}^3 c_l (J_1^{(l)} - \alpha^2 A_l J_2^{(l)}), \quad P_4 = -\frac{\pi}{2} \sum_{l=1}^3 c_l (J_1^{(l)} - \alpha^2 A_l J_2^{(l)}), \\ P_5 &= \pi \sum_{(l=1)}^3 [(2b_l - A_l a_l) \alpha^2 J_2^{(l)} - c_l (J_1^{(l)} - \alpha^2 A_l J_2^{(l)}) + d_l J_1^{(l)}], \quad P_6 = 2\pi \sum_{l=1}^3 d_l \alpha^2 J_2^{(l)} \end{aligned} \quad (\text{C.2})$$

where

$$\begin{aligned} J_1^{(l)} &= 2\lambda_l^2 \left[1 - \frac{1}{2} \alpha^2 A_l \lambda_l \ln \left(\frac{\lambda_l + 1}{\lambda_l - 1} \right) \right], \\ J_2^{(l)} &= 2\lambda_l^2 \left[\frac{1}{2} \lambda_l \ln \left(\frac{\lambda_l + 1}{\lambda_l - 1} \right) - 1 \right], \end{aligned} \quad (\text{C.3})$$

and

$$\lambda_l = \sqrt{\frac{1}{1 - A_l \alpha^2}}. \quad (\text{C.4})$$

Here, for an ellipsoidal inclusion with dimensions $a_1 = a_2 = a$ and $a_3 = c$ along axes x_1, x_2 , and x_3 in transversely isotropic media, α is defined as a/c in contrast with how it is

calculated in Appendix B.

The coefficients a_l , b_l , c_l , d_l , A_1 , A_2 , and A_3 depend on the components of the elastic stiffness tensor of the background medium (which is, in our case, clay matrix), and are written as follows

$$a_l = \frac{1}{\epsilon_l} [(C_{1212} - C_{1111})(C_{3333} - A_l C_{2323}) + (C_{1133} + C_{2323})^2], \quad (\text{C.5})$$

$$b_l = \frac{1}{\epsilon_l} [(C_{2323} - A_l C_{1111})(C_{3333} - A_l C_{2323}) + A_l (C_{1133} + C_{2323})^2], \quad (\text{C.6})$$

$$c_l = \frac{1}{\epsilon_l} (C_{1133} - C_{2323})(C_{2323} - A_l C_{1212}), \quad (\text{C.7})$$

$$d_l = \frac{1}{\epsilon_l} (C_{2323} - C_{1111})(C_{2323} - A_l C_{1212}), \quad (\text{C.8})$$

$$\epsilon_l = 4\pi C_{1111} C_{2323} C_{1212} \prod_{j=1}^3 (A_j - A_l) \quad \text{here } j \neq l, \quad (\text{C.9})$$

The coefficients of A can be found below

$$A_1 = \frac{C_{2323}}{C_{1212}} \quad (\text{C.10})$$

A_2 and A_3 are the roots of the quadratic equation

$$C_{1111} C_{2323} A^2 + (C_{1133}^2 + 2C_{1133} C_{2323} - C_{1111} C_{3333}) A + C_{3333} C_{2323} = 0 \quad (\text{C.11})$$